Chapter 2
Mechanisms of Formation of Some Forms of Electrodeposited Pure Metals

2.1 Electrodeposition on Native Substrate

2.1.1 Macroelectrodes and Microelectrodes

As already given in Chap. 1, the most frequently used form of the cathodic polarization curve equation for flat or large spherical electrode of massive metal is given by:

$$i = \frac{i_0(f_c - f_a)}{1 + \frac{i_0 f_c}{i_L}} \tag{1.13}$$

where i, i_0, and i_L are the current density, exchange current density, and limiting diffusion current density, respectively, and

$$f_c = 10^{\frac{\eta}{b_c}} \text{ and } f_a = 10^{-\frac{\eta}{b_a}} \tag{1.37}$$

where b_c and b_a are the cathodic and anodic Tafel slopes and η is the overpotential. Equation (1.13) is modified for use in electrodeposition of metals by taking cathodic current density and overpotential as positive. Derivation of the Eq. (1.13) is performed under assumption that the concentration dependence of i_0 can be neglected [1–4].

The electrochemical processes on microelectrodes in bulk solution can be under activation control at overpotentials which correspond to the limiting diffusion current density plateau of the macroelectrode. The cathodic limiting diffusion current density for steady-state spherical diffusion, $i_{L,spher}$, is given by:

$$i_{L,spher} = \frac{nFDC_0}{r_{el}} \tag{1.11}$$

and for steady-state linear diffusion, i_L, by:

$$i_L = \frac{nFDC_0}{\delta} \tag{1.14}$$

It follows from Eqs. (1.11) and (1.14) that

$$\frac{i_{L,\text{spher}}}{i_L} = \frac{\delta}{r_{\text{el}}} \tag{2.1}$$

An electrode around which the hydrodynamic diffusion layer can be established, being considerably lower than dimensions of it, could be considered as a macroelectrode. An electrode, mainly spherical, whose diffusion layer is equal to the radius of it, satisfying

$$\delta \gg r_{\text{el}} \tag{2.2}$$

can be considered as a microelectrode [5].

According to the Eq. (1.13) for $f_c \gg f_a$ and

$$\frac{i_0 f_c}{i_L} \gg 1 \tag{2.3}$$

the cathodic process on the macroelectrode enters full diffusion control, *i.e.*,

$$i = i_L \tag{1.35}$$

Simultaneously, the cathodic current density on the spherical microelectrode, i_{spher}, is given by[1]:

$$i_{\text{spher}} = \frac{i_0(f_c - f_a)}{1 + \frac{i_0 f_c}{i_{L,\text{spher}}}} \tag{1.12}$$

or, because of the Eq. (2.1):

$$i_{\text{spher}} = \frac{i_0(f_c - f_a)}{1 + \frac{i_0}{i_L} \cdot \frac{r_{\text{el}}}{\delta} \cdot f_c} \tag{2.4}$$

and if a condition of the Eq. (2.3) is also valid, but

---

[1] The reversible potential of a surface with radius of curvature r_{cur} would depart from that of a planar surface by the quantity $\Delta E_r = 2\gamma V/(nFr_{\text{cur}})$, where γ is the interfacial energy between metal and solution and V molar volume of metal [5]. It is valid at extremely low r_{cur}, being of the order of few millivolts, and it can be neglected except in some special cases, like the stability of the shape of the tips of dendrites [5].

$$\frac{r_{el}}{\delta} \to 0 \tag{2.5}$$

the Eq. (2.4) can be rewritten in the form

$$i = i_0 f_c \tag{2.6}$$

This means that the process on the microelectrode in the bulk solution can be under complete activation control at the same overpotential at which the same process on the macroelectrode is simultaneously under full diffusion control.

The different behavior of macroelectrodes and microelectrodes under the same conditions of electrodeposition causes the disperse deposit formation.

2.1.2   Active Microelectrodes Placed Inside Diffusion Layer of the Active Macroelectrode

2.1.2.1   Mathematical Model

Naturally, the microelectrodes can be placed on the macroelectrodes inside their diffusion layers. Let us consider the model of surface irregularities shown in Fig. 2.1. The electrode surface irregularities are buried deep in the diffusion layer, which is characterized by a steady linear diffusion to the flat portion of the surface [1, 6, 7], and the limiting diffusion current density is given by Eq. (1.14).
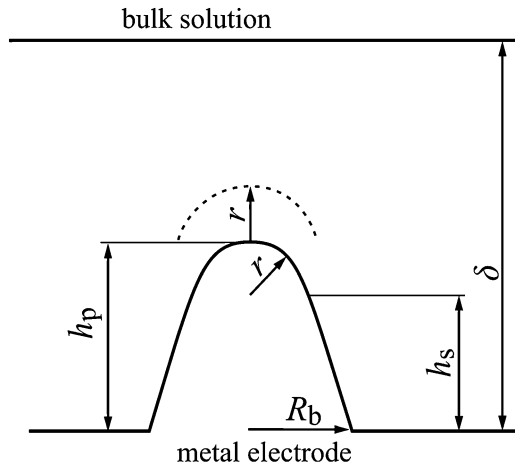

Fig. 2.1 Model of a paraboloidal surface protrusion; h_p is the height of the protrusion relative to the flat portion of the surface, h_s is the corresponding local side elongation, r is the radius of the protrusion tip, R_b is the radius of the protrusion base, and δ is the thickness of the diffusion layer and $\delta \gg h_p$ (Reprinted from Refs. [1, 8] with kind permission from Springer and Ref. [6] with permission from Elsevier)

At the side of an irregularity, the limiting diffusion current density, $i_{L,s}$, is given as:

$$i_{L,s} = \frac{nFDC_0}{\delta - h_s} = i_L \frac{\delta}{\delta - h_s} \tag{2.7}$$

Obviously, this is valid if the protrusion height does not affect the outer limit of the diffusion layer, and if a possible lateral diffusion flux supplying the reacting ions can be neglected. At the tip of an irregularity, the lateral flux cannot be neglected and the situation can be approximated by assuming a spherical diffusion current density, $i_{L,tip}$, given by the Eq. (2.8) [7]:

$$i_{L,tip} = \frac{nFDC^*}{r} \tag{2.8}$$

where C^* is the concentration of the diffusing species at a distance r from the tip, assuming that around the tip a spherical diffusion layer having a thickness equal to the radius of the protrusion tip is formed [5]. Obviously, if $r > \delta$, the spherical diffusion layer around the tip of protrusion cannot be formed and the Eq. (2.9) is valid:

$$i_{L,tip} = \frac{nFDC_0}{\delta - h_p} \tag{2.9}$$

If deposition to the macroelectrode is under full diffusion control, the distribution of the concentration C inside the linear diffusion layer is given by the Eq. (2.10) [3]:

$$C = C_0 \frac{h_{difl}}{\delta} \tag{2.10}$$

where $0 \leq h_{difl} \leq \delta$. Hence,

$$C^* = C_0 \frac{h_p + r}{\delta} \tag{2.11}$$

and

$$i_{L,tip} = i_L \left(1 + \frac{h_p}{r}\right) \tag{2.12}$$

because of Eqs. (1.14), (2.8), and (2.11).

The tip radius of the paraboloidal protrusion is given by the Eq. (2.13) [3, 5, 9]:

$$r = \frac{R_b^2}{2h_p} \tag{2.13}$$

and substitution of r from the Eq. (2.13) in the Eq. (2.12) gives

$$i_{L,tip} = i_L \left(1 + \frac{2h_p^2}{R_b^2}\right) \tag{2.14}$$

or

$$i_{L,tip} = i_L \left(1 + 2k_p^2\right) \tag{2.15}$$

where

$$k_p = \frac{h_p}{R_b} \tag{2.16}$$

If $h_p = R_b, k_p = 1$, hence for a hemispherical protrusion is

$$i_{L,tip} = 3i_L \tag{2.17}$$

If $h_p << R_b, k_p \to 0$, and

$$i_{L,tip} \to i_L \tag{2.18}$$

and if $R_b << h_p, k_p \to \infty$ and

$$i_{L,tip} \to \infty \tag{2.19}$$

Substitution of $i_{L,tip}$ from Eq. (2.15) instead of i_L in Eq. (1.13) and further rearranging give Eq. (2.20):

$$i_{tip} = \frac{i_0(f_c - f_a)}{1 + \frac{i_0}{i_L} \cdot \frac{1}{1 + 2k_p^2} f_c} \tag{2.20}$$

The current density on the tip of a protrusion, i_{tip}, is determined by k_p, hence by the shape of the protrusion. If $k_p \to 0, i_{tip} \to i$ (see the Eq. (1.13)) and if $k_p \to \infty$, $i_{tip} \to i_0 (f_c - f_a) >> i$. The electrochemical process on the tip of a sharp needle-like protrusion can be under pure activation control outside the diffusion layer of the macroelectrode. Inside it, the process on the tip of a protrusion is under mixed control, regardless it is under complete diffusion control on the flat part of the electrode for $k_p \to 0$ (see section "Model of the spherical diffusion around the tip of a surface protrusion–deposition to the point"). If $k_p = 1$, hence for hemispherical protrusion, i_{tip} will be somewhat larger than i, but the kind of control will not be changed. It is important to note that the current density to the tip of hemispherical protrusion does not depend on the size of it if $k_p = 1$. This makes a substantial difference between spherical microelectrodes in bulk solution and microelectrodes inside diffusion layer of the macroelectrode [3, 9, 10]. In the first case, the limiting diffusion current density depends strongly on the radius of the microelectrode.

Fig. 2.2 Models of
surfaces with (**a**) the same
surface roughness and
different coarseness and
(**b**) vice versa (Reprinted
from Ref. [11] with kind
permission from Springer)

Fig. 2.2 Models of surfaces with (a) the same surface roughness and different coarseness and (b) vice versa (Reprinted from Ref. [11] with kind permission from Springer)
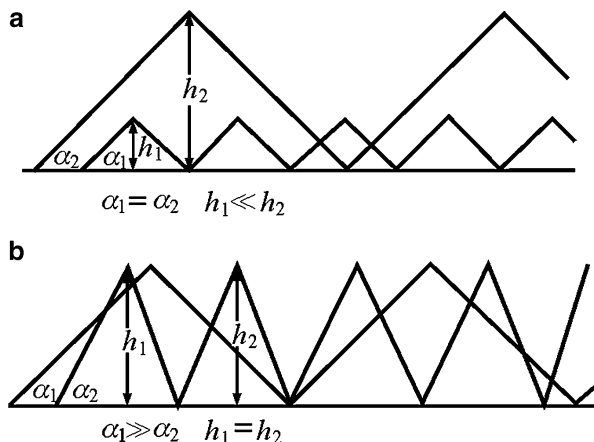
Electrode Surface Coarseness

Any solid metal surface that represents a substrate for metal deposition possesses a certain roughness. In addition, it may appear coarse or smooth, and this is not necessarily related to the roughness. Figure 2.2 shows cases of surfaces with (a) the same roughness and profoundly different coarseness and (b) vice versa.

It is the level of coarseness which determines the appearance of metal deposits, while even with considerable roughness, if below the visual level, the surface may appear smooth.

It is convenient to define the surface coarseness as the difference in thickness of the metal at the highest and lowest points above an arbitrary reference plane facing the solution.

Non-dendritic Amplification of Surface Coarseness

The current densities, i_s and i_{tip} to different points at the electrode surface, can be obtained by substitution of i_L in the Eq. (1.13) by appropriate values from the Eqs. (2.7) and (2.12) for the side and the tip of the protrusion, around which the spherical diffusion layer is formed, respectively. Hence:

$$i_s = \frac{i_0(f_c - f_a)}{1 + \left(\frac{i_0 f_c}{i_L}\right)\left(\frac{\delta - h_s}{\delta}\right)} \tag{2.21}$$

and if the spherical diffusion layer around the tip of a protrusion can be formed ($r < \delta$), it will be valid as in Eq. (2.22):

$$i_{tip} = \frac{i_0(f_c - f_a)}{1 + \left(\frac{i_0 f_c}{i_L}\right)\left(\frac{r}{r + h_p}\right)} \tag{2.22}$$

However, if the spherical diffusion layer around the tip of a protrusion cannot be formed ($r > \delta$), it will be valid:

$$i_{\text{tip}} = \frac{i_0(f_c - f_a)}{1 + \left(\frac{i_0 f_c}{i_L}\right)\left(\frac{\delta - h_p}{\delta}\right)} \tag{2.23}$$

The effective rate of growth of the side elevation is equal to the rate of motion of the side elevation relative to the rate of motion of the flat surface [11]. Hence:

$$\frac{dh_s}{dt} = \frac{V}{nF}(i_s - i) \tag{2.24}$$

and substitution of i_s from the Eq. (2.21) and i from the Eq. (1.13) in the Eq. (2.24) and further rearrangement give the Eq. (2.25) [12]:

$$\frac{dh_s}{dt} = \frac{i^2 V h_s}{i_L nF\delta} \tag{2.25}$$

if $\delta >> h_s$ and $f_c >> f_a$, or in the integral form:

$$h_s = h_{0,s}\exp\left(\frac{i}{i_L}\frac{Q}{Q_{0,D}}\right) \tag{2.26}$$

where $h_{0,s}$ is the initial height of the local side elevation (see also Eqs. (2.32), (2.33), and (2.34)) and Q is given by the Eq. (2.27):

$$Q = i \cdot t \tag{2.27}$$

and

$$Q_{0,D} = \frac{nF\delta}{V} \tag{2.28}$$

Hence, an increase in the surface coarseness can be expected with increasing quantity of deposited metal for the same deposition current density, as well as with increasing current density for the same quantity of electrodeposited metal.

In the same way, the propagation rate of the protrusion tip can be obtained by substituting i_{tip} from the Eq. (2.22) and i from the Eq. (1.13) into the Eq. (2.24), where i_s and h_s are substituted by i_{tip} and h_p, on further rearrangement the following expression is obtained:

$$\frac{dh_p}{dt} = \frac{V i \, i_{tip} h_p}{nF i_L (r + h_p)} \tag{2.29}$$

It should be noted that the Eq. (2.29) is only valid if the radius of the protrusion tip is sufficiently large to make the surface energy term negligible [5].

It is obvious from Eqs. (2.25) and (2.29) that

$$\frac{dh_p}{dt} > \frac{dh_s}{dt} \tag{2.30}$$

because $i_{tip} > i$ and $h_p/(r + h_p) > h_s/\delta$, which means that the tip propagation protrusion will be larger under spherical diffusion control.

2.1.2.2　Physical Model

To test the validity of the above equations, Popov et al. [7, 11, 13, 14] carried out experiments on diffusion-controlled metal electrodeposition on a well-defined, triangularly shaped surface profile, through a diffusion layer of well-defined thickness $\delta >> h_p$. A phonograph disk negative was used as the substrate upon which a layer of an agar-containing copper sulfate–sulfuric acid solution was placed and left to solidify, as illustrated in Fig. 2.3a.

As current was passed and the layer was depleted of copper ions, an increase in the height of the triangular ridges was observed. Metallographic samples were made in wax, and the cross sections of the deposit were photographed under a microscope (Fig. 2.3b) [14]. The three parts of the surface can be noticed in Fig. 2.3b: the flat part of the electrode surface and the sides and the tips of irregularities, providing an excellent physical illustration of the mathematical model.
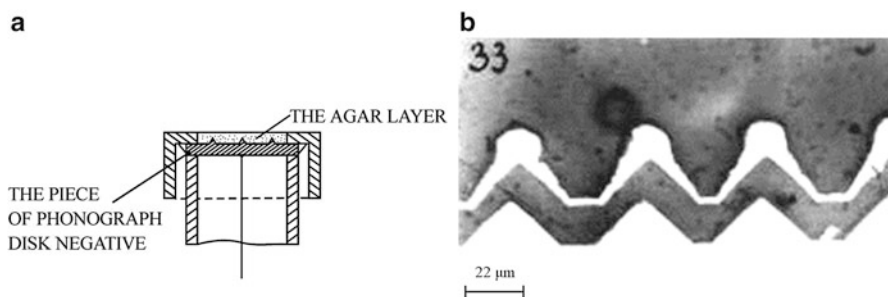

Fig. 2.3 (**a**) The model of an electrode for diffusion-controlled electrodeposition of metals and (**b**) cross section of Cu deposit obtained from 0.50 M $CuSO_4$ in 0.50 M H_2SO_4 in a system from (**a**). The thickness of the agar diffusion layer was 1.0 mm. Deposition overpotential: 300 mV; deposition time: 120 min. The substrate is a piece of a phonograph disk negative (Reprinted from Refs. [7, 11, 13] with kind permission from Springer)

2.1.2.3 Real Systems

The Effect of the Deposition Current Density on the Electrode Surface Coarseness

The effect of deposition current density on the increase in surface coarseness for a fixed quantity of electrodeposited metal is illustrated by Fig. 2.4. As expected, the surface coarseness increases strongly with the increasing current density in the region of mixed activation–diffusion control where obtained deposits are polycrystalline (Fig. 2.4b, c) [15, 16]. It should be noted that the theories describing the increase of electrode surface coarseness are valid for $h_p \ll \delta$, *i.e.,* for the short deposition times. For qualitative investigations, the effect of current density on the increase of surface coarseness and large quantities of metal were used, as it was assumed that the qualitative picture of the phenomenon would not be changed. In quantitative investigations, the deposition times in which the approximation $\delta \gg h_p$ is valid [17] must be determined and taken into account. In the region of the activation-controlled electrodeposition, at the same initial surface, the situation is quite different as can be seen from Fig. 2.4a.

The Deposits with a Minimal Coarseness

Activation-controlled deposition of copper produces large grains with relatively well-defined crystal shapes. This can be explained by the fact that the values of the
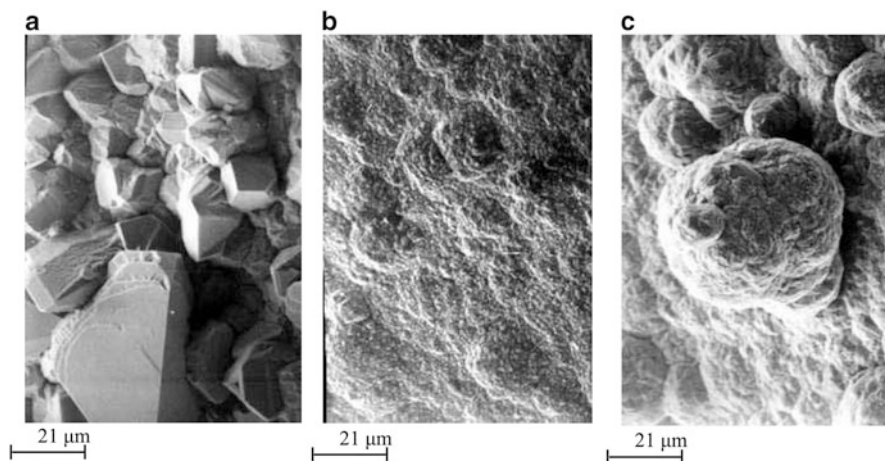

Fig. 2.4 Copper deposits obtained from 0.10 M $CuSO_4$ in 0.50 M H_2SO_4. Quantity of electricity, Q: 20 mA h cm^{-2}: (**a**) activation-controlled electrodeposition: $\eta = 90$ mV, initial current density: 3.3 mA cm^{-2}, (**b**) mixed activation–diffusion-controlled electrodeposition: $\eta = 140$ mV, initial current density: 4.2 mA cm^{-2}, and (**c**) dominant diffusion-controlled electrodeposition: $\eta = 210$ mV, initial current density: 6.5 mA cm^{-2} (Reprinted from Refs. [7, 8, 13] with kind permission from Springer and Ref. [16] with permission from Elsevier)

exchange current densities on different crystal planes are quite different, whereas the reversible potential is approximately the same for all planes [13, 18]. This can lead to preferential growth of some crystal planes, because the rate of deposition depends only on the orientation, which leads to the formation of a large-grained rough deposit. However, even at low degrees of diffusion control, the formation of large, well-defined grains is not to be expected, because of irregular growth caused by mass-transport limitations. Hence, the current density which corresponds to the very beginning of the mixed control (a little larger than this at the end of the Tafel linearity) will be the optimum one for compact metal deposition [13, 16].

All the above facts are illustrated in Fig. 2.4 [13, 16].

Cauliflower-Like Forms

It can be seen from Fig. 2.4c that the surface protrusions are globular and cauliflower-like ones. If the initial electrode surface protrusions are of ellipsoidal shape, they can be characterized by the base radius R_0 and the height h_p as shown in Fig. 2.5a [13, 19].

The tip radius is then given by:

$$r = \frac{R_0^2}{h_p} \tag{2.31}$$

The initial electrode surface protrusion is characterized by $h_p \to 0$ and $r \to \infty$ if $R_0 \neq 0$. In this situation, a spherical diffusion layer cannot be formed around the tip of the protrusion if $r > \delta$, and if the linear diffusion control occurs, leading to an increase in the height of the protrusion relative to the flat surface.

The rate of growth of the tip of a protrusion for $r > \delta$ is equal to the rate of motion of the tip relative to the rate of motion of the flat surface. Hence, in the diffusion-controlled electrodeposition:

$$\frac{dh_p}{dt} = \frac{V}{nF}\left(i_{L,tip} - i_L\right) \tag{2.32}$$

Substitution of $i_{L,tip}$ from the Eq. (2.9) and i_L from the Eq. (1.14) in the Eq. (2.32) and further rearranging gives

$$\frac{dh_p}{dt} = \frac{i^2 V h_p}{i_L nF\delta} \tag{2.33}$$

or

$$h_p = h_{p,0}\exp\left(\frac{i}{i_L}\frac{Q}{Q_{0,D}}\right) \tag{2.34}$$

where Q and $Q_{0,D}$ are given by Eqs. (2.27) and (2.28).
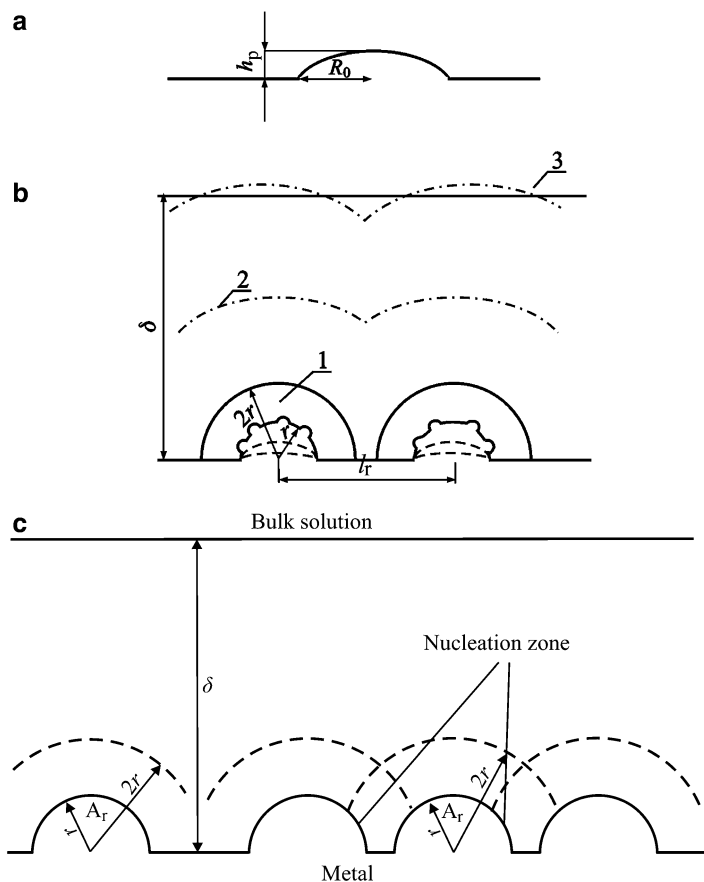
Fig. 2.5 Schematic representations of (**a**) the initial electrode surface protrusion, (**b**) the establishment of spherical diffusion layers around independently growing protrusions (1. $r < (\delta - h_p)$ and $r < 1/4l_r$ spherical diffusion zones are formed; 2. $r < (\delta - h_p)$ and $r > 1/4l_r$ spherical diffusion zones overlap); 3. $r > (\delta - h_p)$, spherical diffusion zones are not formed, and (**c**) spherical diffusion layers and their overlap around growing protrusions (Reprinted from Refs. [7, 8, 13] with kind permission from Springer and Ref. [19] with permission from the Serbian Chemical Society)

If the surface protrusions are sufficiently far one from other, then the spherical diffusion control can be operative around the whole surface of protrusion when h_p increases and r decreases, as illustrated by Fig. 2.5b. In this situation, second-generation protrusions can grow inside the diffusion layer of first-generation protrusions in the same way as first-generation protrusions grow inside the diffusion layer of the macroelectrode, and so on.

A cauliflower-like deposit is formed under such conditions, as is shown in Fig. 2.6a, b. It can be seen from Fig. 2.6a that the distance between the cauliflower-like grains is sufficiently large to permit the formation of spherical diffusion zones around each of them. Simultaneously, second-generation
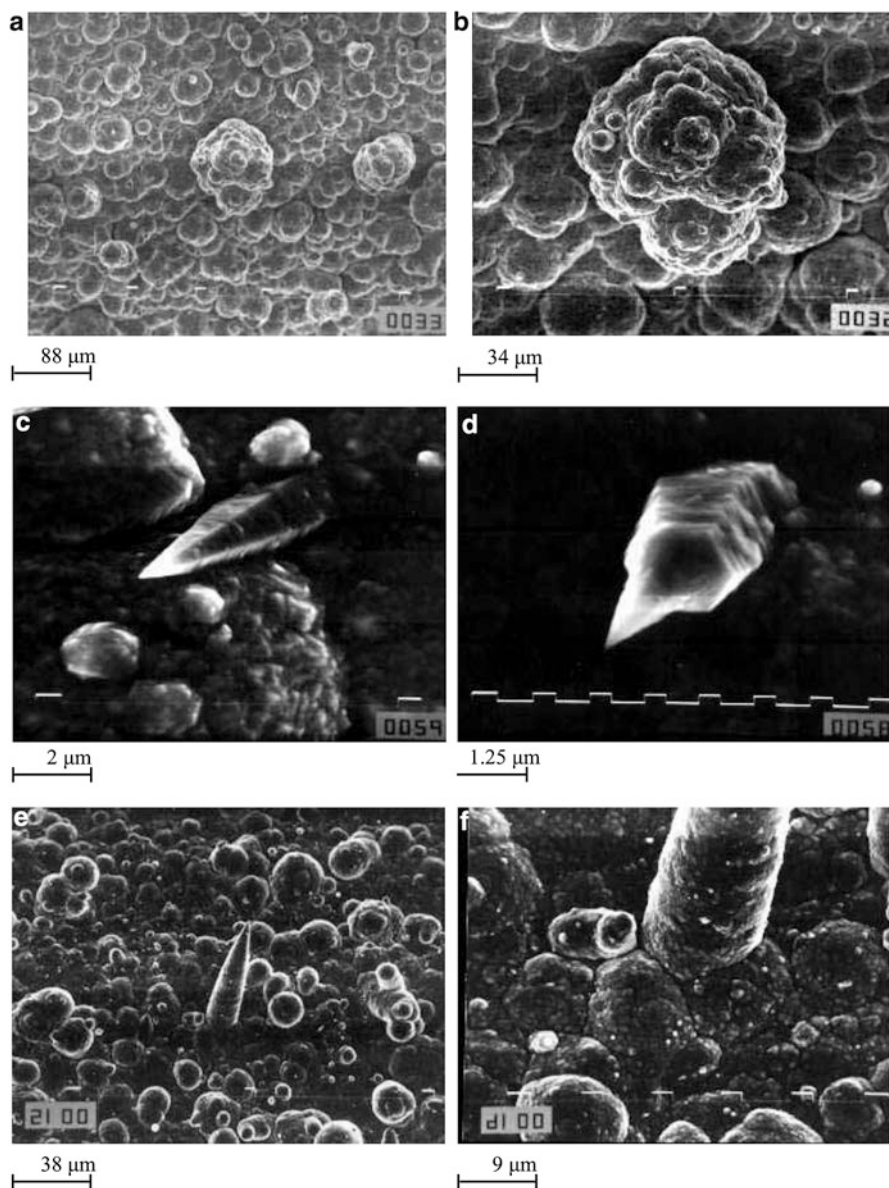
Fig. 2.6 Copper deposits obtained from 0.30 M $CuSO_4$ in 0.50 M H_2SO_4 by electrodeposition under mixed activation–diffusion control. Deposition overpotential: 220 mV. Quantity of electricity: (**a**) 40 mA h cm^{-2}, (**b**) the same as in (**a**), (**c**) 10 mA h cm^{-2}, (**d**) 10 mA h cm^{-2}, (**e**) 20 mA h cm^{-2}, and (**f**) the root of the carrot from (**e**) (Reprinted from Refs. [7, 8, 13] with kind permission from Springer and Ref. [20] with permission from the Serbian Chemical Society)

protrusions grow in all directions, as shown in Fig. 2.6b. This confirms the assumption that the deposition takes place in a spherically symmetric fashion.

To a first approximation, the rate of propagation can be taken to be practically the same in all directions, meaning that the cauliflower-type deposit formed by spherically symmetric growth inside the diffusion layer of the macroelectrode will be hemispherical, as is illustrated in Fig. 2.6a, b.

This type of protrusion is much larger than that formed by linearly symmetric growth inside the diffusion layer of the macroelectrode (Fig. 2.6a, b).

This is because a spherical diffusion layer cannot be formed around closely packed protrusions, their diffusion fields overlap, and they grow in the diffusion layer of the macroelectrode.

Carrot-Like Forms

If spherical diffusion layer can be established around the tip of a protrusion, the limiting diffusion current to the tip is given by Eq. (2.12) or by:

$$i_{L,tip} = i_L \frac{h_p}{r} \tag{2.35}$$

for

$$\frac{h_p}{r} >> 1 \tag{2.36}$$

It can also be seen from Fig. 2.6c–f that the growth of such protrusions produces carrot-like forms, another typical form obtained in copper deposition under mixed activation–diffusion control. This happens under the condition $k_p << 1$, when activation control takes place only around the tip of the protrusion, as is illustrated in Fig. 2.6c, d. In this case, Eq. (2.20) can be rewritten in the form:

$$i_{tip} = i_{0,tip}(f_c - f_a) \tag{2.37}$$

meaning that deposition on the protrusion tip can also be under activation control at overpotentials lower than the critical one for the initiation of dendritic growth (see section "Model of the spherical diffusion around the tip of a surface protrusion–deposition to the point").

This happens if the nuclei have a shape like that in Fig. 2.6c, d. The assumption that the protrusion tip grows under activation control is confirmed by the regular crystallographic shape of the tip [20] just as in the case of grains growing on the macroelectrode under activation control (see Fig. 2.4a).

The maximum growth rate at a given overpotential corresponds to activation-controlled deposition. As a result, the propagation rate at the tip will be many times larger than that in other directions, resulting in protrusions like that in Fig. 2.6e.

The final form of the carrot-like protrusion is shown in Fig. 2.6e. It can be concluded from the parabolic shape that such protrusions grow as moving paraboloids in accordance with the Barton–Bockris theory [5], the tip radius remaining constant because of the surface energy effect. It can be concluded from Fig. 2.6f that thickening of such a protrusion is under mixed activation–diffusion control because the deposit is seen to be of the same quality as that on the surrounding macroelectrode surface. It can be seen from the Fig. 2.6d that activation control takes place only at the very tip of the protrusion.

The Position of New Nuclei

It is seen from Fig. 2.6c, d that new nuclei are mainly formed at the bottom of the already growing protrusions or between them. If the diffusion zones of two or more hemispherical protrusions partially overlap, as illustrated by Fig. 2.5c, the current densities i at each point outside the overlapping field will be those required by Eq. (2.38):

$$\eta = b_c \log\left(\frac{i}{i_0}\right) + b_c \log\left(\frac{1}{1 - \frac{i}{i_L}}\right) \tag{2.38}$$

for $f_c \gg f_a$ and where i_L is the limiting diffusion current density (linear or spherical).

In the overlapping field, the current density i' at the points where the maximum possible current density is i in the absence of overlapping field will be lower than i. In this way, the substrate becomes partially inert, and the formation of new nuclei is enhanced at these points if the entire electrode surface is at same potential because

$$\eta = b_c \log\left(\frac{i'}{i_0}\right) + b_c \log\left(\frac{1}{1 - \frac{i'}{i_L}}\right) + \Delta\eta \tag{2.39}$$

where $\Delta\eta$ is the nucleation overpotential [7, 19].

Some of the new nuclei are the precursors of carrot-like protrusions, depending on their crystal orientation. In this case, they are in the form of small hexagonal pyramids, as shown in Fig. 2.6c, d. Based on their morphology and because copper has a face-centered cubic crystal structure, it is reasonable to assume that they are truncated by a high-Miller index plane. According to Pangarov and Vitkova [21, 22], the orientation of nuclei is related to the overvoltage used. It is reasonable to expect that the appearance of precursors of carrot-like protrusions has its own overvoltage range.

Different Possible Forms

The tips of growing carrot-like protrusions can change the direction of protrusions. This is mainly observed in a later stage of protrusion growth. Thus, the smaller the protrusion height, the lower is the probability of a change in the growth direction. The reason for this behavior is not yet clear. However, it is probably caused by local perturbations on the growth front on the protrusion tip. This effect and the further nucleation on already growing protrusions cause the growth of different forms.

   The growth of surface protrusions in galvanostatic deposition has been considered only for deposition in the limiting diffusion current density range [23, 24].

   In summary, deposition under mixed activation–diffusion control causes the formation of a number of growth forms and the increase of surface coarseness, this increase being more pronounced at higher current densities. It should be noted that electrodeposition at a periodically changing rate can change considerably the morphology of the deposits [13, 25].

2.1.3   Dendritic Deposits

2.1.3.1   Basic Facts

Two phenomena seem to distinguish dendritic from carrot-like growth [7, 11, 13]:

1. A certain well-defined critical overpotential value appears to exist below which dendrites do not grow.
2. Dendrites exhibit a highly ordered structure and grow and branch in well-defined directions. According to Wranglen [26], a dendrite is a skeleton of a monocrystal and consists of a stalk and branches, thereby resembling a tree.

   It is known that dendritic growth occurs selectively at three types of growth sites [11]:

   (a) Dendritic growth occurs at screw dislocations. Swordlike dendrites with pyramidal tips are formed by this process [3, 11].
   (b) Many investigations of the crystallographic properties of dendrites have reported the existence of twin structures [27–30]. In the twinning process, a so-called indestructible reentrant groove is formed. Repeated one-dimensional nucleation in the groove is sufficient to provide for growth extending in the direction defined by the bisector of the angle between the twin planes [11].
   (c) It is a particular feature of a hexagonal close-packed lattice that growth along a high-index axis does not lead to the formation of low-index planes. Grooves containing planes are perpetuated, and so is the chance for extended growth by the one-dimensional nucleation mechanism [31].

In all the above cases, the adatoms are incorporated into the lattice by repeated one-dimensional nucleation. On the other hand, deposition to the tip of screw

dislocations can be theoretically considered as deposition to a point; in the other two cases, the deposition is to a line. Hence, in the case under (a), the conditions of spherical diffusion are fulfilled, while the conditions of the cylindrical diffusion are fulfilled in the case under (b).

From the electrochemical point of view, a dendrite can be defined as an electrode surface protrusion that grows under activation or mixed control, while deposition to the flat part of the electrode surface is under complete diffusion control [3, 7, 9, 11, 13].

2.1.3.2   Dendrite Precursors: Schematic Presentation

The monoatomic high-step edges, the microsteps, are required for continuous metal electrocrystallization. Possible sources of microsteps on a surface are shown in Figs. 2.7, 2.8a, and 2.9a, *i.e.,* the low-index planes, two-dimensional nuclei, emergent screw dislocations, and indestructible reentrant grooves [11, 32].
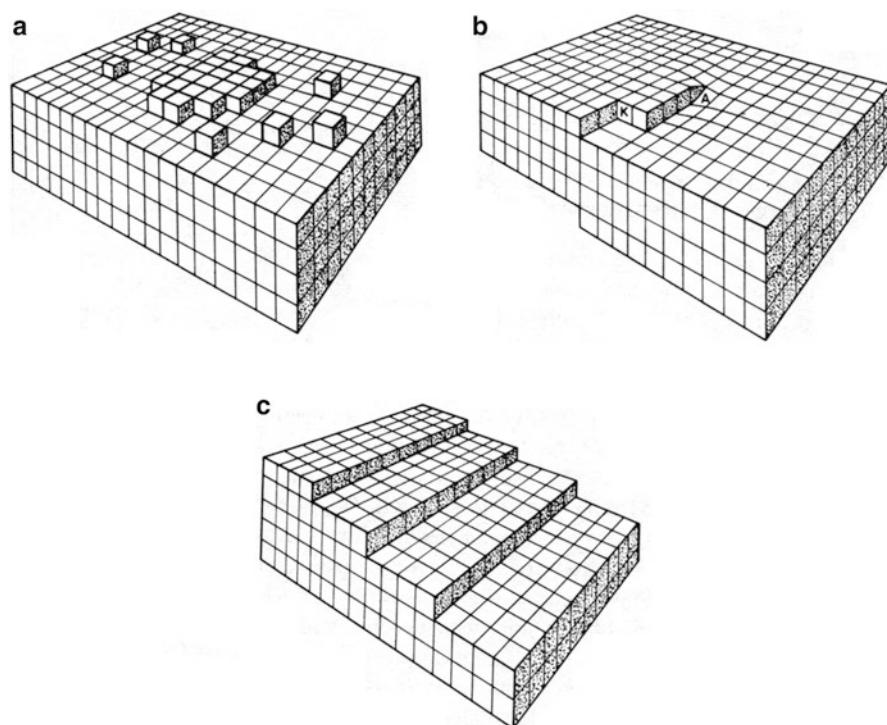

Fig. 2.7 Models of different sources of microsteps on a surface: (**a**) a two-dimensional nucleus, (**b**) an emergent screw dislocation, (**c**) misorientation of the surface with respect to the ideal low-index plane (Reprinted from Refs. [13, 32] with kind permission from Springer)
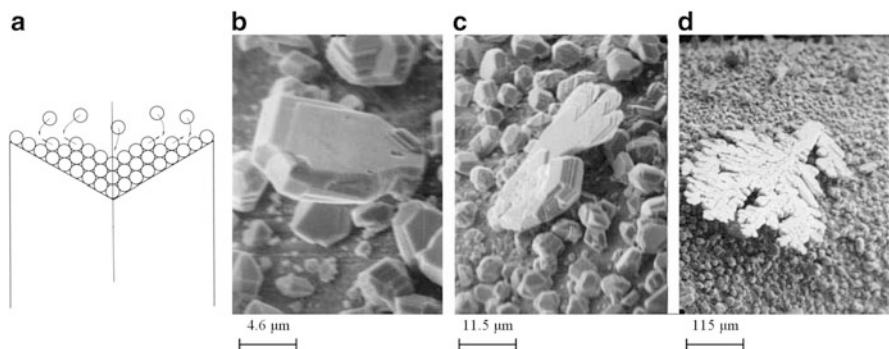
Fig. 2.8 (**a**) Schematic representation of the formation of an "indestructible reentrant groove" and the cadmium deposits obtained by deposition from 0.10 M $CdSO_4$ in 0.50 M H_2SO_4 onto a cadmium electrode. Deposition overpotential: 50 mV. Deposition times: (**b**) 2 min, (**c**) 2 min, and (**d**) 10 min (Reprinted from Refs. [7, 11, 13] with kind permission from Springer and Ref. [33] with permission from Elsevier)
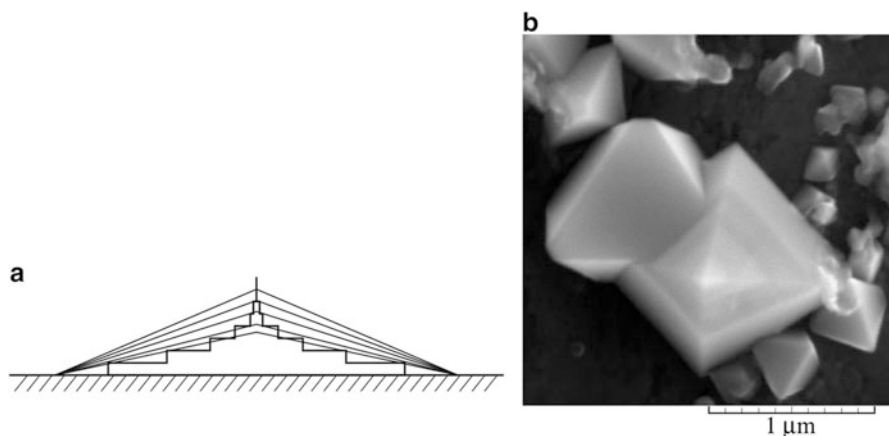

Fig. 2.9 (**a**) Schematic representation of the growth at screw dislocation and (**b**) the initial stage of Pb electrodeposition from 0.40 M $Pb(NO_3)_2$ in 2.0 M $NaNO_3$ at an overpotential of 100 mV with a time of 0.5625 s (According to [3] and reprinted from Ref. [34] with permission from Elsevier)

It is obvious from Fig. 2.7a, c that after the formation of a low-index plane, two-dimensional nucleation is necessary for the growth to be continued.

In the case of a reentrant groove (Fig. 2.8a), the growth of new layers can be started by one-dimensional nucleation. The growth rates in the cases of one-dimensional and two-dimensional nucleation as rate-determining steps can be compared to each other by considering the growth of two-dimensional flat cadmium dendrites from Fig. 2.8b–d.

The tip of the twined cadmium dendrite precursor from Fig. 2.8b represents the physical equivalent of the scheme of the growth site from Fig. 2.8a. As shown in Fig. 2.8a, a layer of atoms advance in the direction determined by twining laws, an edge is constantly renewed, in which the new layers can be started by one-dimensional nucleation. Further growth and branching of precursor like that from Fig. 2.8b produces the dendrites shown in Fig. 2.8c, d. The deposition on the lateral flat dendrite surfaces takes place by repeated two-dimensional nucleation, as in deposition on dislocation free surface [33]. This makes the deposition rate in the direction of tip motion many times larger, which results in dendrite shape like that from Fig. 2.8d.

In the case of a screw dislocation (Fig. 2.9a), the step provokes the growth by retaking itself with one end fixed at the point where the screw dislocation emerges. The initial stage of growth at the screw dislocation is shown in Fig. 2.9b. The needle-like dendrites as those shown in Fig. 1.8b, c are formed by this type of growth [34].

Aside from dendrites of the different shapes [34, 35], during electrodeposition of Pb in the diffusion control, crystals of irregular shapes were also formed (Fig. 2.10). These irregular crystals do not follow the classical Wranglen definition of a dendrite [26], but they behave as dendrites with regard to their electrochemical characteristics. For this reason, these crystals formed under diffusion control are denoted as precursors of dendrites [34].
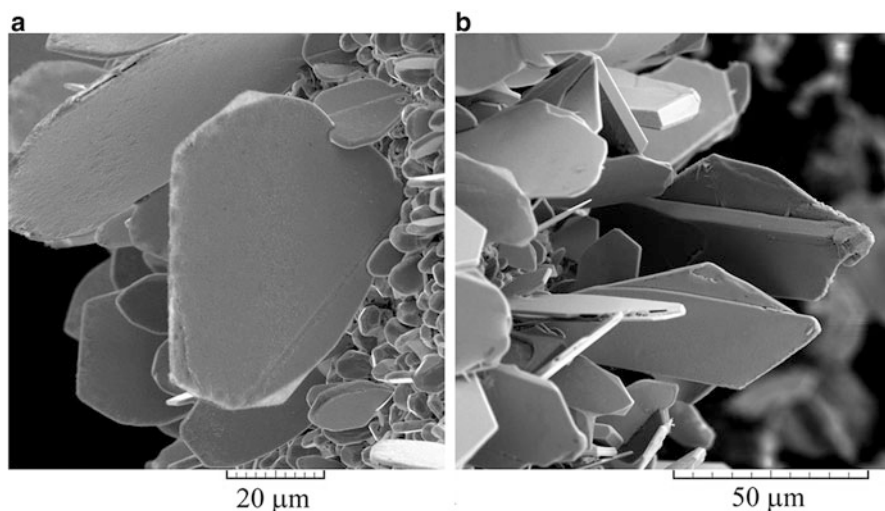

Fig. 2.10 Lead crystals formed by electrodeposition from 0.40 M $Pb(NO_3)_2$ in 2.0 M $NaNO_3$ at overpotentials of (**a**) 50 mV and (**b**) 75 mV with quantity of the electricity of 0.95 mA h cm^{-2} (Reprinted from Ref. [36] with permission from the Serbian Chemical Society)

2.1.3.3 Mathematical Model Considering the Conditions of Spherical and Cylindrical Diffusion

Model of the Spherical Diffusion Around the Tip of a Surface
Protrusion–Deposition to the Point

Considering the model of surface irregularities shown in Fig. 2.1, the surface irregularities are buried deep in the diffusion layer, which is characterized by a steady linear diffusion to the flat portion of completely active surface and by the spherical diffusion field formed around the tip of a surface protrusion. The conditions of spherical diffusion are fulfilled around the tips of both needle-like protrusion (Fig. 2.9b) and irregular crystals (Fig. 2.10b).

If the protrusion does not affect the outer limit of the diffusion layer, *i.e.*, if $\delta \gg h_p$, the limiting diffusion current density to the tip of the protrusion from Fig. 2.1, $i_{L,tip}$, is given by:

$$i_{L,\,tip} = i_L \left(1 + \frac{h_p}{r} \right) \tag{2.12}$$

Substitution of $i_{L,tip}$ from Eq. (2.12) into Eq. (1.13) produces for $h_p/r \gg 1$:

$$i_{tip} = i_{0,\,tip}(f_c - f_a) \tag{2.37}$$

where $i_{0,tip}$ is the exchange current density at the tip of a protrusion.

Obviously, deposition to the tip of such protrusion inside the diffusion layer is activation-controlled relative to the surrounding electrolyte, but it is under mixed activation–diffusion control relative to the bulk solution.

If deposition to the flat part of electrode is diffusion-controlled process and assuming a linear concentration distribution inside diffusion layer (see Eq. (2.10)), the concentration C_{tip} at the tip of a protrusion can be given:

$$C_{tip} = C_0 \frac{h_p}{\delta} \tag{2.40}$$

According to Newman [37], the exchange current density at the tip of a protrusion, $i_{0,tip}$, is given by:

$$i_{0,\,tip} = i_0 \left(\frac{C_{tip}}{C_0} \right)^{\xi} \tag{2.41}$$

where

$$\xi = \frac{d \log i_0}{d \log C_0} \tag{1.17}$$

or

$$i_{0,\text{tip}} = i_0 \left(\frac{h_p}{\delta}\right)^{\xi} \tag{2.42}$$

because of Eq. (2.40).

Taking into account the Eq. (2.37), the current density to the tip of a protrusion is then given by:

$$i_{\text{tip}} = i_0 \left(\frac{h_p}{\delta}\right)^{\xi} (f_c - f_a) \tag{2.43}$$

being under mixed control due to the $(h_p/\delta)^{\xi}$ term, which takes into account the concentration dependence of $i_{0,\text{tip}}$, expressing in this way a mixed controlled electrodeposition process.

Outside the diffusion layer $h_p \geq \delta$, and the Eq. (2.43) becomes:

$$i_{\text{tip}} = i_0 (f_c - f_a) \tag{2.44}$$

indicating pure activation control, as the $(h_p/\delta)^{\xi}$ term is absent.

For the dendrite growth, the current density to the tip of a protrusion formed on the flat part of the electrode surface growing inside the diffusion layer should be larger than the corresponding limiting diffusion current density [38]. Hence, if

$$i_L < i_{\text{tip}} \tag{2.45}$$

the protrusion grows as a dendrite.

In accordance with the Eq. (2.45), instantaneous dendrite growth is possible after reach of steady-state conditions at overpotentials larger than some critical value, η_c, which can be derived from the Eq. (2.43) as shown in Refs [7, 13, 38]:

$$\eta_c = \frac{b_c}{2.3} \ln \frac{i_L}{i_0} \left(\frac{\delta}{h_p}\right)^{\xi} \tag{2.46}$$

and minimum overpotential at which dendritic growth is still possible, for $h_p = \delta$, η_i is given by:

$$\eta_i = \frac{b_c}{2.3} \ln \frac{i_L}{i_0} \tag{2.47}$$

for $f_c \gg f_a$. For very fast processes, when $i_0/i_L \gg 1$, and if $f_c \approx f_a$ but $f_c > f_a$, the Eq. (2.46) becomes:

$$\eta_c = \frac{RT}{nF} \frac{i_L}{i_0} \left(\frac{\delta}{h_p}\right)^{\xi} \tag{2.48}$$

and the Eq. (2.47):

$$\eta_i = \frac{RT}{nF}\frac{i_L}{i_0} \tag{2.49}$$

meaning that in the case of ohmic-controlled reactions, dendritic growth can be expected at very low overpotentials, or better to say, if $i_0 \to \infty$, instantaneous dendritic growth is possible at all overpotentials if only mass transfer limitations are taken into consideration.

It should be noted that all the above derivations are valid, if the protrusion tip radius is sufficiently large to make the effect of the surface energy term negligible [5].

It follows from Eq. (2.49) that for systems with $i_0 \to \infty$, dendritic growth is possible at all overpotentials. Experimentally, some critical overpotential of dendritic growth initiation exists in all cases, being of the order of a few millivolts [5, 39, 40]. Assuming that under complete diffusion and surface energy control ($i_0 \to \infty$) the current density to the macroelectrode is given by [5]:

$$i = \eta\frac{(nF)^2DC_0}{\delta RT} \tag{2.50}$$

and assuming that Eq. (2.40) is valid, the current density on the tip of a dendrite growing inside the diffusion layer of a macroelectrode, i_d, is given by:

$$i_d = \eta^2\frac{(nF)^3DC_0}{8\gamma VRT}\frac{h_p}{\delta} \tag{2.51}$$

then, it is possible to derive the relationships:

$$\eta_c = \frac{8\gamma V}{nF h_p} \tag{2.52}$$

using the same procedure as in derivation of Eqs. (2.46) and (2.47), where γ is the interfacial energy between metal and solution and V is the molar volume of the metal, and minimum overpotential at which dendritic growth is still possible, η_i is given by:

$$\eta_i = \frac{8\gamma V}{nF\delta} \tag{2.53}$$

Hence, a critical overpotential for initiation dendritic growth is also expected in such cases, being of the order of few millivolts [7, 13, 38].

Model of the Cylindrical Diffusion Around the Top Edge of a Surface
Protrusion–Deposition to the Line

Unlike the conditions of spherical diffusion fulfilled around the tips of surface
protrusions, the conditions of cylindrical diffusion are fulfilled around the top edges
of the protrusions or crystals shown in Figs. 2.8b and 2.10a.

The stationary diffusion current, I, between two electrodes in a cylindrical
diffusion field (see Fig. 2.11a) is given by the Eq. (2.54) [41]:

$$I = \frac{2\pi n \, l_{\text{cyl}} \, FDC_0}{\ln \frac{R_{\text{cyl}}}{r_{\text{cyl}}}} \qquad (2.54)$$

where l_{cyl} is a length of a cylindrical electrode and n, F, D, and C_0 have their already
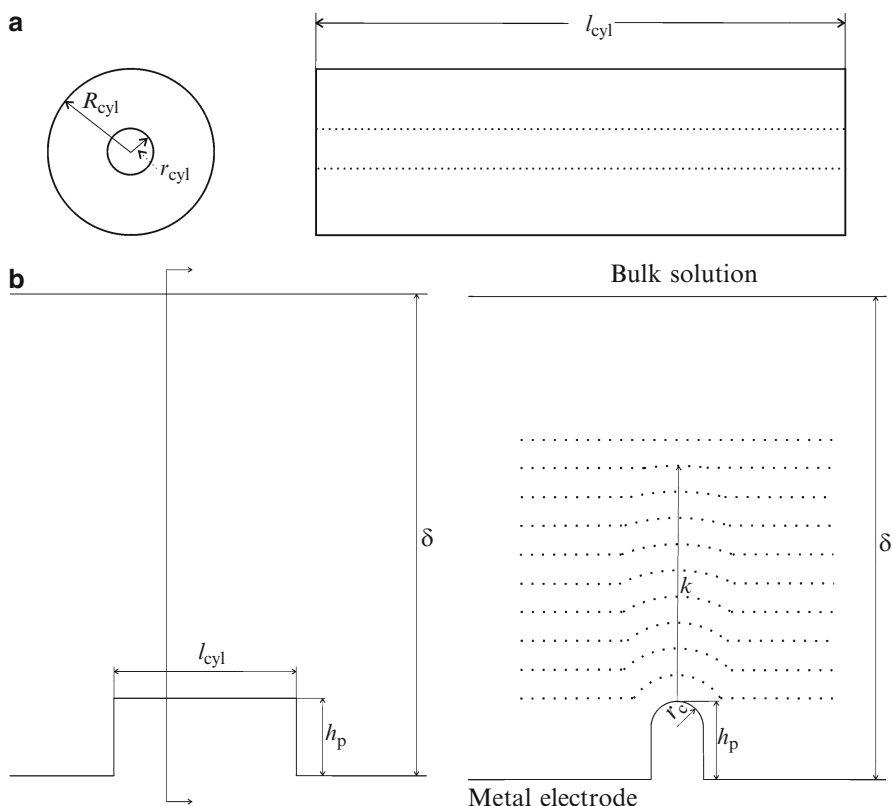mentioned meanings. For the geometry consisted of two cylindrical electrodes

Fig. 2.11 The cylindrical diffusion: (**a**) geometry of the electrode and (**b**) schematic presentation
of a protrusion growing inside the diffusion layer of the macroelectrode under the conditions for
this type of diffusion (Reprinted from Ref. [34] with permission from Elsevier)

shown in Fig. 2.11a, the current density to the electrode characterized by a radius r_{cyl} will be:

$$i = \frac{n\,FDC_0}{r_{cyl}\ln\frac{R_{cyl}}{r_{cyl}}} \tag{2.55}$$

where the concentration at the surface of an electrode characterized by a radius r_{cyl} is close to zero, while a concentration around a surface of electrode characterized by radius R_{cyl} is C_0.

The limiting diffusion current density to a cylindrical electrode, $i_{L,c}$, in the bulk solution is given by Eq. (2.56) [33, 41]:

$$i_{L,c} = \frac{n\,FDC_0}{r_{cyl}\ln\frac{r_{cyl}+d_{cyl}}{r_{cyl}}} \tag{2.56}$$

where $d_{cyl} = (\pi Dt)^{0.5}$ and t is the time.

In order to simplify, the top edges of the protrusions can be approximated by a cylindrical protrusion growing inside the diffusion layer of the macroelectrode shown in Fig. 2.11b, where r_c is the radius of the top edge of a surface protrusion, $l_{cyl} \gg r_c$, $\delta \gg h_p$ and $\delta \gg r_c$. The closest case of this approximation is crystal shown in Fig. 2.10a. Model of formation of iso-concentric lines around the top edges of growing protrusions was similar to the one proposed by Scharifker and Hills [42] for iso-concentric lines formed around the spherical nuclei. It was assumed that a cylindrical diffusion control of electrodeposition process is initiated by the last line deformed by a top edge of the growing protrusion and that the distribution of the concentration inside the diffusion layer of the macroelectrode does not vary with time. Hence, $k = m \cdot r_c$, where m is a number of deformed lines around a top edge of the protrusion. Approximately, if Eq. (2.40) is still valid, the concentration at the outer limit of the cylindrical diffusion layer inside the diffusion layer of the macroelectrode will be:

$$C^{**} = C_0\frac{h_p + mr_c}{\delta} \tag{2.57}$$

or

$$C^{**} = C_0\frac{mr_c}{\delta} \tag{2.58}$$

if the following condition is satisfied:

$$mr_c \gg h_p \tag{2.59}$$

then, Eq. (2.60) will be valid for the limiting diffusion current density under the conditions of cylindrical diffusion:

$$i_{L,c}{}^{**} = \frac{nFDC^{**}}{r_c \ln \frac{r_c + m r_c}{r_c}} \tag{2.60}$$

Using the Eq. (2.58), the Eq. (2.60) can be rewritten in the form:

$$i_{L,c}{}^{**} = \frac{nFDC_0 \frac{m r_c}{\delta}}{r_c \ln \frac{r_c + m r_c}{r_c}} \tag{2.61}$$

or

$$i_{L,c}{}^{**} = \frac{m i_L}{\ln m} \tag{2.62}$$

for $m \gg 1$.

Substitution of $i_{L,c}{}^{**}$ from Eq. (2.62) into Eq. (1.13), after rearranging, gives the Eq. (2.37) as in the case of spherical diffusion control, and the further derivation remains the same. Hence, the dendritic growth can be initiated at the same deposition overpotential under conditions of both spherical and cylindrical diffusion.

Comparison of the Rates of Growth Under Conditions of Spherical and Cylindrical Diffusion

The rate of growth of the protrusions under the conditions of spherical and cylindrical diffusion can be compared as follows. As shown earlier, the limiting diffusion current density at the tips of protrusions growing under the conditions of spherical diffusion (the needle-like dendrite or dendrite precursor), $i_{L,tip}$, inside the diffusion layer of the macroelectrode is given by:

$$i_{L,tip} = i_L \left(1 + \frac{h_p}{r}\right) \approx i_L \frac{h_p}{r} \tag{2.63}$$

where $r \ll h_p$, and the limiting diffusion current density under the conditions of cylindrical diffusion is given by Eq. (2.62).

The current density under a mixed activation–diffusion-controlled electrodeposition is given by Eq. (1.13), and substitution of the corresponding limiting diffusion current density from Eqs. (2.62) and (2.63) into the Eq. (1.13) produces after rearrangement:

$$i_{tip} = \frac{i_0 (f_c - f_a)}{1 + \frac{i_0 f_c}{i_L} \frac{r}{h_p}} \tag{2.64}$$

and

$$i_{tip,c} = \frac{i_0(f_c - f_a)}{1 + \frac{i_0 f_c}{i_L} \frac{\ln m}{m}} \qquad (2.65)$$

where i_{tip} and $i_{tip,c}$ are the current densities to the tips of dendrites growing under conditions of the spherical and cylindrical diffusion control, respectively.

The radius at the tip of protrusion growing in the conditions of spherical diffusion, r is extremely small [5], and, hence, the following is valid:

$$\frac{r}{h_p} < \frac{\ln m}{m} \qquad (2.66)$$

Thus,

$$i_{tip} > i_{tip,c} \qquad (2.67)$$

or

$$\frac{i_0(f_c - f_a)}{1 + \frac{i_0 f_c}{i_L} \frac{r}{h_p}} > \frac{i_0(f_c - f_a)}{1 + \frac{i_0 f_c}{i_L} \frac{\ln m}{m}} \qquad (2.68)$$

Hence, during electrodeposition at a selected overpotential belonging to diffusion control, faster growth occurs under the conditions of spherical control of the electrodeposition than under those of cylindrical control.

2.1.3.4 Physical Model of Dendritic Growth

The cross sections of the copper deposits obtained in a model system described earlier (Fig. 2.3a) are shown in Fig. 2.12.

Deposits obtained at 300 mV are compact, while those obtained at 600 mV are dendritic ones. Since both overpotentials correspond to the plateau of the limiting diffusion current density [14], it is clear that dendrites are formed at overpotentials larger than certain critical value, as required by the Eq. (2.47). It is seen that the current density to the tips of dendrites depends on the h_p/δ ratio (see the Eq. (2.43)), so that larger dendrites are produced at more elevated points of the electrode surface. This is because the effective height of the dendrite precursor in the modeled diffusion layer is equal to the sum of the height of the precursor and the height of the point at which nucleation took places relative to the flat part of the electrode surface. In the same way, for nuclei formed on the tip of a protrusion (Fig. 2.12b), η_c (see Eq. (2.46)) is lower than that formed on the flat surface, and a dendrite is formed at the tip of the protrusion while dendrites are not formed on the flat part of the electrode at the same overpotential.
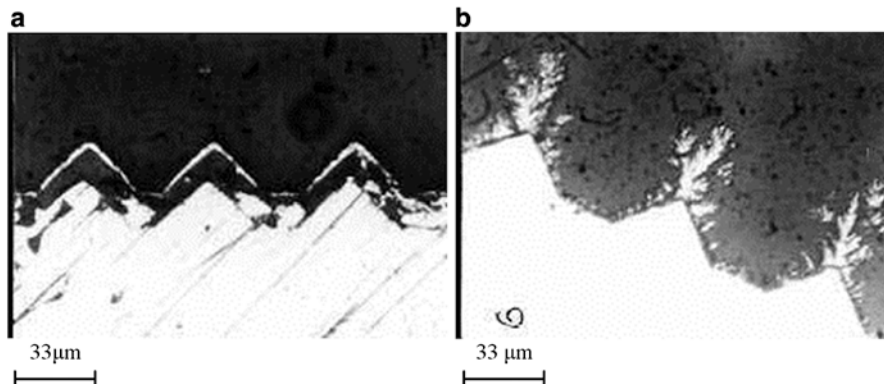
Fig. 2.12 Cross sections of copper deposits obtained in the same manner as those in Fig. 2.3b from 0.10 M CuSO$_4$ in 0.50 M Na$_2$SO$_4$. The thickness of the agar–agar diffusion layer was 1.0 mm. Deposition time: 30 min; deposition overpotential: (**a**) 300 mV and (**b**) 600 mV (Reprinted from Refs. [7, 13] with kind permission from Springer)

2.1.3.5 Dendritic Growth Inside Diffusion Layer of the Active Macroelectrode and Ohmic Diffusion and Activation–Diffusion-Controlled Deposition and Determination of η_i and η_c

In these cases, the dendritic growth starts at overpotentials larger than the one which corresponds to the beginning of the limiting diffusion current density plateau [7, 13].

There is an induction period before the initiation of dendritic growth [5]. During this induction period, dendrite precursors are formed and become sufficiently high to satisfy the Eq. (2.46) at a given overpotential, as illustrated in Fig. 2.13. The cross-like grains seen in Fig. 2.13a, b further develop into dendrite precursors (Fig. 2.13a, c).

The propagation of this structure by branching (Fig. 2.13d) produces dendrites as shown in Fig. 2.13e.

The initiation of dendritic growth is followed by a change in the slope of the current density–time curves [7, 11, 13], indicating a change in the growth mechanism of the deposit.

The slopes of these dependencies are similar to each other and independent of the deposition overpotential during the non-dendritic amplification of the surface coarsening according to the Eq. (2.34).

The change of the slope of the current-time dependencies due to the dendritic growth initiation will be treated here in somewhat simplified way.

The limiting diffusion current density to the elevated points of a surface protrusion, $i_{L,e}$, is given by:

$$i_{L,e} = \frac{nFDC_0}{\delta - h_e} \tag{2.69}$$

where h_e is the height of the elevated point relative to the flat surface.
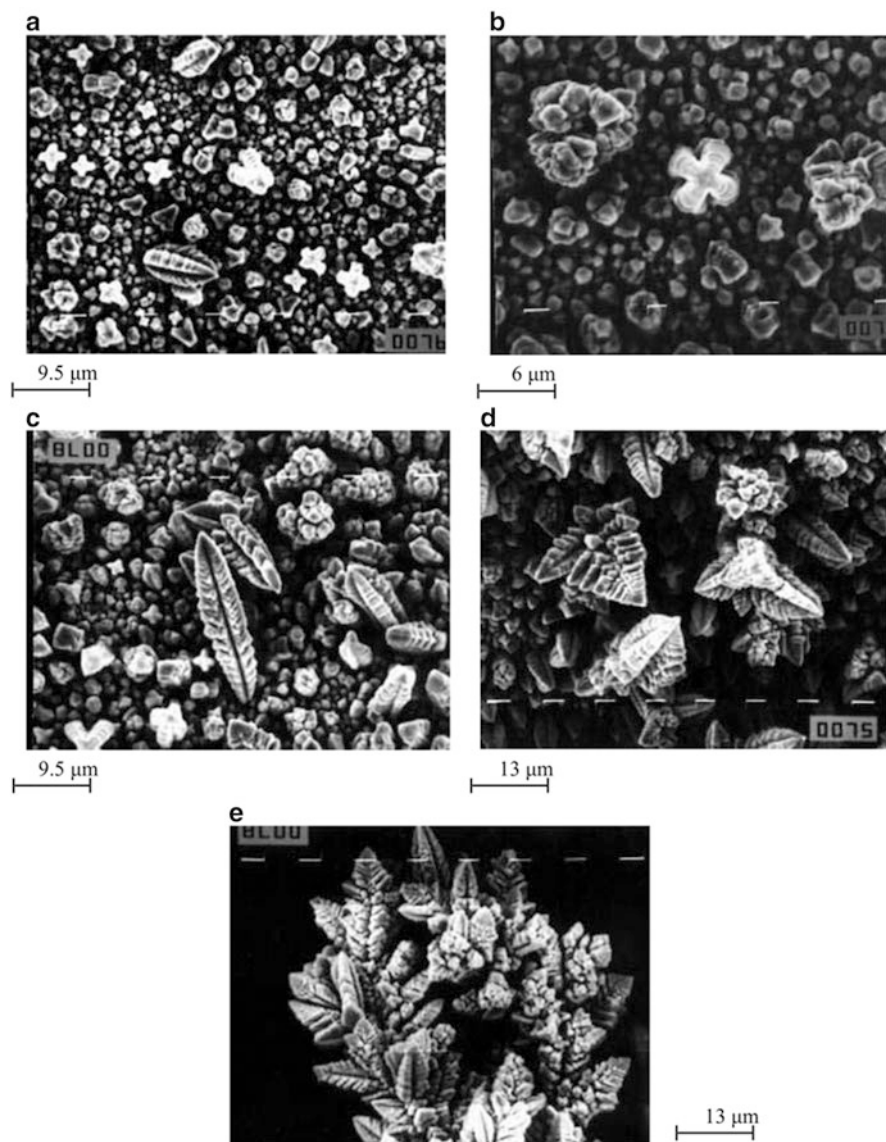
Fig. 2.13 SEM micrographs of copper deposits obtained by electrodeposition from 0.30 M CuSO$_4$ in 0.50 M H$_2$SO$_4$ onto a copper wire electrode. Deposition overpotential: 550 mV. Quantity of electricity: (**a**) 2 mA h cm^{-2}, (**b**) 2 mA h cm^{-2}, (**c**) 5 mA h cm^{-2}, (**d**) 10 mA h cm^{-2}, and (**e**) 10 mA h cm^{-2} (Reprinted from Ref. [19] with permission from the Serbian Chemical Society and Refs. [7, 8, 13] with kind permission from Springer)

Then, the limiting diffusion current density will be given by:

$$i_{\mathrm{L}} = \theta \frac{nFDC_0}{\delta} + \frac{1-\theta}{\mathrm{N}} \sum_{i=1}^{i=N} \frac{nFDC_0}{\delta - h_{i,\mathrm{e}}} \tag{2.70}$$

where θ is the part of the electrode surface uncovered by dendrites, and N is the number of elevated points on the electrode surface, and $h_{i,\mathrm{e}}$ changes with time according to Eq. (2.71):

$$h_{i,\mathrm{e}} = h_{i,0,\mathrm{e}} \exp\left(\frac{VDC_0}{\delta^2}t\right) \tag{2.71}$$

which is somewhat modified the Eq. (2.34) for $i = i_{\mathrm{L}}$.

It is obvious that $\frac{di_{\mathrm{L}}}{dt}$ does not depend on overpotential. After initiation of dendritic growth, the slopes become dependent on the overpotential. The overpotential η and current density i_{tip} on the tip of a dendrite are related by:

$$i_{\mathrm{tip}} = i_0 \frac{h_{\mathrm{p}}}{\delta} f_{\mathrm{c}} \tag{2.72}$$

for $f_{\mathrm{c}} \gg f_{\mathrm{a}}$ and the Eq. (2.70) can be rewritten in the form:

$$i = i_{\mathrm{L}}\theta + (1-\theta)i_0 \frac{f_{\mathrm{c}}}{\mathrm{N}} \sum_{i=1}^{i=N} \frac{h_{\mathrm{p,i}}}{\delta} \tag{2.73}$$

and $\frac{di}{dt}$ in this case depends on overpotential.

Hence, the maximum overpotential at which the slope of the apparent current density–time dependence remains constant and equal to that in non-dendritic amplification of the surface roughness corresponds to η_{i}. The minimum overpotential at which this slope cannot be recorded corresponds to η_{c}.

In this way, η_{i} and η_{c} can be estimated. It is known that the *i-t* dependence is different from case to case owing to different mechanisms of dendritic growth initiation and dendritic growth [13]. As a result of this, the analytical approach to the determination of η_{i} and η_{c} must be specific for each system under consideration; the procedure for one particular case is as follows.

Typical log (current)–time dependencies obtained for Cu electrodeposition from 0.20 M $CuSO_4$ in 0.50 M H_2SO_4 at overpotentials belonging to the limiting diffusion current plateau are shown in Fig. 2.14a. According to the above discussion, it is clear that the intersection points of the two linear dependencies determine the induction time of dendritic growth initiation [38].

The induction times for dendritic growth initiation extracted from the graphs in Fig. 2.14a can be presented as a function of overpotential, and the critical overpotential for instantaneous dendritic growth can be obtained by extrapolation to zero induction time [43].
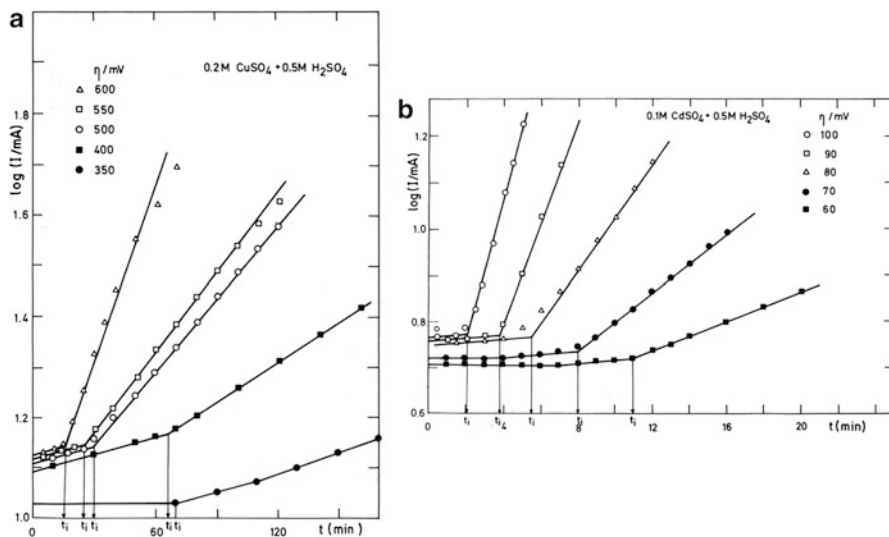
Fig. 2.14 log I as a function of time for (**a**) copper and (**b**) cadmium deposition (Reprinted from Refs. [13, 38, 43] with kind permission from Springer)

The critical overpotential of dendritic growth initiation can be determined by plotting the logarithm of the slopes of the straight lines from Fig. 2.14a as a function of overpotential, and the intersection point of the two straight lines determines η_i. The same procedure was followed for the deposition of cadmium from 0.10 M CdSO$_4$ in 0.50 M H$_2$SO$_4$ (Fig. 2.14b) [43].

The η_i and η_c of 260 and 660 mV for copper deposition (lower i_0 value) and 27 and 110 mV for cadmium deposition (larger i_0 value) are successfully determined using the above given procedure, being in perfect agreement with experimental findings as can be seen from Fig. 2.15 [13, 38, 43].

The cross sections of the copper and cadmium deposits obtained at $\eta < \eta_i$, $\eta_i < \eta < \eta_c$, and $\eta > \eta_c$ are shown in Fig. 2.15a, b, respectively. It can be seen that there is no dendrite formation when $\eta < \eta_i$, both compact and dendritic deposits are formed when $\eta_i < \eta < \eta_c$ and only dendritic metal is deposited when $\eta > \eta_c$. This is in perfect agreement with findings of Calusaru [44] for the morphology of deposits of the same metals deposited at overpotentials corresponding to full diffusion control.

The shapes of the polarization curves presented in Fig. 2.15a, b are in accordance with values of the exchange current density to the limiting diffusion current density ratios.

It is known [45] that, apart from decreasing the concentration of the depositing ion, the formation of a dendritic deposit can also be enhanced by increasing the concentration of the supporting electrolyte, increasing the viscosity of the solution, decreasing the temperature, and decreasing the velocity of motion of
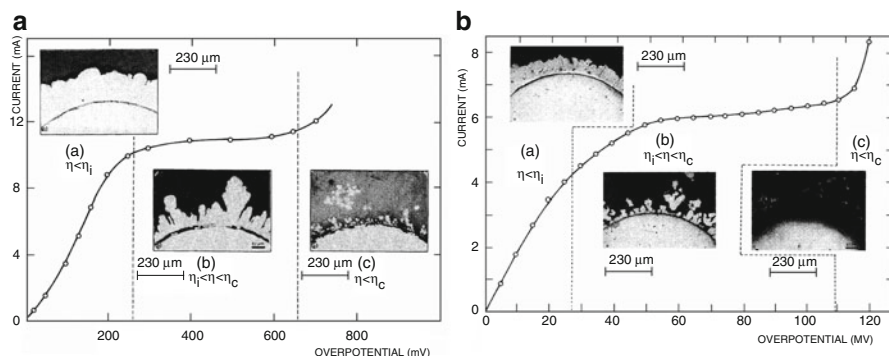
Fig. 2.15 Polarization curves for the potentiostatic deposition of (**a**) copper from 0.20 M CuSO$_4$ in 0.50 M H$_2$SO$_4$ and the cross sections of Cu deposits obtained on Cu wire electrodes previously plated with Ni: (*a*) overpotential: 200 mV, deposition time: 6 h; (*b*) overpotential: 300 mV, deposition time: 5 h, and (*c*) overpotential: 700 mV, deposition time: 2 min, and (**b**) cadmium from 0.10 M CdSO$_4$ in 0.50 M H$_2$SO$_4$ and the cross sections of Cd deposits obtained on Cu wire electrode: (*a*) overpotential: 20 mV, deposition time: 8 h; (*b*) overpotential: 40 mV, deposition time: 2 h, and (*c*) overpotential: 120 mV, deposition time: 9 min (Reprinted from Refs. [13, 38, 43] with kind permission from Springer)

the solution. Practically, all the above facts can be explained by the Eqs. (2.47) and (2.49), assuming that a decrease in η_i means enhanced dendrite formation because of the lower electrical work required to produce the dendrites. The possibility of obtaining dendrites of Pb [39] and Sn [40] from aqueous solutions at lower overpotentials than required for the formation of dendrites of Ag from aqueous solutions can also be explained by Eq. (2.53) owing to the much lower melting points of these metals, *i.e.*, their lower surface energy at room temperature. Dendrites of silver can be obtained from molten salts at overpotentials of a few millivolts [5], as in the case of Pb and Sn deposition from aqueous solutions [39, 40], because the difference between the melting point of silver and the working temperature for deposition from molten salts is not very different from the difference between the melting point of lead or tin and room temperature. On the other hand, dendrites grow from screw dislocation and nuclei of higher indices or twinned ones only [7, 11, 13]. The probability of formation of such nuclei increases with increasing overpotential [21, 46] and η_i, can also be defined as the overpotential at which they are formed. Regardless of this, Eqs. (2.47), (2.49), and (2.53) illustrate well the effect of different parameters on the initiation of dendritic growth. It is obvious that the electrochemical conditions, as well as the crystallographic ones, under which dendritic deposits are formed can be precisely determined.

2.2   Electrodeposition on the Inert Substrate

### 2.2.1   Cementation and Prevention of it by Deposition from the Complex Salt Solutions

If zinc is immersed in a copper sulfate solution, the reaction

$$Cu^{2+} + Zn \rightarrow Zn^{2+} + Cu \tag{2.74}$$
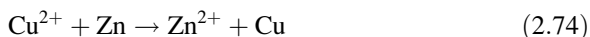
occurs, whereby copper ions are converted to the metal, while the zinc dissolves. Such deposits are spongy and dendritic in a number of cases, and non-adherent as well. Hence, a good copper deposit on a zinc substrate cannot be formed in this manner. The basic characteristics of plating baths which produce good deposits are use of inert substrates and simple or complex salt solutions from which the metal is deposited at a sufficiently negative cathode potential [13].

In a cyanide-containing bath, the copper potential is sufficiently negative so cementation does not occur and copper can be successfully deposited onto zinc. This is due to the fact that the cyanide complexes of copper are very strong so the potential of copper in such a solution is much more negative than in simple salt solutions. On the other hand, the zinc cyanide complex is relatively weak and the potentials of two metals become comparable so an external power supply is required to deposit copper on the zinc from cyanide.

Analogously, from a copper sulfate solution, cementation of copper on immersed iron occurs according to the reaction

$$Cu^{2+} + Fe \rightarrow Fe^{2+} + Cu \tag{2.75}$$
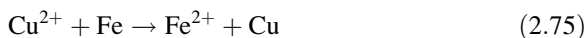
but from a cyanide solution, copper can be successfully deposited using an external power supply. In this case the complexes of both copper and iron are very strong and cementation is theoretically possible if only the reversible potentials only are taken into consideration. The fact that copper can be successfully deposited onto steal from cyanide-containing solutions is explained by the fact that the reaction between iron and cyanide ions is very slow, and so the reversible potential is never reached.

2.2.2   Surface Film Formation

2.2.2.1   Crystallization Overpotential

The formation of the first crystals during galvanostatic metal electrodeposition on an inert substrate is sometimes accompanied by a pronounced increase in overpotential [47, 48]. The dependence of the overpotential on time in such situations is shown in Fig. 2.16.
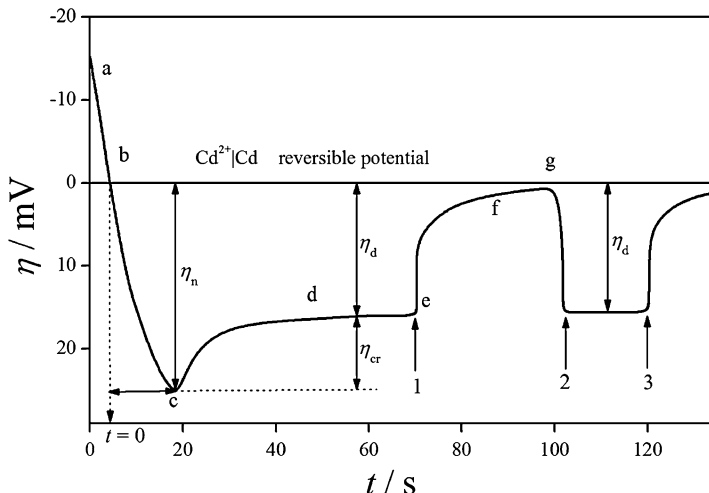
Fig. 2.16 The dependence of the overpotential on time during cadmium electrodeposition on a spiral platinum cathode (electrode surface area: 1.5 cm^2) from 0.50 M CdSO$_4$. The deposition current was 65 μA, η_n is the nucleation, η_{cr} is the crystallization, and η_d is the deposition overpotential (Reprinted from Ref. [47] with permission from Bulgarian Chemical Communications and Ref. [13] with kind permission from Springer)

The overpotential η_t changes with deposition time from point b to point c according to the Eq. (2.76) [47]:

$$\eta_t = \frac{RT}{nF} \ln \frac{C_{t,a}}{C_{0,a}} \tag{2.76}$$

where $C_{t,a}$ is the concentration of adatoms at time t and $C_{0,a}$ is the concentration of adatoms at $t = 0$.

On the other hand, the surface concentration of adatoms changes according to:

$$C_{t,a} = C_{0,a} + \frac{it}{nF} \tag{2.77}$$

Substitution of the Eq. (2.77) into the Eq. (2.76) produces

$$\eta_t = \frac{RT}{nF} \ln \left(1 + \frac{it}{nFC_{0,a}} \right) \tag{2.78}$$

which becomes

$$\eta_n = \frac{RT}{nF} \ln \left(\frac{C_{cr,a}}{C_{0,a}} \right) \tag{2.79}$$

at the moment of nucleation.

The Eq. (2.78) describes the dependence of the overpotential on the deposition time from point b to point c. The overpotential changes due to the change of the surface concentration of adatoms from $C_{0,a}$ at the equilibrium potential to some critical value $C_{cr,a}$ at the critical overpotential, η_n, at which the new phase is formed. Hence, the concentration of adatoms increases above the equilibrium concentration during the cathode reaction, meaning that at potentials from point b to point c there is some supersaturation. The concentration of adatoms increases to the extent to which the boundary of the equilibrium existence of adatoms and crystals has been assumed to enable the formation of crystal nuclei. On the other hand, the polarization curve can be expressed by the equation of the charge transfer reaction, modified in relation to the crystallization process, if diffusion and the reaction overpotential are negligible, as given by Klapka [48]:

$$i = i_0 \left\{ \frac{C_a}{C_{0,a}} \exp\left(\frac{\alpha n F \eta}{RT}\right) - \exp\left[\frac{(\alpha - 1) n F \eta}{RT}\right] \right\} \tag{2.80}$$

because the partial anode current density depends on the concentration of adatoms, which for $i/i_0 = 0$ becomes equal to the Eq. (2.79).

Obviously, the Eq. (2.80) becomes valid at the moment of the formation of the new phase, and it can be used for estimating the overpotential, η_n, at which the nucleation takes place. In order to calculate this overpotential, the supersaturation must be known. According to Pangarov et al. [22, 49, 50], the work of formation of differently oriented particles can be estimated using supersaturations of four to seven. Considering the nucleation overpotential (for different supersaturations), Klapka [48] assumed ten as the upper limit of supersaturation. The lower limit is obviously one and the Eq. (2.80) in this case becomes identical to the equation of the charge transfer reaction.

The difference in overpotential between the curves for a given supersaturation (nucleation on an inert substrate) and the curve for a supersaturation equal to unity (deposition on a native substrate) gives the value of the crystallization overpotential, η_{cr} [48]. It is equal to the difference in the overpotential at point c and at point e in Fig. 2.16. If the current is switched off at point e, the electrode potential will approach to the reversible potential of the deposited metal (point g); after switching on the current again at point g, the overpotential returns to the same value as at point e, i.e., the deposition overpotential, η_d, meaning that a new phase is formed. On the contrary, if current is switched off before point c, the electrode potential will approach the initial stationary potential of the inert electrode, meaning that new phase has not been formed [47].

Using temperature of 25 °C, $\alpha = 0.5$, $n = 1$ or 2, and the Eq. (2.80), Klapka [48] calculated the dependencies of the nucleation overpotential on the i/i_0 ratio for $C_{cr,a}/C_{0,a} = 1$, 2, 5, and 10. The calculated curves are shown in Fig. 2.17a. From these curves, the dependencies of the crystallization overpotentials on the i/i_0 ratio, shown in Fig. 2.17b, can be derived.
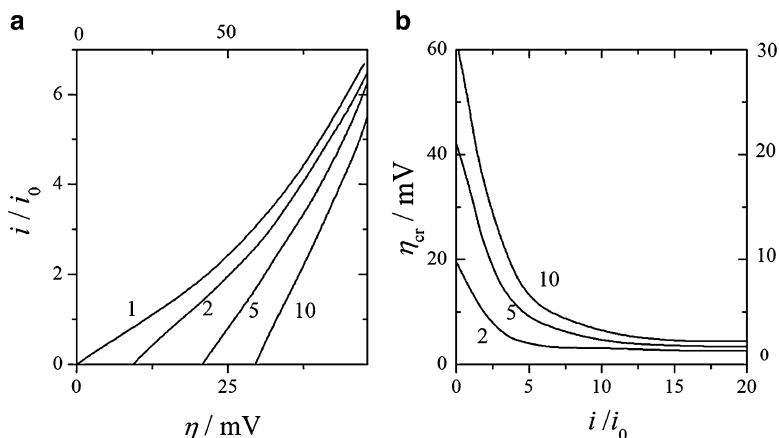
Fig. 2.17 (**a**) Dependence of the i/i_0 ratio on the overall overpotential for different $C_{cr,a}/C_{0,a}$ ratios, indicated on the curves (*upper scale for n = 1, lower scale for n = 2*) and (**b**) dependence of the crystallization overpotential, η_{cr} (in mV), for the cathodic reaction on i/i_0 for different $C_{cr,a}/C_{0,a}$ ratios, indicated on the curves (*left-hand scale for n = 1, right-hand scale for n = 2*) (Reprinted from Ref. [48] with permission from the Collection of Czechoslovak Chemical Communications and Ref. [13] with kind permission from Springer)

The crystallization overpotential strongly decreases with increasing i/i_0 ratio. As a result of this, it can be measured only in the case of a metal deposition which is characterized by very high values of the exchange current density [48].

2.2.2.2   The Nucleation Exclusion Zones

Metal electrodeposition on inert electrodes begins with the formation of separate growth centers until a continuous or disperse deposit is produced. Once a nucleus of the depositing metal has been formed, the current flowing causes a local deformation of the electric field in the vicinity of the growing center. As a result, an ohmic potential drop occurs along the nucleus–anode direction. Considering the high dependence of the nucleation rate on the overpotential, new nuclei would be expected to form only outside the spatial region around the initial nucleus. In that region, the potential difference between the cathode and the electrolyte surpasses some critical value η_{crit}. Using simple mathematics, one obtains for the radius of the screening zone, r_{sz}, in an ohmic-controlled deposition:

$$r_{sz} = f \frac{U_\Omega}{U_\Omega - \eta_{crit}} r_N \tag{2.81}$$

where η_{crit} is the critical overpotential for nucleation to occur, U_Ω is the ohmic drop between the anode and cathode, f is a numerical factor, and r_N is the radius of the nucleus. The radius of the screening zone depends on the value of both U_Ω and η_{crit}.
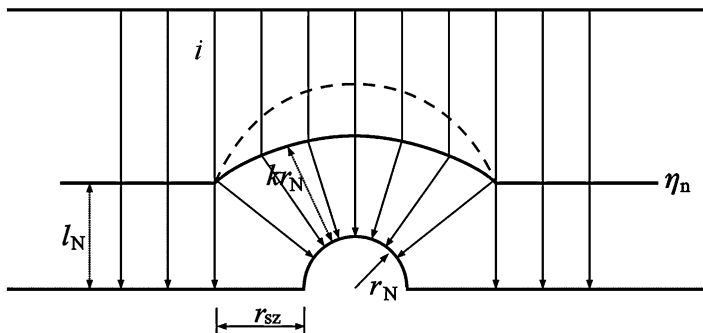
Fig. 2.18 A schematic representation of the deformation of the current field around a defect or a grain grown on a foreign substrate. For an explanation of the symbols, see Ref. [52] (Reprinted from Ref. [52] with permission from the Serbian Chemical Society and Ref. [13] with kind permission from Springer)

At a constant η_{crit}, an increase in U_Ω leads to a decrease in the radius of the screening zone, the same is true if η_{crit} decreases at constant U_Ω [51].

The radius of a nucleation exclusion zone can be calculated on the basis of the following discussion, taking into account the charge transfer overpotential also. If there is a half-spherical nucleus on a flat electrode, the extent of the deviation in the shape of the equipotential surfaces which occurs around it depends on the crystallization overpotential, current density, a resistivity of the solution and on the radius of the nucleus, r_N. If the distance from the flat part of the substrate surface to the equipotential surface which corresponds to the critical nucleation overpotential, η_n, is l_N, then this changes around defect to the extent $k \cdot r_N$, where k is a number, as is presented in Fig. 2.18.

Therefore, in this region, the current lines deviate from straight lines toward the defect, thus causing an increase in the deposition rate, while in the surrounding region nucleation does not occur, *i.e.*, a nucleation exclusion zone is formed. The voltage drop between the point from which the deviation occurs and the nucleus surface consists of the ohmic drop between these points and the charge transfer overpotential at the nucleus solution interface. The nucleation overpotential includes both the crystallization and charge transfer (deposition) overpotential:

$$\eta_n = \eta_{cr} + \eta_d \tag{2.82}$$

Hence, at the moment when $k \cdot r_N$ become equal to l_N

$$k \, r_N i\rho = \eta_{cr} \tag{2.83}$$

where i is the current density along the current lines and ρ is the specific ohmic resistivity of the solution. Hence, when the ohmic drop between the deviation point and nucleus surface becomes equal to the crystallization overpotential, a new nucleation becomes possible on inert substrate assuming in both cases the same

charge transfer overpotential, and the same value of the current density between the two symmetrical points on the anode and inert cathode surface and between the same point on the anode and the point at the surface of the earlier formed nucleus.

The radius of the nucleation exclusion zone, r_{sz}, corresponds to the distance between the edge of a nucleus and the first current line which not deviates (when $k \cdot r_N$ becomes equal to l_N). Accordingly, nucleation will occur at distances from the edge of a nucleus equal or larger than r_{sz}, which can be calculated as:

$$r_{sz} = r_N \left(\sqrt{2k + 1} - 1 \right) \tag{2.84}$$

If the Eq. (2.83) is taken into account, one obtains:

$$r_{sz} = r_N \left(\sqrt{\frac{2\eta_{cr}}{r_N \rho i} + 1} - 1 \right) \tag{2.85}$$

According to the Eq. (2.85), a new nucleation is possible in the vicinity of a nucleus if $\eta_{cr} \to 0$ or $i \to \infty$ or $\rho \to \infty$

The analysis of the nucleation rate around a growing grain can also be treated in a more rigorous way [53]. Regardless of this, the above model is sufficient to explain the role of nucleation–exclusion zones in the first stage of electrocrystallization. This is because the nuclei formed are extremely small, and the spherical diffusion control around them can be established after relatively large induction times [54]. During this induction time, the nucleation exclusion zones are due to the ohmic drop in the vicinity of a growing center. Simultaneously, the nucleation process is practically terminated, because it is very fast [55]. On the other hand, the rigorous treatment of this problem is very complicated while the effect of the kinetic parameters of the deposition process in the first stage of electrocrystallization can be qualitatively explained in a simple way using the described model, *i.e.,* Klapka's concept of crystallization overpotential and the classical nucleation theory.

During the cathodic process at low i/i_0, the crystallization overpotential is considerably high; with increasing i/i_0, however, it decreases rapidly [48]. Hence, for $i_0 \to 0$, it follows that $r_{sz} \to 0$.

2.2.2.3 Nucleation Rate and Deposition Overpotential

It has been established experimentally that the number of nuclei deposited electrolytically onto an inert electrode increases linearly with time after an induction period. After a sufficient length of time, it reaches a saturated value that is independent of time. The density of the saturation value increases with the increasing applied overpotential and is strongly dependent on the concentration of the electrolyte and the state of the electrode surface [55].

Kaischew and Mutaftchiew [56] explained the phenomenon of saturation on the basis of energetic inhomogeneity of the substrate surface. They assumed that the active centers have different activity, or different critical overpotential with respect to the formation of nuclei. Nuclei can be formed on those centers whose critical overpotential is lower or equal to the overpotential externally applied to the electrolytic cell. The higher the applied overpotential, the greater the number of weaker active sites taking part in the nucleation process and, hence, the greater the saturation nucleus density is. The formation and growth of nuclei is necessarily followed by the formation and growth of nucleation exclusion zones. After some time, the zones overlap to cover the substrate surface exposed for nucleation, thus terminating the nucleation process [55]. This is well illustrated in Fig. 2.19. It can be seen that the deposit obtained at low current densities consists of a small number of nuclei, but with increasing overpotential or current density, the number of growth sites increases and the grain size of the deposit decreases.

The simultaneous action of both active centers and nucleation exclusion zones must be taken into consideration when discussing the dependence of the number of nuclei on time. In the limiting case for active centers, when screening zones are not formed, the saturation nucleus density is exactly equal to the integral number of active centers. In the limiting case for nucleation exclusion zones, the saturation nucleus density is directly proportional to the nucleation rate and inversely to the zone growth rate [55]. It is obvious that the saturation nucleus density is larger in the first than in the second case, because of the deactivation of active centers by overlapping nucleation exclusion zones.

The classical expression for the steady-state nucleation rate, J, is given by [47, 57, 58]:

$$J = K_1 \exp\left(-\frac{K_2}{\eta^2}\right) \tag{2.86}$$

where K_1 and K_2 are practically overpotential-independent constants. Equation (2.86) is valid for a number of systems regardless of the value of the exchange current density for the deposition process [47, 58]. At one and the same deposition current density, i, decreasing i_0 leads to an increasing nucleation rate and decreasing nucleation exclusion zones radii. Hence, the limiting case for nucleation exclusion zones can be expected when $i/i_0 \to 0$, and the limiting case for active centers when $i/i_0 \to \infty$.

The saturation nucleus density and the exchange current density of the deposition process strongly affect the morphology of metal deposits. At high exchange current densities, the radii of the screening zones are large and the saturation nucleus density is low. This permits the formation of large, well-defined crystal grains and granular growth of the deposit. At low exchange current densities, the screening zones radii are low, or equal to zero, the nucleation rate is large, and a thin surface film can be easily formed. The saturation nucleus density depends also on the deposition overpotential.
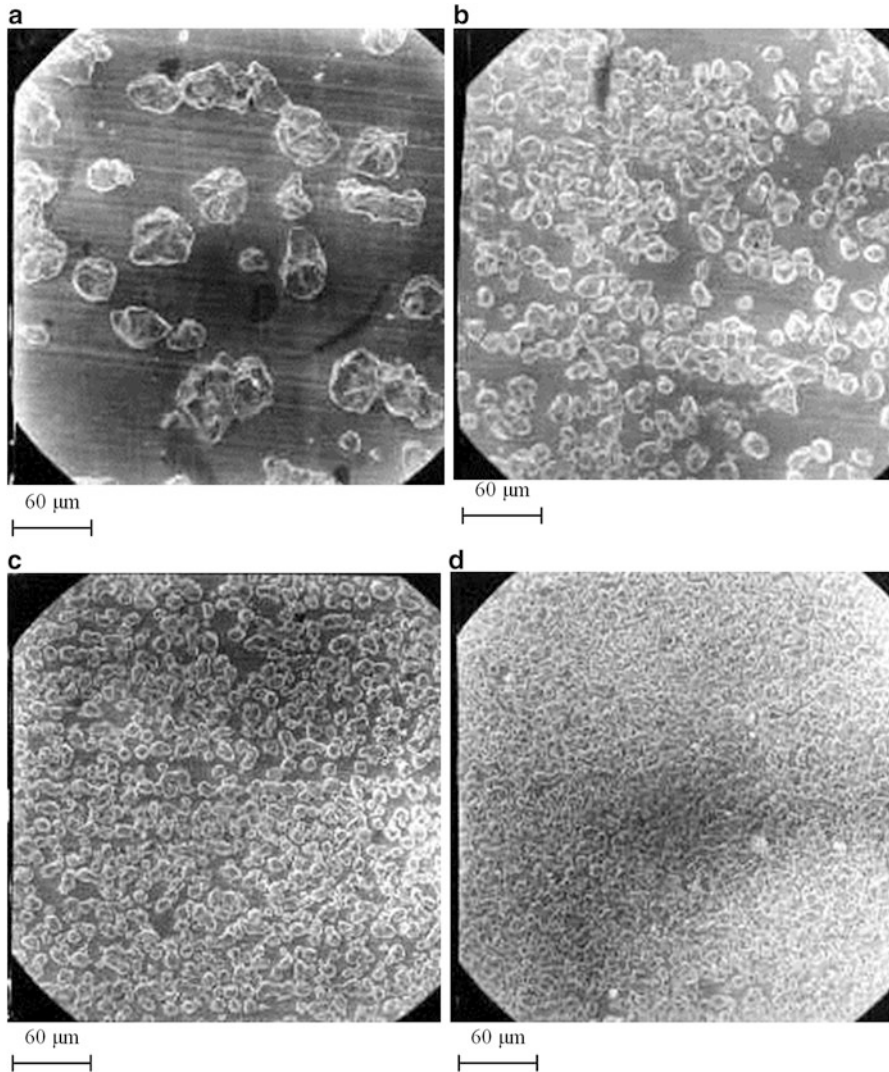
Fig. 2.19 Cadmium deposits obtained from 1.0 M CdSO$_4$ in 0.50 M H$_2$SO$_4$ solution onto a copper plane electrode: (**a**) deposition overpotential: 10 mV; deposition time: 24 min, (**b**) deposition overpotential: 40 mV; deposition time: 4 min, (**c**) deposition overpotential: 60 mV; deposition time: 2 min, and (**d**) deposition overpotential: 110 mV; deposition time: 80 s (Reprinted from Refs. [13, 54] with kind permission from Springer)

The nucleation law can be written as [59]:

$$N = N_0[1 - \exp(-At)] \qquad (2.87)$$

where

$$A = K_1 i_0 \exp\left(-\frac{K_2}{\eta^2}\right) \tag{2.88}$$

and N_0 is the saturation nucleus surface density (nuclei cm^{-2}), being dependent on the exchange current density of deposition process and the deposition overpotential.

The overpotential and the current density in activation-controlled deposition inside the Tafel region are related by:

$$\eta_{act} = \frac{b_c}{2.3} \ln \frac{i}{i_0} \tag{2.89}$$

Therefore, increasing b_c and decreasing i_0 leads to an increase in the deposition overpotential. According to Eq. (2.88), the value of A increases with increasing overpotential and decreases with decreasing the exchange current density. It follows from all available data that the former effect is more pronounced resulting in deposits with a finer grain size with decreasing value of the exchange current density.

Nucleation does not occur simultaneously over the entire cathode surface, but it is a process extended in time so that crystals generated earlier may be considerably larger than those generated later. This causes periodicity in the surface structure of polycrystalline electrolytic deposits, as well as coarseness of the obtained thin metal film even when they are formed on ideally smooth substrate. Hence, the larger the nucleation rate, the more homogeneous the crystal grain size distribution is obtained leading to formation of smoother deposit. Obviously, periodicity in the surface structure is a more complicated problem, as shown by Kovarskii et al. [60–62], but for the purpose of this analysis, the above conclusion is sufficient.

The confirmation of the above theories with accent on the analysis of the effect of exchange current density on the thin metal film formation on inert substrates can be obtained in the following way. In Chap. 1 (see Fig. 1.13 and Table 1.2) are given the polarization curves, the exchange current density values, and i_L/i_0 ratios for three different electrodeposition systems (Cd, Cu, and Ni) characterized by the substantially different value exchange current densities [13, 63].

The deposits of Cd, Cu, and Ni obtained by the processes of electrochemical deposition on the inert substrates are shown in Fig. 2.20. In Cd electrodeposition, boulders or large grains are formed by the independent growth of formed nuclei inside zones of zero nucleation (Fig. 2.20a). Due to the high value of i_0 for Cd, the deposition overpotential is low, the crystallization overpotential is relatively large, and the screening zones are, according to Eq. (2.81), relatively large. On the other hand, the nucleation rate is low.

In the case of Cu, due to the lower exchange current density value, a surface film is practically formed by a smaller quantity of electricity (Fig. 2.20b). The value of the deposition overpotential is larger than in the case of Cd, and the crystallization overpotential is lower, resulting in a decrease of the zero nucleation zone radiuses. In the case of Cu, it is clear that a considerably larger nucleation rate is observed.
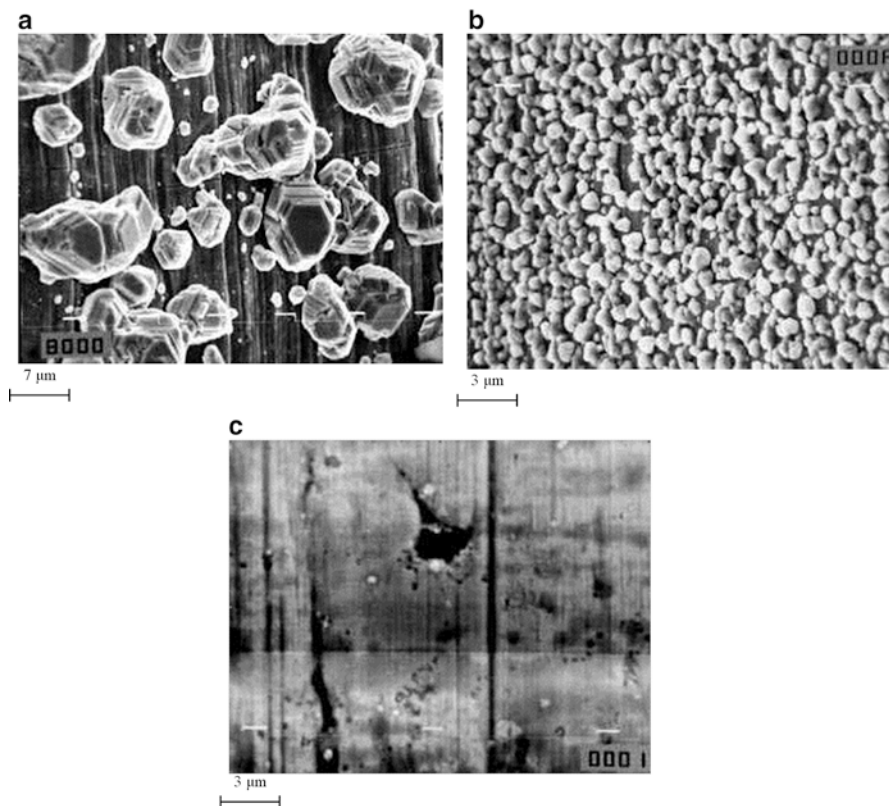
Fig. 2.20 (**a**) Cd deposit on Cu substrate obtained at a current density of 1 mA cm^{-2} from 0.070 M CdSO$_4$ in 0.50 M H$_2$SO$_4$. Deposition overpotential: 15 mV. Deposition time: 1200 s, (**b**) Cu deposit on Ag substrate obtained at a current density of 1 mA cm^{-2} from 0.070 M CuSO$_4$ in 0.50 M H$_2$SO$_4$. Deposition overpotential: 60 mV. Deposition time: 300 s, and (**c**) Ni deposit on Cu substrate obtained at a current density of 1 mA cm^{-2} from 0.070 M NiSO$_4$ in 0.50 M Na$_2$SO$_4$ + 30 g dm^{-3} H$_3$BO$_3$, pH $= 4$. Deposition overpotential: 715 mV. Deposition time: 120 s (Reprinted from Ref. [63] with permission from the Serbian Chemical Society and Refs. [8, 13] with kind permission from Springer)

A further decrease in the exchange current density value, as in the case of Ni, leads to the surface morphology shown in Fig. 2.20c. A surface film is formed, but it is porous, probably due to hydrogen evolution.

Hence, a decrease in the value of the exchange current density of the deposition process enhances thin surface metal film formation on inert substrates due to an increase in the nucleation rate and a decrease in the radius of the zero nucleation zones. As a result of this, a compact surface metal film is formed with a smaller quantity of electrodeposited metal, and its coarseness and porosity decrease with a decreasing exchange current density. On the other hand, at sufficiently negative equilibrium potentials and low hydrogen overpotential for an inert substrate,
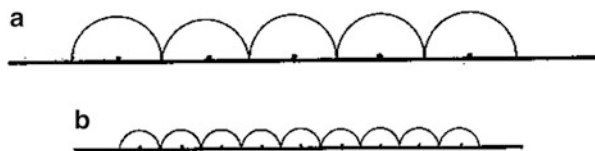
Fig. 2.21 Schematic representation of the formation of the surface film: (**a**) low nucleation rate and (**b**) high nucleation rate (Reprinted from Ref. [13] with permission from Springer)

decreasing the exchange current density of the deposition process can produce a porous deposit due to hydrogen evolution.

2.2.2.4 Compact Surface Film Formation

A surface metal film on an inert substrate is formed by the coalescence of growing grains developed from corresponding nuclei, as is illustrated in Fig. 2.21, whereby the surface properties of the inert substrate are changed to those of the electrodeposited metal.

It is obvious that the larger nucleus density, the thinner is the thickness of the metal film required to isolate the substrate from the solution. At the same time, a thinner surface film will be less coarse than a thicker one. This means that a smoother and thinner surface film will be obtained at larger deposition overpotentials and nucleation rates, *i.e.,* by electrodeposition processes characterized by high cathodic Tafel slopes and low exchange current densities.

The main ways of the decrease of the exchange current density and the increase of the cathodic Tafel slope can be considered as follows.

2.2.2.5 Deposition from Complex Salt Solutions

The silver deposits obtained from nitrate electrolyte-containing 0.10 M $AgNO_3$ in 0.20 M HNO_3 (the basic electrolyte) at the overpotential corresponding to an initial current density of $0.5i_L$ and from the ammonium complex electrolyte (0.10 M $AgNO_3$ in 0.50 M $(NH_4)_2SO_4$ solution to which ammonium hydroxide had been added to dissolve the silver sulfate precipitate) at the overpotential corresponding to an initial current density of $0.3i_L$ are presented in Fig. 2.22 [64].

From Fig. 2.22a, it can be seen that the silver deposit obtained from the nitrate electrolyte was constructed from a small number of nuclei. Irregular large grains were formed even with an initial current density of $0.5i_L$, causing formation of a non-compact deposit. On the other hand, the microcrystalline deposit was obtained by electrodeposition from the ammonium electrolyte (Fig. 2.22b).

The poor microthrowing power of the Ag deposit obtained from the nitrate electrolytes at the small current densities can be explained in the following way:
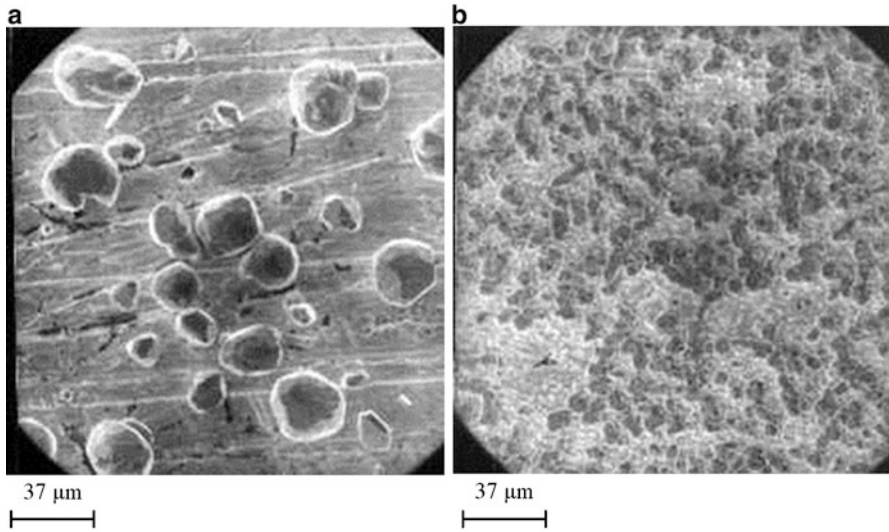
Fig. 2.22 Silver deposits obtained from: (**a**) the nitrate solution at an overpotential of 18 mV (corresponding to an initial current density of $0.5i_L$) (90 mA min cm^{-2}) and (**b**) an ammonium complex solution at an overpotential of 65 mV (corresponding to an initial current density of $0.3i_L$) (90 mA min cm^{-2}) (Reprinted from Ref. [64] with permission from Elsevier and Ref. [13] with kind permission from Springer)

For $i_0 >> i_L$, the deposition overpotential according to Eq. (1.33) is given by [13, 64]:

$$\eta = \frac{RT}{nF} \ln \left(1 - \frac{i}{i_L} \right) \tag{2.90}$$

It follows from Eqs. (2.87) and (2.88) that for $i << i_L$, $\eta \to 0$ and $N \to 0$. Thus, at low current densities, poor microthrowing power is expected.

On the other hand, for the ammonium complex solution, it is valid $i_0 << i_L$ [13]. For $i_0 << i$ and $i << i_L$, Eqs. (2.87), (2.88), and (1.29) are valid meaning that $N > 0$. Hence, for deposition at low current densities, the decreasing i_0 leads to the increasing coverage of an inert substrate for a given quantity of deposited metal.

2.2.2.6 Deposition in the Presence of Adsorbed Additives

Inorganic Compounds

The effect of addition of inorganic compounds to the electroplating baths on electrodeposition processes was illustrated by the analysis of Ag deposits obtained from the nitrate electrolytes (0.50 M AgNO$_3$ in 100 g dm^{-3} NaNO$_3$) without (Fig. 2.23a) and with the addition of 6 g dm^{-3} H$_3$PO$_4$ (Fig. 2.23b) [65–67].
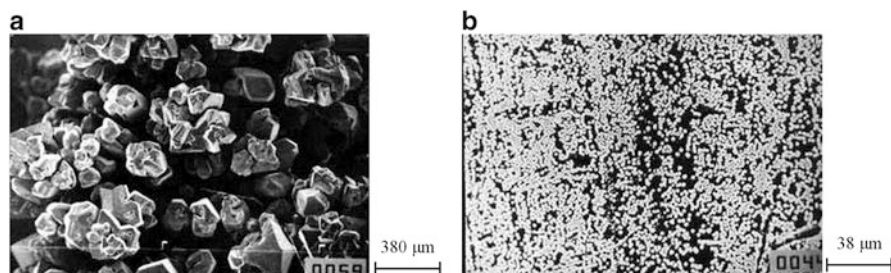
Fig. 2.23 Silver deposits electrodeposited from 0.50 M AgNO$_3$ in 100 g dm^{-3} NaNO$_3$: (**a**) in the potentiostatic regime of electrolysis onto Ag wire electrode without the addition of H$_3$PO$_4$. Quantity of electricity: 100 mA h cm^{-2}. Deposition overpotential: 120 mV. The exchange current density: 26 mA cm^{-2} and (**b**) in the galvanostatic regime of electrolysis onto Pt wire electrodes with the addition of 6 g dm^{-3} H$_3$PO$_4$. Current: 30 mA. Time: 2 s. The exchange current density: 5 mA cm^{-2} (Reprinted from Refs. [13, 65, 66] with kind permission from Springer)

In the case of electrodeposition from the solution containing PO$_4{}^{3-}$-ions, almost complete surface coverage was achieved even with a charge quantity of 2 mA h cm^{-2} at a current density of 30 mA cm^{-2} (*i.e.,* under the optimal film deposition conditions, as determined in Ref. [65]). This is probably due to the possibility of further nucleation occurring immediately next to the already existing nuclei, as a result of the smaller values of the radii of the nucleation exclusion zones caused by the decrease of the exchange current density for the deposition process by the addition of PO$_4{}^{3-}$-ions. For comparison, in phosphate-free nitrate solution, a compact Ag film had not been deposited even after 100 mA h cm^{-2} had been passed through the cell, as can be seen from Fig. 2.23a [65].

Organic Compounds

The effect of organic compounds on morphology of electrodeposited metal has been examined by the analysis of cadmium electrodeposition processes from solution containing 0.25 M CdSO$_4$ in 0.50 M H$_2$SO$_4$ to which was added 3.3 g dm^{-3} poly(oxyethylene alkylphenol) (9.5 mol ethylene oxide) [68].

The overpotential-log (current density) plot is given in Fig. 2.24. A well-defined Tafel line characterized by $i_0 \approx 10^{-6}$ A cm^{-2} and $b_c = 160$ mV dec^{-1} was observed at higher potentials also. This phenomenon is explained by the formation of a film of the organic additive which completely covers the cathode at sufficiently negative potentials [69, 70]. Tafel linearity was also observed over a short overpotential range at low overpotentials. The values of $i_0 \approx 10^{-3}$ A cm^{-2} and $b_c = 60$ mV dec^{-1} obtained in this case are close to the values expected for deposition from a pure solution [71].

It has been shown [16] that the optimum plating overpotential and current density are determined by the upper limit of the validity of the Tafel equation for
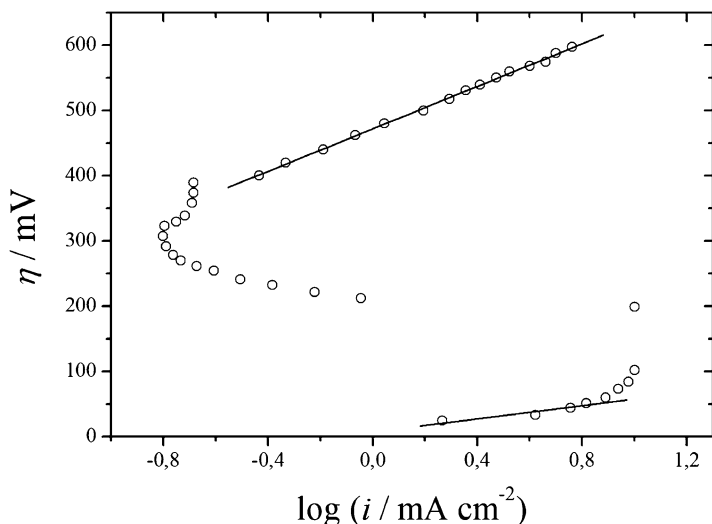
Fig. 2.24 Overpotential *vs*. log (current density) for cadmium deposition in the presence of additive (Reprinted from Ref. [68] with permission from Elsevier and Ref. [13] with kind permission from Springer)

the deposition process. In this case, as can be seen in Fig. 2.24, the optimum deposition overpotentials are about 530 mV and 40 mV in the presence and in the absence of adsorption of this additive, respectively. Cadmium deposits 3 μm thick obtained at 40 mV and 530 mV are shown in Fig. 2.25. It can be seen that the deposit obtained at 40 mV is constructed from large grains (Fig. 2.25a), whereas the one obtained at 530 mV is fine grained due to the larger overpotential (Fig. 2.25b).

Apart from the nucleation density, the preferential orientation of the nuclei is important in surface metal film formation. As the deposit becomes free of the influence of the substrate structure on thickening, instead of the formation of a randomly oriented grain structure, a preferred crystal orientation can develop, which gives a definite texture to the cross section of the deposit [72]. Texture can be expressed in terms of degree of orientation of the grains constituting the deposit.

It is to note that the theoretical approach to the problems of deposit orientation was successfully developed by Pangarov et al. [21, 49, 50]. Using this theory, it was possible to determine the preferred orientation as a function of overpotential from silver single crystals [50] to nickel and iron thin films [21, 50].

Finally, it can be concluded that increasing the overpotential at one and the same current density leads to less coarse deposits with prolonged deposition, because of lower grains formed during the formation of the surface metal film. This conclusion is valid if $i_0 < i_L$. In the opposite case, a rough deposit is often not formed because of disperse or granular deposit formation. Hence, the first condition that must be satisfied in thick non-rough metal film deposition is that the exchange current density must be considerably lower than the limiting diffusion current density in the system under consideration. The second condition is that the deposition current
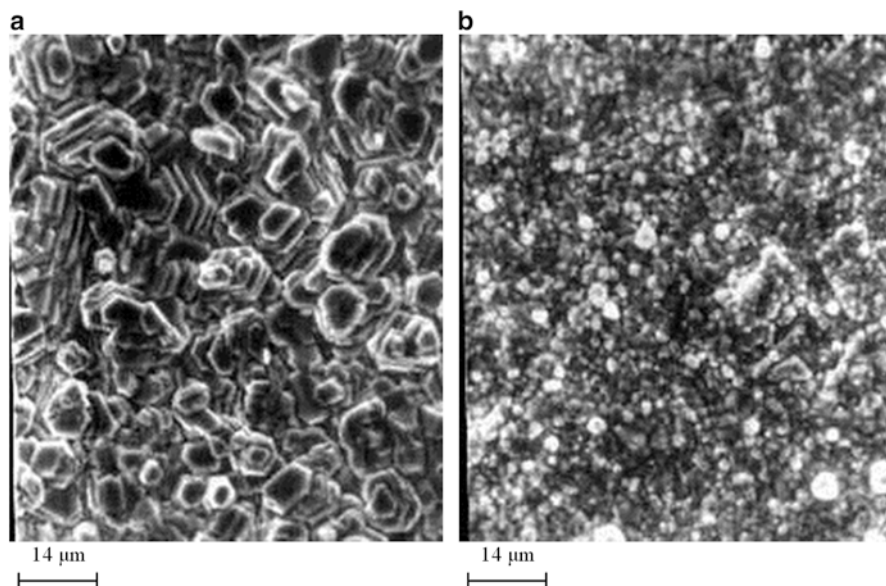
Fig. 2.25 Cadmium deposits formed in the middle of Cu electrodes at overpotentials of (**a**) 40 mV; in the absence of adsorption of the additive and (**b**) 530 mV; in the presence of adsorption of the additive. The deposit thickness is 3 μm (Reprinted from Ref. [68] with permission from Elsevier and Ref. [13] with kind permission from Springer)

density must be a little larger than the one corresponding to the end of the Tafel linearity. In this way, the formation of large and well-defined crystal grains due to deposition under activation control will be prevented. Simultaneously, the increase of the surface coarseness due to the deposition in mixed activation–diffusion control will be minimum, and the formation of cauliflower-like and carrot-like protrusions will be avoided.

On the other hand, smooth and bright deposits can be only obtained in the presence of specific substances denoted as additives. They are the most often organic compounds that either are incorporated into the deposits or undergo electrochemical reaction. Also, they can be adsorbed on the flat part of the surfaces permitting the electrodeposition at the steps [73, 74].

2.2.2.7 Smooth Surfaces

Basic Facts

It is well known [11] that in electrolytes containing specific substances as additives, a phenomenon opposite to the ones described so far can occur, *i.e.*, a more rapid metal deposition at recessed points of the surface than at elevated points. This causes leveling of the surface irregularities as is illustrated in Fig. 2.26.

Fig. 2.26 Illustration of leveling action of an additive during metal electrodeposition
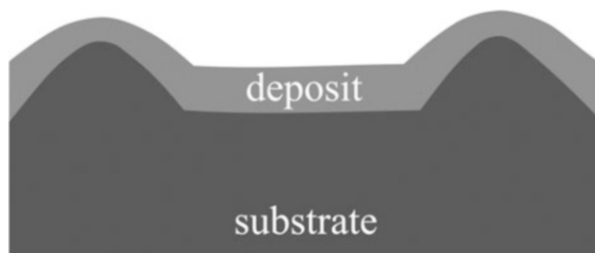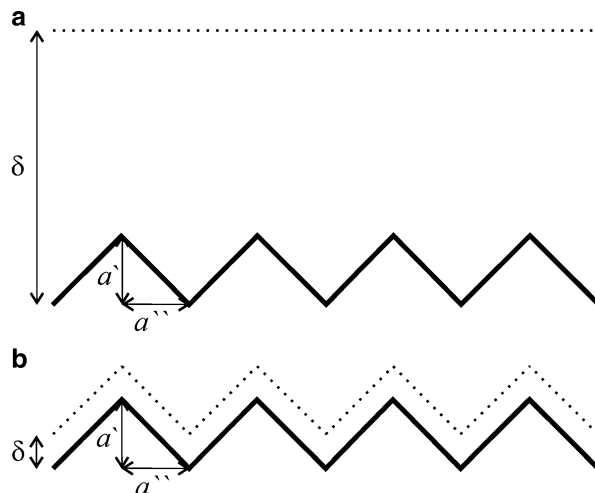

Fig. 2.27 Serrated surface profile with diffusion layer, showing the difference between (**a**) microprofile ($a' << \delta$) and (**b**) macroprofile ($a' >> \delta$) (Reprinted from Refs. [13, 76] with kind permission from Springer)

The fact that this phenomenon is only observed at microprofiles not exceeding 100 µm in amplitude necessitated the introduction of the concept of "microthrowing power" as a category different from ordinary throwing power [11]. The latter is used in technical literature to describe the quality of electrolytes in plating on macroprofiles, at which a similar effect is never observed. The difference between a microprofile and a macroprofile can be seen from Fig. 2.27.

Detailed surveys of the literature on leveling are available in Refs [11, 73–75, 77, 78].

Model of Leveling

All the experimental evidence points to the conclusion that leveling takes place under conditions when the supply of the substance causing inhibition of the electrode process is under diffusion control. It was already clear to early investigators that the explanation should be sought in the local variations in the supply of the leveling agent over the surface profile. Peaks at the surface receive larger amounts of an additive than the recesses. This results in an increase in inhibition

and a decrease in the local current density of deposition at the protrusion relative to less-exposed parts of the surface. Thus, leveling is directly related to differences in the surface concentration of the additive which leads to differences in the local current density of deposition [11].

The deposition current density of metal ions must be close to the end of the Tafel linearity, *i.e.,* it can be treated as the current density in activation-controlled deposition, being independent on the geometry of the system. Hence, the current density at the tip of a protrusion will be equal to the current density on the flat surface in the absence of additive. It should be noted that under such condition "geometric leveling" occurs, but true leveling requires the presence of an additive. If the additive is consumed at the electrode by the reaction

$$\text{Additive} + n^\bullet \text{e}^- \rightarrow \text{Product} \tag{2.91}$$
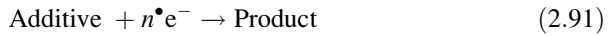
the limiting diffusion current density of the additive, $i^\bullet_{\text{L,tip}}$, to the tip of the protrusion from Fig. 2.1, if the spherical diffusion can be neglected, is given by:

$$i^\bullet_{\text{L,tip}} = \frac{n^\bullet F D^\bullet C_0^\bullet}{\delta - h_\text{p}} \tag{2.92}$$

and that to the flat part of the electrode, $i^\bullet_{\text{L,f}}$, by:

$$i^\bullet_{\text{L,f}} = \frac{n^\bullet F D^\bullet C_0^\bullet}{\delta} \tag{2.93}$$

where $n^\bullet$ is the number of electrons in Eq. (2.91), $D^\bullet$ and C_0 are the diffusion coefficient and concentration of the additive, respectively.

Assuming that the overall current density, i, at each point of the electrode surface is equal, the effective current density, i_{eff}, of metal deposition at the tip of a protrusion is given by:

$$i_{\text{eff},1} = i - \frac{n^\bullet F D^\bullet C_0^\bullet}{\delta - h_\text{p}} \tag{2.94}$$

and on the flat part of the surface by:

$$i_{\text{eff},2} = i - \frac{n^\bullet F D^\bullet C_0^\bullet}{\delta} \tag{2.95}$$

and following the same procedure as in the treatment of the increase of coarseness (see section "Non-dendritic amplification of surface coarseness"), one can write:

$$\frac{\text{d}h_\text{p}}{\text{d}t} = \frac{V}{nF} (i_{\text{eff},1} - i_{\text{eff},2}) \tag{2.96}$$

or in the integral form:

$$h_p = h_{p,0} \exp\left(-\frac{t}{\tau_1}\right) \qquad (2.97)$$

where

$$\tau_1 = \frac{n\delta^2}{n^\bullet V D^\bullet C_0^\bullet} \qquad (2.98)$$

where V (molar volume of metal) and n correspond to the electrodeposited metal. This is the simplest mathematical model of the leveling process [79]. Despite this, it elucidates the physical essence of the phenomenon under consideration well.

Obviously, for this model to be operative, two conditions must be satisfied: (a) the additive must be consumed in some manner at the electrode, so that it must be continuously supplied in order to maintain a certain surface concentration, and (b) the diffusion layer must not follow the microprofile but must have a smoother outer boundary, so that variations in its thickness arise, which cause variations of the diffusion flux of the additive [11].

The first condition is fulfilled with all good leveling agents. Most of them undergo sufficiently strong adsorption to remain long enough at the metal surface to be surrounded by depositing atoms and be incorporated into the deposit. It is the balance between the rate of incorporation and that of diffusion of the substance from bulk of solution which maintains a given surface concentration of the additive. The larger the diffusion flux, the higher is the steady-state surface concentration of the additive. Conversely, higher rates of metal deposition cause a lowering of the latter [11].

There is an optimal range of additive concentration and current density of deposition at which the differences in inhibition of deposition between the peaks and recesses, and hence the effect of leveling, are maximum. At too low surface concentrations of the additive, *i.e.*, low bulk concentration and high current density of deposition, the process is practically uninhibited and little difference in the local current density of deposition can arise. This explains the decrease in the leveling effect with increasing current density [11].

At somewhat higher bulk concentrations and lower current densities, linearity exists between the bulk and the surface concentration. This is the range of maximum difference in inhibition [11].

However, at still higher concentrations, an adsorption/desorption equilibrium tends to be approached leading to a Langmuir-type relationship. Eventually, in spite of incorporation, saturation of the surface is reached and the surface concentration is no longer sensitive to local changes in the diffusion flux of the additives. Hence, differences in inhibition vanish and leveling is lost [11].

One should appreciate that some time is needed for the diffusion layer to develop to the extent that it separates from the surface microprofile and provides for local

differences in the diffusion flux of the additives. Hence, an induction time should be expected before the leveling effect appears. This is demonstrated by the observed sensitivity of the process to current interruptions [77].

Quantitative Treatment

An attempt at a comprehensive quantitative consideration of the problem was made by Krichmar [80]. He proposed that additives adsorbed to the surface of an electrode are incorporated into the deposit at a rate proportional to the surface coverage and current density.

For a sinusoidal profile of the electrode surface, Krichmar [80] obtained an exponential decrease of the amplitude, $H_0(t)$ with time:

$$H_0(t) = H_0 \exp\left(-\frac{t}{\tau_2}\right) \tag{2.99}$$

where τ_2 is a time constant given by:

$$\tau_2 = \frac{a_1}{A_1 \left[B_1\left(C_0^\bullet/\delta\right) - i\right]} \coth\left(\frac{2\pi\delta}{a_1}\right) \tag{2.100}$$

where

$$A_1 = \frac{2\pi V}{nF} \tag{2.101}$$

and

$$B_1 = \frac{K_{\text{lev}}\,\alpha_{\text{lev}}\,F\,n\,D^\bullet C_{0,\text{a}}^\bullet}{R\,T\,\delta V} \tag{2.102}$$

K_{lev} and α_{lev} in the above equations are constants.

An exponential decrease of the amplitude of the surface profile was found experimentally by Krichmar and Pronskaya [81].

Regardless, a model of the current distribution and numerical procedure for the calculation of the change in shape of an electrode, for electrodeposition followed by diffusion-controlled reduction or incorporation of a leveling agent, has been developed [78, 82–84]; the approach of Krichmar [80] seems to be the most important one for understanding the leveling process.

2.2.2.8 Bright Surfaces

Basic Facts

In order for metal coatings to be used for decorative purposes, it is necessary that their surfaces must be smooth and bright. In everyday experience, the optical properties of the metals are associated with high reflectivity and low transmission. For this reason, the terms "mirror bright," "semi bright," and "high bright" are often used when considering electrodeposited metal coatings.

However, there are no precise definitions of these terms. Brightness of a metal surface is usually defined as its reflecting power, measured by the amount of light specularly reflected off the surface, *i.e.,* at an angle equal and opposite to that of the incidence light with respect to the normal to the geometrical surface. A more precise definition, not involving the actual reflectivity of the surface, would be the ratio between specularly and diffusely reflected light [32, 85–87]. The ratio of specular to total reflectivity can also be used for an estimation of the brightness of a surface [88].

The development of the techniques of scanning tunneling microscopy (STM) and atomic force microscopy (AFM) enabled the determination and systematization of structural characteristics which metal surfaces should fulfill in order for light from metal surfaces to be to a high degree specularly reflected [89, 90]. The value of these techniques lies in their ability to provide *local* information concerning the metal deposit, which is unsurpassed by any other technique owing to the resolution. These techniques enable a precise analysis of the topography of a metal surface, *i.e.,* examination of the submicrostructures of metal surfaces to be made. Also, the digital images obtained by these techniques can easily be analyzed by powerful software packages.

The (total) reflected light from an ideally flat (geometrical) surface is exclusively mirror-reflected light, *i.e.,* the light is reflected at an angle equal and opposite to that of the incident light with respect to the normal to the geometrical surface. On the other hand, any (every) real surface possesses surface irregularities, which lead to scattering of the light. Then, reflected light from a metal surface includes diffusely reflected, not only specularly reflected light.

According to Bockris and Razumney [32], if the brightness of a surface is defined as the ability to reflect light only in a direction making an angle with the normal equal to that of the incident beam (*i.e.*, approach to an "ideal mirror"), then the surface will be increasingly bright as the scattering introduced in the reflected light by surface irregularities decreases, that is, as deviations of the actual surface from the ideal, geometrical boundaries are eliminated.

The system which is the nearest approximation to an ideally flat surface, from which reflection of light is exclusively mirror reflection, is the surface of a silver mirror or of mercury. For that reason, reflection and structural characteristics of a silver mirror surface can be taken as the reference standard for bright surfaces [87, 91, 92].
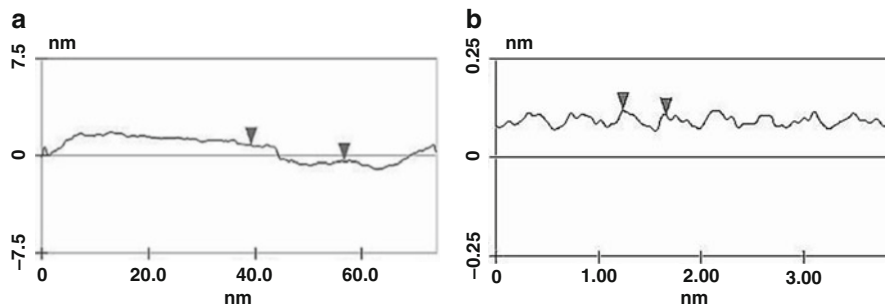
Fig. 2.28 Typical surface profiles of a silver mirror: (**a**) the vertical distance between the markers represents 1.246 nm, and (**b**) line section analysis of the flat part of the surface shown in Fig. 2.28a (Reprinted from Ref. [92] with permission from the Serbian Chemical Society and from Refs. [13, 87] with kind permission from Springer)

Silver Mirror

The reflection of light from a silver mirror surface is mostly mirror reflection and the degree of diffuse reflection is very small (up to 2 %). The degree of mirror reflection from this surface is also very close to the ideal reflectance of silver [87, 91, 92]. The silver mirror surface consists of parts parallel to the base and flat on the atomic level with low-step heights between them, as is shown in Fig. 2.28. It is clear that bright metal surfaces must be similar to the surface of the mirror.

Electropolished Surfaces

The phenomenon of decreasing the surface coarseness of a metal upon anodic dissolution under certain conditions is defined as electropolishing. In cases when polishing occurs, the current–voltage curve was found to exhibit a plateau characteristic for diffusion control of the dissolution process. Some facts point to the complex nature of the phenomenon of electropolishing.

It was also found that systems undergoing electropolishing exhibit a significant photoelectrochemical effect. This corresponds to the region of limiting diffusion current densities and also to the maximum polishing effect.

This suggests to the existence of a photosensitive semiconducting film at the surface and to a possible role of this film in the electropolishing process. Subsequent measurements of the capacitance and resistance of the double layer as functions of potential have shown that this film must be a very thin and a well-conducting one.

In spite of all this, considerable evidence has accumulated justifying the treatment of the electropolishing process as an essentially transport-controlled phenomenon; this film could be related to the effect of brightening [11].

A quantitative model was suggested by Edwards [93] and elaborated by Wagner [94]. According to this model, the metal ions produced are complexed by

a component of the electropolishing solution (*e.g.*, phosphate ions or water molecules). Hence, for the reaction to be completed, not only must ions be formed, but also acceptor species have to diffuse to the surface from the bulk of the solution in order to form a complex reaction product. Diffusion of the acceptor from the bulk of the solution to the surface determines the overall rate of reaction.

Hence, differences in acceptor fluxes of different points at the surface arise. The slower diffusion of the acceptor to the recessed parts could cause an increased concentration of free metal ions. This would have many possible consequences such as increasing the cathodic partial current which reduces the net dissolution current, producing changes in the reaction layer such as the formation of an oxide film by hydrolysis, making room for an additional phenomenon observed in electropolishing–brightening. This could be related to the dissolution of facets and other crystallites. Brightening seems to occur when the surface becomes covered by a protective film, which controls the rate of dissolution and makes it a random process, the energetic advantages of atoms at facets and dislocations being lost. Thus, it could be concluded that the Edwards–Wagner model seems to provide a reasonable basis for development of a comprehensive theory of the electropolishing process [11].

The reaction between a metal ion and a ligand is usually sufficiently fast, but it is the insufficient supply of the latter, which could cause the inhibition of this step and make it the rate-determining step.

The anodic partial current is independent of the presence of the ligand. However, if the ligand becomes scarce, the concentration of the free metal ions increases, and, as a result, the cathodic partial current is increased as well. In an ideal case, when diffusion of free metal ions away from the electrode is negligible, the difference between the two partial currents, *i.e.*, the net dissolution current, must be proportional to the flux of the ligand. This case was considered in detail by Wagner [94] who assumed a molecular diffusion mechanism of supply through a fixed hydrodynamic boundary layer of thickness, δ, much larger than wavelength and amplitude of the surface profile.

For a sinusoidal profile of the electrode surface, Wagner [94] gives:

$$H_0(t) = H_0 \exp\left(-\frac{t}{\tau_3}\right) \tag{2.103}$$

where H_0 is the initial surface amplitude, and τ_3 is given by:

$$\tau_3 = \frac{\omega\delta}{2\pi DVC^0} \tag{2.104}$$

ω is the wavelength of the profile and C^0 is the concentration of the acceptor.

Equation (2.104) shows that the electropolishing process is faster if the thickness of the diffusion layer is smaller and if the bulk concentration of the ligand is larger. Also, it is faster, the smaller the wavelength of the surface profile is. The latter reflects the radius of curvature of the elevations and recesses, and the result

indicates that "microroughness" will disappear more rapidly than "macroroughness," which is in accordance with experimental experience (see also Fig. 2.29c–g). The exponential time dependence of the height of the elevations given by Eq. (2.104) is in agreement with the findings of Krichmar and Pronskaya [95]. The electropolished metal surfaces are characterized by a specular reflection of light.

The 3D STM images of the Cu surface polished only mechanically and the Cu surface polished both mechanically and electrochemically are shown in Fig. 2.29a, b, respectively. In order to determine which structural features determine brightness, the flat parts of the profile, which were parallel to the base, were examined under different magnifications. The line sections of parts of the flat surfaces were investigated first at lower magnifications and then at increasingly higher ones. Following this procedure, Fig. 2.29c–f were obtained.

In the case of the mechanically polished surface, the amplitude of roughness was several atomic diameters of Cu (Fig. 2.29c, d), whereas the mechanically and electrochemically polished surface exhibited smoothness on the atomic level (Fig. 2.29e, f). The increase in the specular reflection of 20–25 % is due to this fact. It is interesting to note (Fig. 2.29g) that the structure of the bright surface was not oriented. This is in accordance with the assumption that the dissolution process under polishing conditions is a random process.

Hence, it can be concluded that the condition for mirror brightness of a metal surface is smoothness on the atomic level of a suitably oriented flat part of the metal surface with low-step heights between, as in the case of a silver mirror.

Electrodeposited Surfaces

The STM images of the copper coating electrodeposited in the presence of the brightening additives that exhibit high degree of mirror reflection which approached very nearly the ideal reflectance of copper are shown in Fig. 2.30 [87, 91, 96].

The high degree of mirror reflection of this coating was determined by flat and mutually parallel parts of the surface (Fig. 2.30a, b). The distances between adjacent flat parts were several atomic diameters of copper (Fig. 2.30c) [87]. The flat parts of the surfaces were smooth on the atomic scale (Fig. 2.30d). The mean size of these atomically flat parts was estimated by STM software measurements, using option of the determination of the autocovariance (ACVF) and power spectral density (PSD) functions, and they were: (160×170) nm^2 – determined by ACVF function and 198 nm – determined by PSD function [87].

The flat and mutually parts of the surface appear because the growth of the deposit in the vertical direction is suppressed by the adsorption of the additive [89]. This happens if the organic additive adsorbs strongly on the top of the copper crystallites and inhibits the formation of new growth centers. Deposition then occurs dominantly at the edges of the crystallite, resulting in lateral expansion of the layers and the formation of smooth terraces on the atomic level. The growth of a
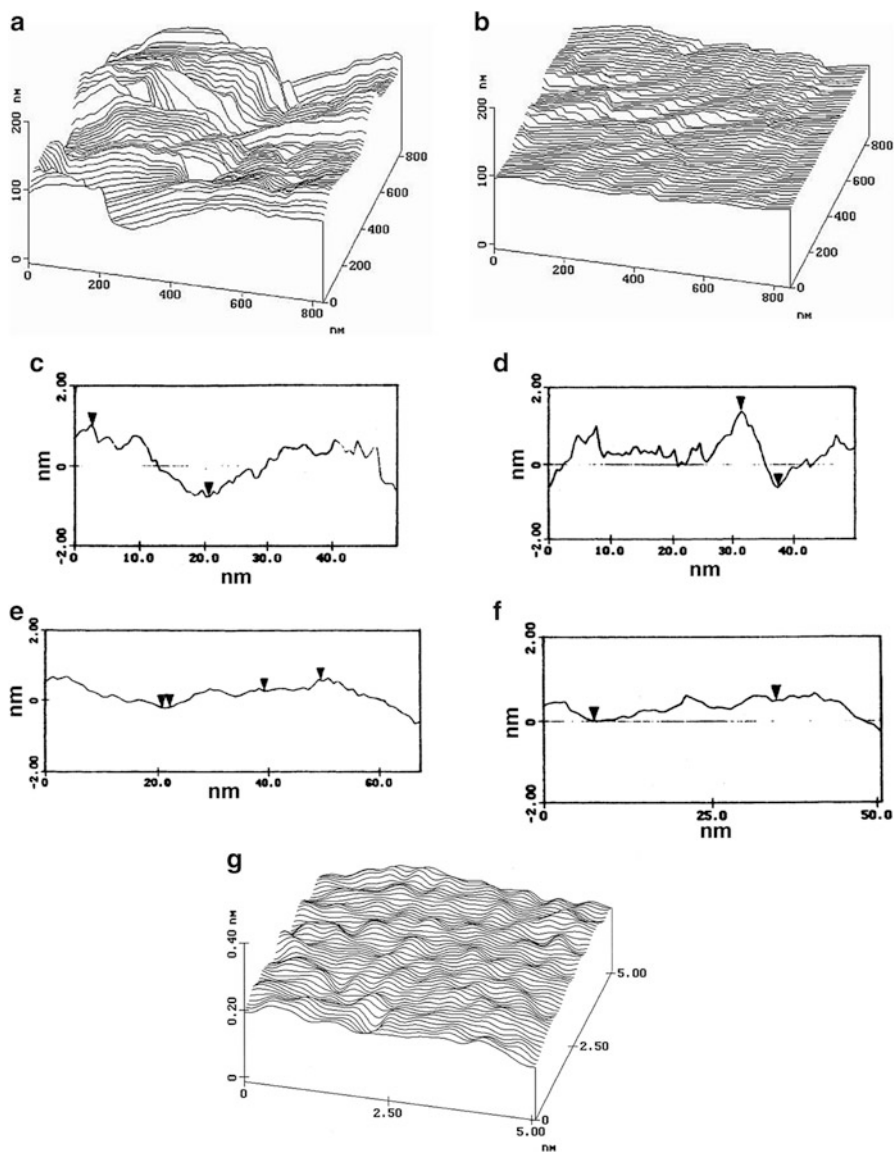
Fig. 2.29 The 3D STM images of (**a**) only mechanically polished Cu surfaces, (**b**, **g**) both mechanically and electrochemically polished, and the surface profiles of the flat parts from (50×50) nm^2 samples areas: mechanically (**c–d**) and both, mechanically and electrochemically (**e–f**) polished Cu surface. The vertical distances between the labels of the maximum and minimum points are (**c–d**) $\Delta l = 2.0$ nm, (**e–f**) $\Delta l = 0.51$ nm (Reprinted from Ref. [87] with kind permission from Springer, Ref. [91] with permission from Elsevier, and Ref. [96] with permission from the Serbian Chemical Society)
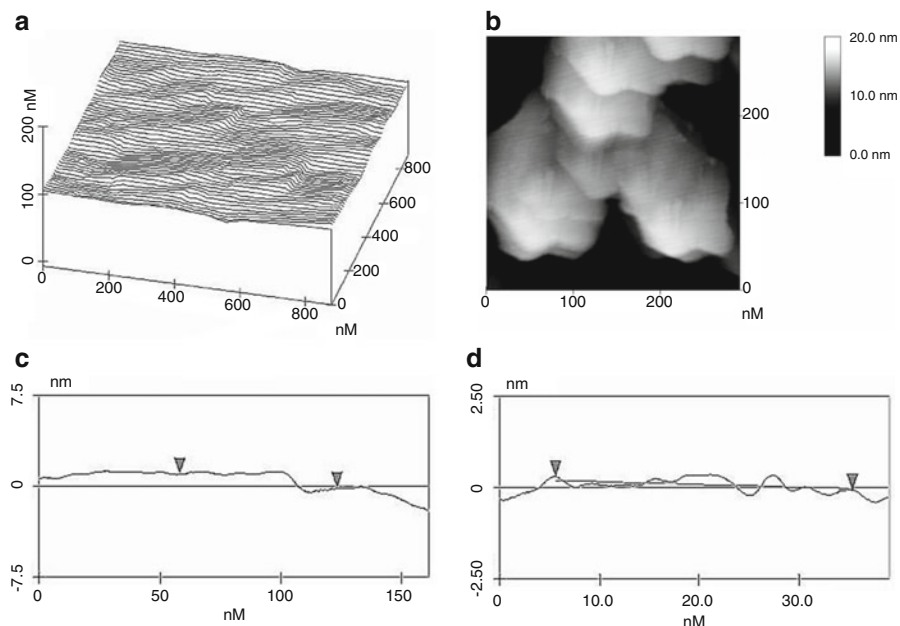
Fig. 2.30 The STM images of 25 μm thick the copper coating electrodeposited from solution: 240 g dm^{-3} CuSO$_4$·5 H$_2$O + 60 g dm^{-3} H$_2$SO$_4$ + 0.124 g dm^{-3} NaCl + 1.0 g dm^{-3} modified polyglycol ether (Lutron HF 1) + 1.0 g dm^{-3} poly(ethylene glycol) M$_n$ = 6000 (PEG 6000) + 1.5 mg dm^{-3} 3 -mercapto propane sulfonate. Scan size: (**a**) (880 × 880) nm^2, and (**b**) (300 × 300) nm^2, (**c**) the line section analysis from the portion of the STM surface of the copper coating shown in Fig. 2.30a. The distance between markers is 1.177 nm, and (**d**) the line section analysis of the flat part of surface of the copper coating shown in Fig. 2.30c (Reprinted from Ref. [91] with permission from Elsevier and Ref. [87] with kind permission from Springer)

new layer starts from defect arising at the interface between two adjacent crystal-lites, and surfaces like those in Fig. 2.30a are formed.

Mirror brightness of copper surfaces is not associated with their preferred orientation. This copper coating showed (200) preferred orientation [87]. On the other hand, the copper coating electrodeposited from the copper solution containing thiourea as the brightening additive showed the (111) preferred orientation, while the mirror bright copper surface polished both mechanically and electrochemically was relatively disordered with an increased ratio of copper crystallites oriented in (200), (220), and (311) planes [87, 91, 97].

The 3D STM image of the zinc coating having the high degree of mirror reflection is shown in Fig. 2.31a. This zinc coating obtained with the addition of dextrin/salicylaldehyde mixture as the brightening additives were relatively smooth, but without large flat and mutually parallel parts of the surface, which were characteristic of the previously observed copper surfaces [98]. Analysis of the zinc coating at even higher magnification (Fig. 2.31b) showed that the zinc coating was constructed from hexagonal zinc crystals. XRD (X-ray diffraction) analysis of
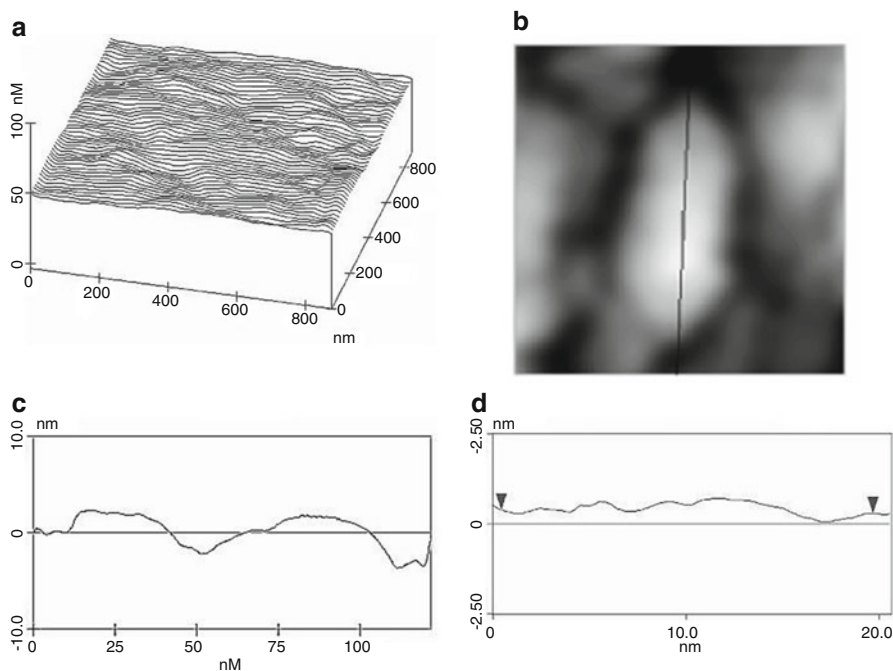
Fig. 2.31 The STM images of 25 μm thick the zinc coating electrodeposited from solution: 300 g dm^{-3} ZnSO$_4$· 7 H$_2$O + 30 g dm^{-3} Al$_2$(SO$_4$)$_3$· 18 H$_2$O + 15 g dm^{-3} NaCl + 30 g dm^{-3} H$_3$BO$_3$ + 3.0 g dm^{-3} dextrin + 2.8 ml dm^{-3} salicylaldehyde. Scan size: (**a**) (880 × 880) nm^2, and (**b**) (50 × 50) nm^2, (**c**) the line section analysis from the portion of the STM surface of the zinc coating shown in Fig. 2.31a, and (**d**) the line section analysis of the hexagonal zinc crystal shown in Fig. 2.31c (Reprinted from Ref. [98] with permission from the Serbian Chemical Society and Refs. [87, 97] with kind permission from Springer)

the zinc coating showed that the zinc crystallites were oriented in the (110) plane only. The (110) plane of the h.c.p. crystal lattice is the plane where the most densely packed atom rows in the most densely packed lattice plane (basal plane) stand upright to the cathode surface and when the crystallites of the deposits are oriented so that the most densely populated atom plane is perpendicular to the substrate, then the deposited metal adopts an outward type of growth [87].

The line section analysis of the zinc coating shown in Fig. 2.31a is given in Fig. 2.31c, from which it can be observed that the top surfaces of the hexagonal zinc crystals are relatively flat and mutually parallel. The distance between the top plane of a hexagonal zinc crystal and the boundary with the adjacent zinc crystal was several atomic diameters of zinc [87]. The roughness of the hexagonal zinc crystals was less than the atomic diameter of zinc, *i.e.,* these zinc crystals were smooth at the atomic level (Fig. 2.31d). The mean size of these hexagonal zinc crystals (estimated by the STM software data processing) was by approximately (18 × 20) nm^2 by the ACVF and about 20 nm by the PSD functions.

The similar reflection and structural characteristics also showed the zinc coatings electrodeposited onto the zinc substrate [99], as well as those electrodeposited from acid sulfate solution with the addition of dextrin/furfural mixture [100].

The similarity of reflection and structural characteristics of the copper surfaces polished both mechanically and electrochemically, and the copper and zinc coatings electrodeposited with the corresponding brightening additives with those of silver mirror as the reference standard just enabled systematization of the conditions which metal surfaces must fulfill to be mirror bright. These conditions are:

I. *Reflection condition*: high degree of mirror reflection which approaches to the ideal reflectance of the corresponding metal
II. *Structural conditions*:

   (a) Flat parts of the surface parallel to the base which are smooth on the atomic level
   (b) Distances between adjacent flat parts which are comparable with the distances between the adjacent flat parts of a silver mirror

Mathematic model that treats brightness of metal surfaces from the point of view of geometrical optics only is proposed [87, 91]. The proposed model is valid if the following assumptions were fulfilled:

- Metal surfaces are divided into equal elementary parts for which the surface area is n_s.
- The flat parts are smooth.
- The light falls onto the surface at a determined angle and is reflected from the surface only in the direction making an angle with the normal equal to the angle of incidence.
- *The upper flat parts of a surface area* ($k_u \cdot n_s$ parts) reflect light completely.
- The parts of *the lower flat parts of a surface area* ($k_d \cdot n_s$ parts) do not reflect light completely because they are screened by the height of *the lateral parts of a surface area* ($k_l \cdot n$ parts). The screened zones are made by both incident and reflected lights.

In total, the brightness of a surface is determined by the ratio of flat parts to the surface between adjacent flat parts. Increasing the distance between adjacent flat parts leads to a decreasing brightness of the surface [91].

The parts of the surface which are not able to reflect light, e_i, depend on the angle of incidence and the height of the lateral part of the surface.

All metal surfaces can be represented by one equivalent surface which consists of row elementary surface units. One such surface unit is represented in Fig. 2.32.

The part of the surface which is screened, e_i, and so cannot reflect light is given, for an angle of incidence, θ_i, by Eq. (2.105):

$$e_i = k_{l,i} \cdot n_s \cdot \operatorname{tg} \theta_i \qquad (2.105)$$

where $i = 0, 1, 2, 3.......$

Fig. 2.32 Line section simulation of one surface unit a metal surface (Reprinted from Ref. [91] with permission from Elsevier and Ref. [87] with kind permission from Springer)
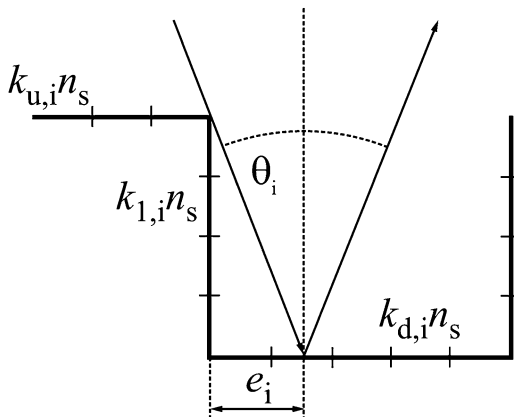
Then, having in mind the fact that the screened zones are made by both incident and reflected lights, the brightness of a surface, defined as the ratio of the geometrical minus the screened surface and the geometrical surface, can be given by Eq. (2.106):

$$
\text{brightness} = \frac{\sum_1^\infty k_{u,i} \cdot n_s + \left(\sum_1^\infty k_{d,i} \cdot n_s - 2\sum_1^\infty e_i \right)}{\sum_1^\infty k_{u,i} \cdot n_s + \sum_1^\infty k_{d,i} \cdot n_s}
$$

$$
= \frac{k_u \cdot n_s + (k_d \cdot n_s - 2 \cdot e)}{k_u \cdot n_s + k_d \cdot n_s} = \frac{k_u \cdot n_s + \left(k_d \cdot n_s - 2 \cdot \sum_1^\infty k_{l,i} \cdot n_s \cdot \mathrm{tg}\theta_i \right)}{k_u \cdot n_s + k_d \cdot n_s}
$$

$$
= \frac{k_u + (k_d - 2 \cdot k_l \cdot \mathrm{tg}\theta_i)}{k_u + k_d} = 1 - 2\frac{k_l}{k_u + k_d}\,\mathrm{tg}\theta_i
$$

(2.106)

where

$$
k_u = \sum_1^\infty k_{u,i}, \;\; k_d = \sum_1^\infty k_{d,i}, \;\; k_l = \sum_1^\infty k_{l,i}, \;\; e = \sum_1^\infty e_i
$$

Hence, according to Eq. (2.106), the brightness of a surface is a function of the incident angle, θ_i, and the ratio between the flat parts, $(k_u + k_d)$ and the lateral parts, k_l. Increasing the lateral parts of a surface, k_l, leads to a decrease in the brightness of the surface. Therefore, when $k_l \to 0$, then the brightness of the surface approaches that of a mirror.

The boundary conditions of Eq. (2.106) depend on the expression in the bracket [87]. *The lower flat parts of a surface area* will reflect light only if tangent of an

incident angle of light is smaller than the ratio ($k_{d,i}/2\,k_{l,i}$). On the other hand, for larger incident angles or an incident angle equal to this ratio, *the lower flat parts of a surface area* will not be able to reflect light.

It is necessary to note that an increase of the lateral parts of a surface, k_l, is accompanied by an increase of the "degree of development of the surface." The later quantity, S', defined as the ratio of the real (actual) to geometrical surface, is given by Eq. (2.107):

$$S' = \frac{k_u \cdot n_s + k_d \cdot n_s + 2k_l \cdot n_s}{k_u \cdot n_s + k_d \cdot n_s} = 1 + 2\frac{k_l}{k_u + k_d} \qquad (2.107)$$

Then, according to Eqs. (2.106) and (2.107), the brightness of a surface can be defined by Eq. (2.108):

$$\text{brightness} = 1 - S_s \text{tg}\theta_i \qquad (2.108)$$

or, in %, by Eq. (2.108a):

$$\text{brightness (in\%)} = 100 - S_s(\text{in\%})\text{tg}\theta_i \qquad (2.108a)$$

where $S_s = (S' - 1)$ – a quantity experimentally measurably by STM data processing as *the surface area diff*.

The excellent agreement within the limits of the experimental error, between experimentally obtained values of mirror-reflected light for incident angles of 5° and 30° and those of brightness obtained according to the proposed model using experimentally determined values of *the surface area diff* (Eq. 2.108a), was observed [87].

2.2.3 Active Microelectrodes Inside the Diffusion Layer of the Inert Macroelectrode

2.2.3.1 Granular Growth

Granular deposits consisting of independently growing grains with a highly developed surface area are obtained by deposition of metals in processes characterized by large values of the exchange current density [101–103]. In some cases, they consist of grains growing independent of each other until a compact film [54, 104] or spongy deposit on it is formed [54].

Granular Growth of Silver

It is shown in Fig. 2.33 that various crystallographic forms, some of them ideal, are obtained during silver deposition at low overpotentials from pure silver nitrate
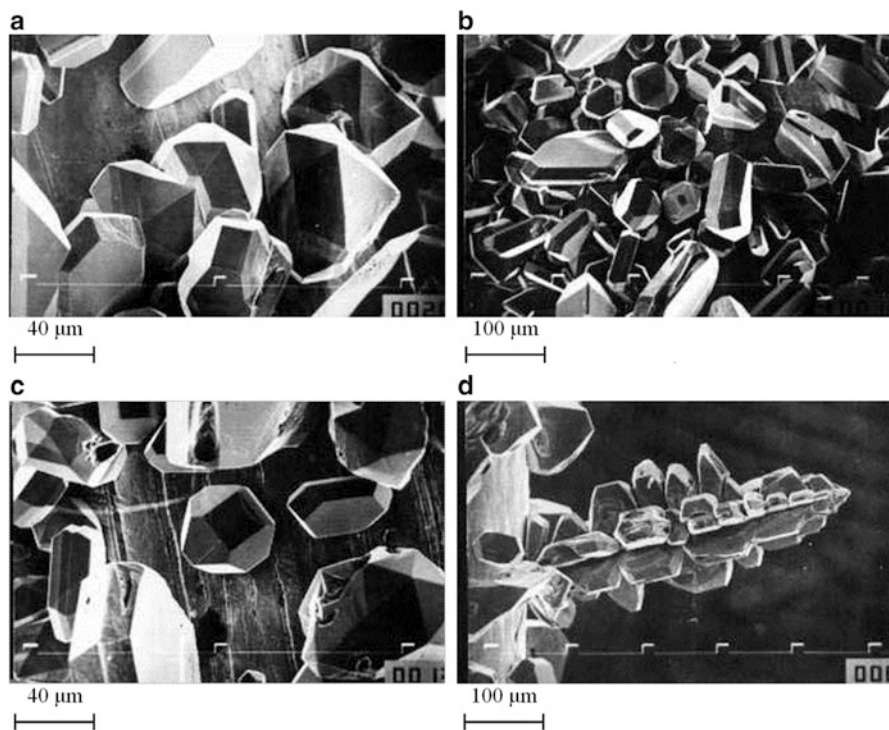
Fig. 2.33 Silver deposits obtained potentiostatically on platinum electrode from 0.10 M AgNO$_3$ in 100 g dm^{-3} NaNO$_3$ at the room temperature. Quantity of electricity: 2 mA h cm^{-2}. Deposition overpotential: (**a**) 60 mV, (**b**) 60 mV, (**c**) 70 mV, and (**d**) 70 mV (Reprinted from Refs. [13, 67] with kind permission from Springer)

solution, due to the independent grain growth inside the zones of zero nucleation, probably if 2D nucleation is the rate-determining step [105]. Dendritic growth starts at higher overpotentials. It can be seen from Fig. 2.33b, c that dendritic growth initiation is mainly related to the appearance of twinned forms in which indestructible reentrant groove is formed, being the precursors of dendrite. Hence, a granular deposit will be formed at overpotentials lower than those for the formation of dendrite precursors and dendritic growth initiation.

Granular Growth of Lead

The typical Pb granules obtained in the potentiostatic regime of electrolysis are shown in Fig. 2.34. Similar to silver granules, granules of various shapes were produced by the electrodeposition processes. The granules, such as octahedrons and hexagons, as well as many various types of twinned particles: single-twinned, multiply-twinned (MTPs), lamellar-twinned (LTPs), and many other complicated
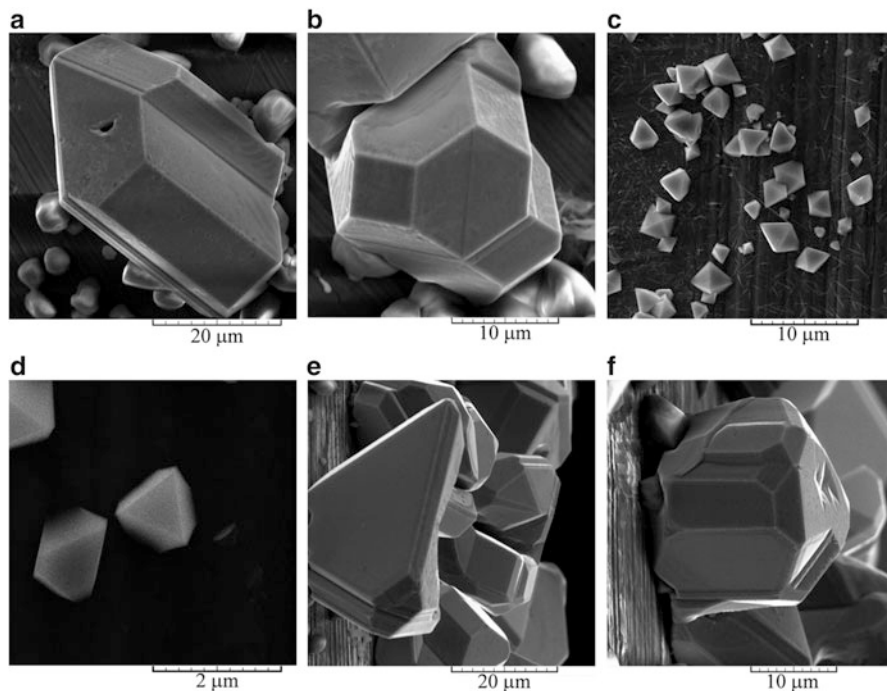
Fig. 2.34 Lead granules obtained by potentiostatic regime of electrolysis at an overpotential of 5 mV from: (**a–d**) 0.020 M $Pb(NO_3)_2$ in 2.0 M $NaNO_3$, and (**e** and **f**) 0.040 M $Pb(NO_3)_2$ in 2.0 M $NaNO_3$

shapes denoted as polyparticles, were synthesized through regulation of the parameters of electrolysis.

2.2.3.2 Mathematical Model and Polarization Curve Equation for the Metal Deposition on Partially Covered Inert Electrode

The ensemble of microelectrodes consists of microelectrodes placed on the inert surface at distances between their centers larger than their diameter. There are two conditions under which the particles of active metal placed on the surface of a macroelectrode can represent microelectrodes. The first condition is that the substrate is conducting, but inert relative to the process under consideration. The second one is that the grains are sufficiently small to permit activation control of the electrochemical process on them, making, thus, mixed overall control, as in the case of the tips of growing dendrites [3, 5, 20], or during the induction time of the formation of spongy deposits [54].

Assuming homogeneously distributed, equal to each other, hemispherical grains of the catalyst on an inert substrate, in a way similar to that used by Gileadi [10] to

Fig. 2.35 A schematic presentation of the top view of the surface of an inert macroelectrode modified with microelectrodes of catalyst (Reprinted from Ref. [6] with permission from Elsevier and Ref. [1] with kind permission from Springer)
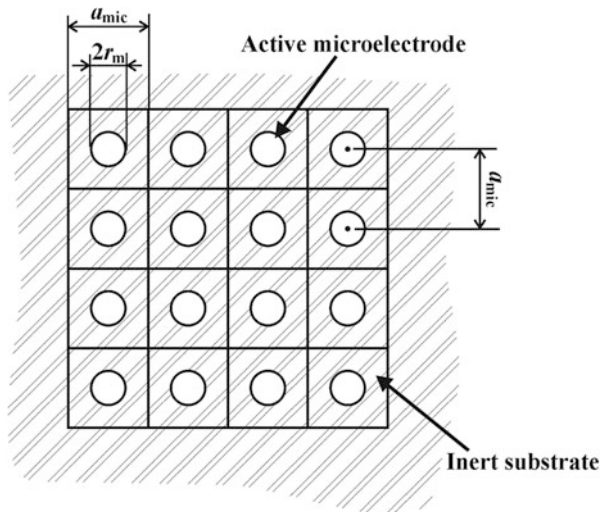
describe an ensemble of microelectrodes, the surface of the macroelectrode can be presented by an idealized model, as in Fig. 2.35, and the number of grains per cm^2 is given by:

$$N = \frac{1}{a_{mic}^2} \tag{2.109}$$

It is obvious from Fig. 2.35 that the edge size, a_{mic}, of a square of the surface of the inert macroelectrode belonging to one such particle is equal to the distance between the centers of the closest particles. If

$$a_{mic} = x \cdot 2r_m \tag{2.110}$$

where r_m is the radius of the microelectrode and x is the ratio of the distance between the centers of the particles and the particle diameter, Eq. (2.109), can be rewritten in the form:

$$N = \frac{1}{4r_m^2 \cdot x^2} \tag{2.111}$$

The surface of each hemispherical microelectrode, S_m, is:

$$S_m = 2r_m^2 \cdot \pi \tag{2.112}$$

and the working surface of catalyst per square centimeter of macroelectrode, S_w, is then:
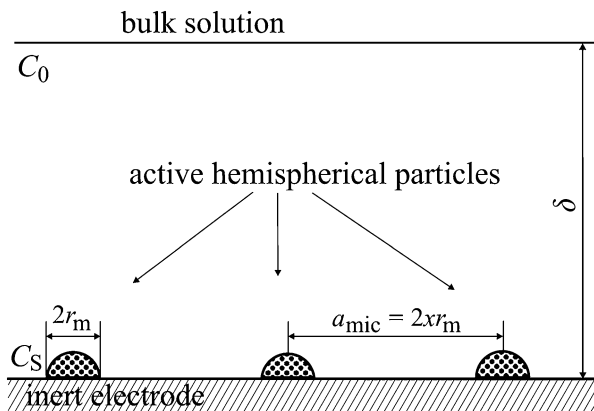
Fig. 2.36 Schematic presentation of the cross section of the diffusion layer of a partially covered inert electrode with hemispherical active particles, where r_m is the radius of the microelectrodes, δ is the diffusion layer thickness of the macroelectrode, C_0 and C_s are the bulk and the surface concentrations of reacting ions, respectively, x is the ratio of the distance between the centers of neighboring particles and the particle diameter, and $\delta \gg r_m$ (Reprinted from Ref. [6] with permission from Elsevier and Ref. [1] with kind permission from Springer)

$$S_w = N \cdot S_m = \frac{\pi}{2x^2} \tag{2.113}$$

or

$$S_w = \frac{2r_m^2 \pi}{a_{mic}^2} \tag{2.114}$$

if Eq. (2.110) is taken into account, being dependent on the ratio r_m/a_{mic}.

A schematic presentation of the cross section of the diffusion layer of an inert macroelectrode partially covered with small active hemispherical particles is shown in Fig. 2.36, taking into account that $\delta \gg r_m$.

A mathematical model can be derived under the assumption that the electrochemical process on the microelectrodes inside the diffusion layer of a partially covered inert macroelectrode is under activation control, despite the overall rate being controlled by the diffusion layer of the macroelectrode. The process on the microelectrodes decreases the concentration of the electrochemically active ions on the surfaces of the microelectrodes inside the diffusion layer of the macroelectrode, and the zones of decreased concentration around them overlap, giving way to linear mass transfer to an effectively planar surface [42]. Assuming that the surface concentration is the same on the total area of the electrode surface, under steady-state conditions, the current density on the whole electrode surface, i, is given by:

$$i = \frac{nFD\,(C_0 - C_s)}{\delta} \tag{2.115}$$

Obviously, the current density from Eq. (2.115) is due to the difference in the bulk, C_0, and surface concentration, C_s, of the reactive ions. Considering the concentration dependence of the exchange current density [37] (see Eqs. (1.16) and (1.17)), the current density on the macroelectrode can also be written as:

$$i = S_w i_0 \left(\frac{C_s}{C_0}\right)^{\zeta} (f_c - f_a) \tag{2.116}$$

assuming a reversible activation-controlled electrode process on the hemispherical active microelectrodes on an inert substrate, where S_w is the active surface per cm^2 of the macroelectrode and i_0 is the exchange current density on the massive active electrode, standardized to the apparent electrode surface.

The current densities given by Eqs. (2.115) and (2.116) are mutually equal and substitution of C_s/C_0 from Eq. (1.18) into Eq. (2.116) produces

$$i = S_w i_0 \left(1 - \frac{i}{i_L}\right)^{\zeta} (f_c - f_a) \tag{2.117}$$

or, for $\zeta = 1$, after rearranging

$$i = \frac{S_w i_0 (f_c - f_a)}{1 + \frac{S_w i_0 (f_c - f_a)}{i_L}} \tag{2.118}$$

where i_L is the limiting diffusion current density on the macroelectrode standardized to the apparent electrode surface.

It is obvious that

$$i_{0,\text{eff}} = S_w i_0 \tag{2.119}$$

where $i_{0,\text{eff}}$ is the effective value of the exchange current density relative to the total surface of a partially covered electrode.

If Eq. (2.120)

$$\frac{S_w i_0 (f_c - f_a)}{i_L} \gg 1 \quad \text{and} \quad f_c > f_a \tag{2.120}$$

is valid even for small S_w and overpotentials, all the surface behaves as an active one if $i_0/i_L \to \infty$ meaning the ohmic control of electrodeposition.

Figure 2.37 shows the polarization curves for Ag electrodeposition from 0.50 M $AgNO_3$ in 0.20 M HNO_3 recorded on both a graphite electrode and graphite electrode previously plated with silver from the ammonium electrolyte (electrolyte containing 0.10 M $AgNO_3 + 0.50$ M $(NH_4)_2SO_4 + NH_4OH$ to dissolve the silver sulfate precipitate that was used for this purpose) [1, 6].
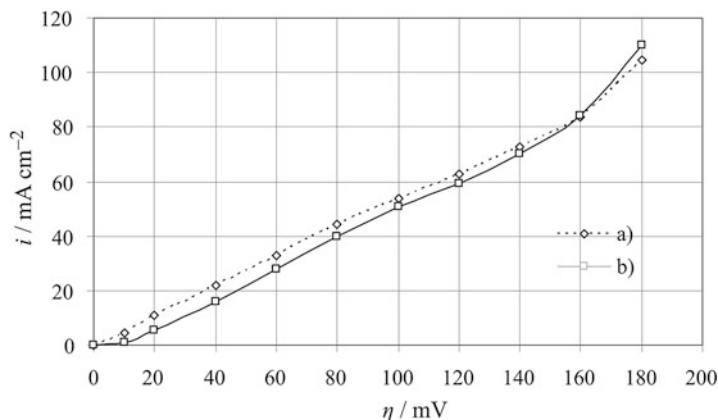
Fig. 2.37 Polarization curves for silver electrodeposition from the nitrate solution on (*a*) a graphite electrode previously plated with silver from the ammonium solution and (*b*) an uncovered graphite electrode (Reprinted from Ref. [1] with kind permission from Springer and Ref. [6] with permission from Elsevier)

From Fig. 2.37, it can be noticed that the polarization curves for deposition on the compact silver layer and on the uncovered graphite electrode are practically the same (please note that there is small difference in initial parts of the polarization curves due to the different nucleations on silver and graphite electrodes). In both cases, the ohmic-controlled deposition can be noticed up to about 100 mV. In both cases, an overpotential of 120 mV belongs to the region in which a slight decline in the slope of the polarization curve indicates an increased degree of diffusion control. At overpotentials larger than 140 mV, a strong increase in the current density with increasing overpotential occurs because of the initiation of dendritic growth [3, 5]. The polarization curves on platinum electrodes were very similar to those obtained on graphite ones [6].

The surface of completely covered graphite electrode by deposition from ammonium bath is shown in Fig. 2.38a, while the silver deposit obtained after polarization measurement up to an overpotential of 120 mV on an uncovered graphite electrode is shown in Fig. 2.38b. This electrode surface is partially covered because of the overlapping of the nucleation exclusion zones, being the ideal physical model of a partially covered inert electrode. The regular crystal form of the grains in Fig. 2.38b confirms that the deposition on the microelectrodes is not under diffusion control [16, 106], despite the overall deposition rate that is determined by diffusion to the macroelectrode.

The current density on the electrode from Fig. 2.38b, with coverage of about 20 %, is practically the same as on a completely covered graphite electrode, as can be seen from Fig. 2.37 at an overpotential of 120 mV. This is because the exchange current density for the silver electrodeposition process from nitrate baths is large [58, 107]. A similar situation appears in silver electrodeposition on platinum [6].
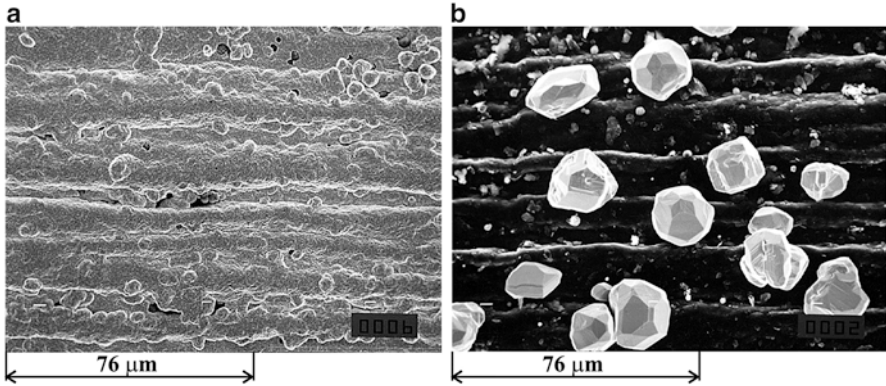
Fig. 2.38 The physical model of a partially covered inert electrode with active grains and a completely covered inert electrode: (**a**) a graphite electrode completely covered by deposition from the ammonium electrolyte; current density on the electrode completely covered with silver was 62.5 mA cm^{-2} at an overpotential of 120 mV in the nitrate electrolyte and (**b**) the silver deposit on the graphite electrode after the polarization measurements ended at an overpotential of 120 mV in the nitrate electrolyte; current density on such electrode was 59.4 mA cm^{-2} at the same overpotential in the nitrate electrolyte (Reprinted from Ref. [1] with kind permission from Springer and Ref. [6] with permission from Elsevier)

2.2.4 Dendritic Growth Initiation Inside Diffusion Layer of the Macroelectrode in the Case of Very Fast Electrodeposition Processes

The initiation of dendritic growth in the case of very fast electrodeposition processes also will be followed by an increase of the deposition current density, and the overall current density will be larger than the limiting diffusion current on a flat active electrode. Based on the above discussion, the polarization curve equation in the mixed ohmic diffusion-controlled electrodeposition of metals can be determined as [108]:

$$i = \frac{\kappa\eta}{L_c} \text{ for } 0 \leq \eta < i_L\frac{L_c}{\kappa} = \eta_i \tag{2.121}$$

$$i = i_L \text{ for } \eta_i \leq \eta < \eta_c \tag{2.122}$$

$$i = i_L\theta + (1 - \theta)i_0\frac{(f_c - f_a)}{N}\sum_{i=1}^{i=N}\left(\frac{h_{i,e}}{\delta}\right)^{\xi} \text{ for } \eta_c \leq \eta \tag{2.123}$$

where $N = N(t)$ is the number of dendrites and $\theta = \theta(t) \leq 1$, where θ is the part of the electrode surface uncovered by dendrites.

Equation (2.121) describes the linear part of the polarization curves for tin [109], silver [1, 6], and lead [34, 35, 110, 111] deposition, and Eq. (2.122) foresees the inflection point in the cases when η_c is low and the resistance of electrolyte is large. Finally, Eq. (2.123) describes the part of the polarization curve after the inflection point characterized by the fast increase of current density with increasing the overpotential (see Chap. 1; Sect. 1.3.1.1).

In the case of the fast electrochemical processes, the diffusion control follows after the linear dependence of the current density on the overpotential, *i.e.,* after the ohmic part at the polarization curve. The overpotential which initiates dendritic growth is denoted as the critical overpotential for dendritic growth initiation, η_i, and it is overpotential at which the system enters diffusion control of the electrodeposition. The critical overpotential for instantaneous dendritic growth, η_c, is overpotential at which diffusion control becomes complete, and this overpotential corresponds to the inflection point at the polarization curve [111]. After the inflection point, the electrodeposition systems remain diffusion controlled ones, and the rapid increase of the current density after the inflection point is result of the fast growth of dendrites and strong increase of the surface area. Then, using the electrochemical definition of a dendrite, it follows that this sudden and rapid increase of the current density can be mainly ascribed to the activation-controlled electrodeposition at the tips of the formed dendrites. Hence, for this part of the polarization curve, it can be concluded that there is elimination of mass transfer limitations due to instantaneous dendritic growth and the activation control at the tips of growing dendrites.

The polarization curve for Ag electrodeposition from 0.50 M AgNO$_3$ in 0.20 M HNO$_3$, onto a graphite electrode, is shown in Fig. 2.39. The polarization curve in Fig. 2.39 means that mass transfer limitations were decreased or even eliminated. The SEM photomicrographs of the deposit corresponding to the points from Fig. 2.39 are shown in Fig. 2.40.

Fig. 2.39 The polarization curve for silver electrodeposition from nitrate solution on a graphite electrode (Reprinted from Ref. [108] with permission from Elsevier and Ref. [1] with kind permission from Springer)
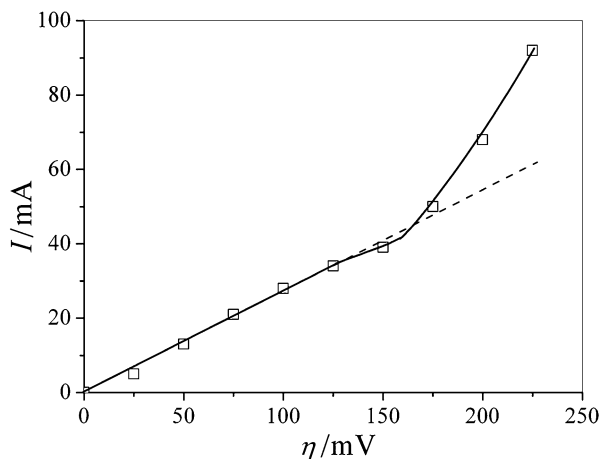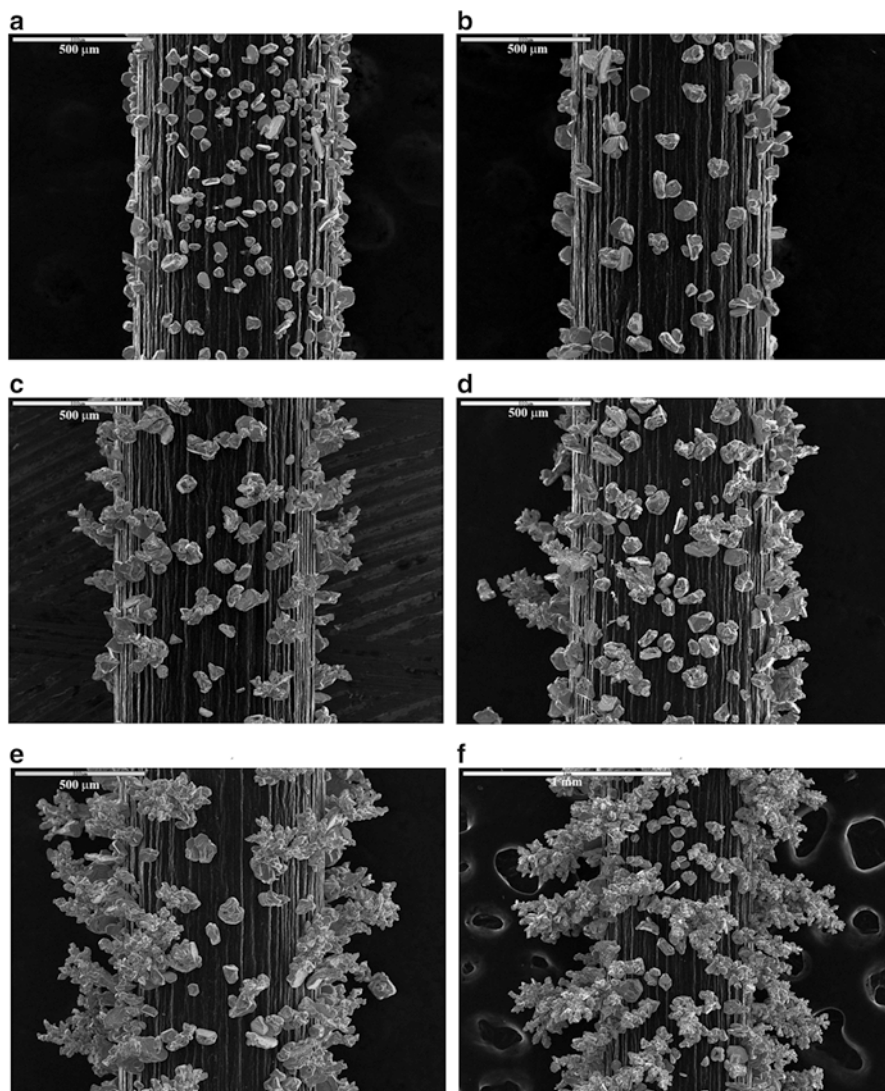
Fig. 2.40 The SEM photomicrographs of the silver deposit obtained on a graphite electrode obtained after the recording of the current at different overpotentials in polarization measurements: (**a**) 100 mV, (**b**) 125 mV, (**c**) 150 mV, (**d**) 175 mV, (**e**) 200 mV, and (**f**) 225 mV (Reprinted from Ref. [108] with permission from Elsevier and Ref. [1] with kind permission from Springer)

It can be seen from Figs. 2.39 and 2.40a that only grains are obtained at an overpotential of 100 mV indicating that electrodeposition process was not under diffusion control [108]. From Figs. 2.39 and 2.40b, it follows that electrodeposition at 125 mV is still out of the diffusion control. At 150 mV, the current density is somewhat lower than that which could be expected from the linear dependence of

the current on the overpotential. This indicates on the initiation of diffusion control of the deposition process, but also to the initiation of dendrite growth, which compensates the mass transfer limitations (Figs. 2.39 and 2.40c). The point corresponding to an overpotential of 150 mV can be considered as the inflection point at the polarization curve in Fig. 2.39. At overpotentials larger than 175 mV, the current density is considerably larger than the one expected from the linear dependence of current on overpotential. The formation of dendritic deposits (Fig. 2.40d–f) confirms that the electrodeposition process was dominantly under activation control at the tips of dendrites. It is necessary to note that the silver deposits shown in Fig. 2.40d–f are not similar to ideal silver dendrites [26], but they behave as dendritic ones in regard to their electrochemical properties. Hence, they can be considered as degenerate dendritic deposits. Occasionally, the needle-like dendrites can also be formed.

For metals characterized by $i_0 < i_L$ (electrodeposition under mixed activation–diffusion control; $e.g.$, Cu), both η_i and η_c increase with increasing concentration of the depositing ions, indicating a decrease of the i_0/i_L ratios with the increasing concentration of metal ions [111]. The difference between η_c and η_i (see Eqs. (2.46) and (2.47)) is given by:

$$\eta_c - \eta_i = \frac{\zeta \, b_c}{2.3} \ln \frac{\delta}{h_p} \qquad (2.124)$$

It is very clear from Eq. (2.124) that this difference does not depend on the i_L/i_0 ratio and, hence, on the concentration of the depositing ions. This difference will always have a finite value which will never tend to be zero.

For metals characterized by $i_0 \gg j_L$ (electrodeposition in mixed ohmic–diffusion control of the electrodeposition; $e.g.$, Pb and Ag), increasing concentration of metal ions causes a decrease in both η_i and η_c [111]. Simultaneously, opposite to electrodeposition of metals in mixed activation–diffusion control, increasing the concentration of depositing ions leads to a strong increase in the i_0/i_L ratio.

For this group of metals (see Eqs. (2.48) and (2.49)), the difference between η_c and η_i is given by Eq. (2.125):

$$\eta_c - \eta_i = \frac{RT}{nF} \frac{i_L}{i_0} \left[\left(\frac{\delta}{h_p} \right)^{\zeta} - 1 \right] \qquad (2.125)$$

This difference decreases with the decreasing i_L/i_0 value (or increasing i_0/i_L value) and becomes negligible at the sufficiently large concentrations of depositing ions with the increasing concentration. Due to the decrease i_L/i_0 ratio with increasing concentration of depositing ions and at the sufficiently high concentration of depositing ions, this ratio will tend to be zero ($i_L/i_0 \to 0$). Then, the right side of Eq. (2.125) will also tend to be zero and hence $\eta_c - \eta_i \to 0$ (or $\eta_c \approx \eta_i$), which corresponds to full ohmic control of the electrodeposition process (see Chap. 1; Sect. 1.3.1.1). In this way, the limiting diffusion current density plateau transforms into the inflection point.

2.2.5 Spongy Deposit Formation

2.2.5.1 Low Overpotentials

Mathematical Model

In systems characterized with low exchange current density values, electrodeposition process enters the full diffusion control at sufficiently large overpotentials [13]. On the other hand, if condition $0.1 < i_0/i_L \leq 1$ is fulfilled, deposition will be under complete diffusion control at all overpotentials if some other kind of control does not take place (*e.g.*, for silver deposition on a well-defined silver crystal grains at a silver electrode at low overpotentials, two-dimensional nucleation is the rate-determining step [105]).

At low overpotentials, a small number of nuclei are formed, and they can grow independently. The limiting diffusion current density to the growing nucleus $i_{L,N}$ is given by:

$$i_{L,N} = \frac{nFDC_0}{r_N} \tag{2.126}$$

or

$$i_{L,N} = \frac{i_L \delta}{r_N} \tag{2.127}$$

where r_N is the tip radius of the nucleus. Hence, if $r_N \to 0$, condition $0.1 < i_0/i_L \leq 1$ is not satisfied and electrodeposition is under activation or mixed control. Pure activation-controlled deposition is, thus, possible even at $i_0 \gg i_L$ on very small electrodes such as nuclei on an inert substrate.

An increase in r_N leads to a decrease of $i_{L,N}$, and, at sufficiently large r_N, the electrodeposition comes under mixed activation–diffusion control, *i.e.,* when:

$$r_N > r_{mix} \tag{2.128}$$

where r_{mix} is the radius of a growing nucleus where the process comes under mixed control [7, 54].

Under mixed control of the deposition, amplification of the surface irregularities on the growing nucleus occurs, leading to the formation of a spherical agglomerate of filaments. Thereby a spongy deposit is formed. The above reasoning is valid if spherical diffusion control can occur around growing grains, as in the case of cauliflower-like deposit growth. Assuming that around each grain with radius r_N, growing under spherical diffusion control, a diffusion layer of the same thickness is formed, then the initiation of spongy growth is possible if the number of nuclei per cm^2, N, satisfies the condition:

$$N \leq \frac{1}{(4r_{\mathrm{mix}})^2} \qquad (2.129)$$

On the basis of all the above facts, it can be concluded that the formation of a spongy deposit on an inert substrate may be caused by mass-transport limitations when the nucleation rate is low. Hence, suitable conditions for the formation of spongy deposits arise at low overpotentials in systems where $i_{\mathrm{L}} < i_0$ [7, 54].

Physical Model

As was mentioned before, at a fixed value of the overpotential, the growth of a spongy deposit is possible if condition given by Eq. (2.128) is fulfilled.

The situation in which spongy deposits can start to grow can easily be demonstrated [112]. Grains of the desired size and distribution can be grown at low overpotentials under conditions of activation-controlled deposition. This corresponds to growth of grains when $r < r_{\mathrm{mix}}$. The situation in which $r > r_{\mathrm{mix}}$ can be simulated by increasing the overpotential to a sufficiently high value to result in diffusion control around the growing grains and the amplification of surface irregularities. With increasing overpotential, r_{mix} decreases. This permits the simulation of the initial stage of spongy growth, as illustrated in Fig. 2.41a, b.

Spongy growth can start on the growing nucleus if the conditions given by Eqs. (2.128) and (2.129) are both satisfied.

In the first stage of deposition, the formation of nuclei having a regular crystal shape can be expected because the deposition is activation controlled. After r_{mix} is reached, the system comes under mixed control, producing polycrystalline grains like those shown in Fig. 2.41c, just as in the case of mixed control of copper deposition (see Fig. 2.4c) [12]. In this situation, amplification of the surface irregularities on the growing grains occurs, and spongy growth is initiated.

An ideal spongy nucleus obtained in a real system is shown in Fig. 2.41c which illustrates the above discussion and physical simulation well [113]. The agglomerate of filaments in Fig. 2.42b is obviously formed by further growth of nuclei like that in Fig. 2.41d. Hence, it can be concluded that at low overpotentials the initiation of spongy growth is due to the amplification of surface protrusions directly inside the spherical diffusion layer formed around each independently growing grain, as in the case of the formation of cauliflower-like deposits. The growth of protrusions in all directions is good proof that the initial stage of deposition on the grain is under spherical diffusion control, while further growth takes place in the diffusion layer of the macroelectrode. In less ideal situations, non-ideal spongy nuclei are formed, which, however, after further deposition, results in a macroelectrode with the same appearance.

The growth of protrusions in all directions is a good proof that the deposition on the grain is under spherical diffusion control. At longer deposition times, the protrusions branch and interweave causing the macroelectrode to have a spongy appearance.
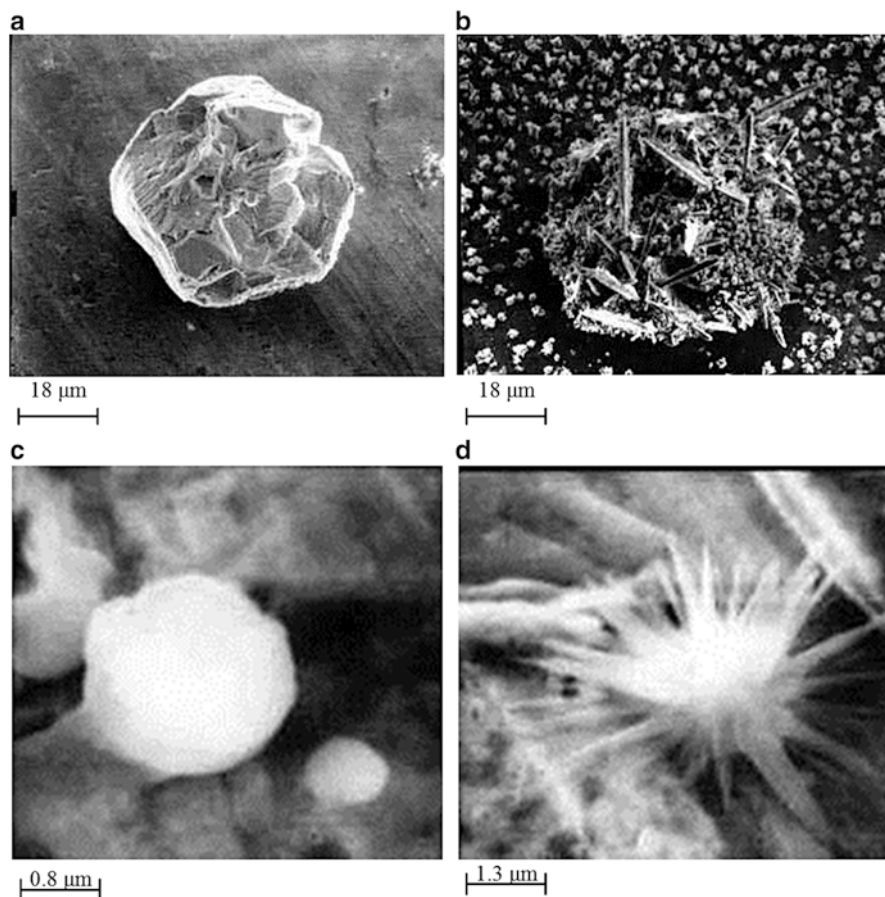
Fig. 2.41 Cadmium deposits obtained from (**a**) 1.0 M CdSO$_4$ in 0.50 M H$_2$SO$_4$ at 12 mV; Deposition time: 15 min, (**b**) 0.10 M CdSO$_4$ in 0.50 M H$_2$SO$_4$ at 120 mV. Deposition time: 45 s, and Zinc deposits obtained by deposition at 35 mV from 0.10 M zincate solution in 1.0 M KOH. Deposition time: (**c**) 7 min and (**d**) 15 min (Reprinted from Refs. [7, 13, 112] with kind permission from Springer and Ref. [113] with permission from the Serbian Chemical Society)

Real Systems

Typical spongy electrodeposits are formed during zinc and cadmium electrodeposition at low overpotentials [7, 54]. Scanning electron microscopy images of zinc deposited at an overpotential of 20 mV onto a Cu electrode from an alkaline zincate solution are shown in Fig. 2.42. The increase in the number of nuclei formed with increasing deposition time can be seen in Fig. 2.42a, b, and a spongy deposit is formed as can be seen in Fig. 2.42b. The spongy growth takes place on a relatively small number of nuclei, as is shown in Fig. 2.42b, c.
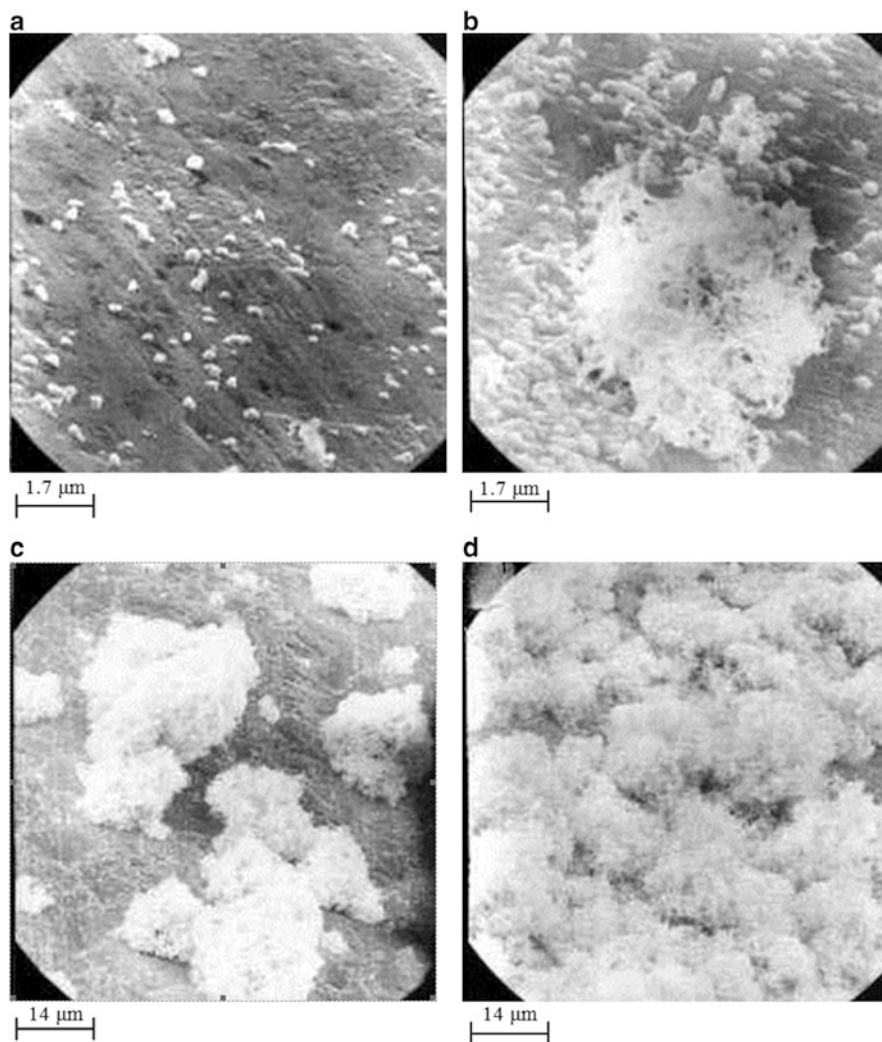
Fig. 2.42 Zinc deposits obtained by electrodeposition at 20 mV from 0.10 M zincate and 1.0 M KOH. Deposition time: (**a**) 10 min, (**b**) 20 min, (**c**) 30 min, and (**d**) 60 min (Reprinted from Refs. [7, 13, 54] with kind permission from Springer)

The initiation of spongy growth at a fixed overpotential is possible if the condition $r_N > r_{mix}$ (Eq. (2.128)) is satisfied, which is the case after some time. On the other hand, increasing the deposition time leads to the formation of a larger number of nuclei, and so the condition given by Eq. (2.129) is not satisfied over a large part of the electrode surface. Regardless of this, the coverage of the electrode surface by spongy deposits increases with increasing deposition time up to full coverage, as can be seen in Fig. 2.42d.

It should be noted that some other possible mechanisms of spongy deposit formation have been considered in a qualitative way, as reviewed in Refs. [114, 115], but the mechanism presented above seems to be the most probable [115]. However, the mechanism of formation of a spongy deposit over an initial coating, which is not seen in the case of cadmium but occurs in zinc deposition, requires clarification [54, 113]. For instance, the mechanism of spongy growth initiation in this case has not been elucidated.

2.2.5.2   Large Overpotentials

Mathematical Model

As already told, the limiting diffusion current to the growing nucleus, $i_{L,N}$, is related to i_L by Eq. (2.127).

Equation (2.4) for the growing nucleus can be rewritten in the form:

$$i_N = \frac{i_0 f_c}{1 + \frac{i_0 f_c}{i_L} \frac{r_N}{\delta}} \qquad (2.130)$$

where i_N is the current density to the growing nucleus. It is obvious from Eqs. (2.4) and (2.130) that deposition process on the macroelectrode can be under complete diffusion control if the condition given by Eq. (2.3) is fulfilled.

At the same overpotential, process on the growing nucleus can be under pure activation control if conditions

$$\frac{i_0 f_c}{i_L} \frac{r_N}{\delta} << 1 \qquad (2.131)$$

or

$$\frac{r_N}{\delta} \to 0 \qquad (2.132)$$

are satisfied [116].

Equations (2.131) and (2.132) are fulfilled in the initial stage of electrodeposition to the nuclei of metal formed on the inert substrate [112]. In this case, the nuclei behave as microelectrodes, because of their complete independent growth well before the formation of the diffusion layer of the macroelectrode. The radius r_0 of the initial stable nucleus, at overpotential η, is given by [117]:

$$r_0 = \frac{2 \gamma V}{nF} \qquad (2.133)$$

where γ is the interfacial energy between metal and solution. The radius of the growing nucleus will vary with the time according to [101]:

$$r_N = r_0 + \frac{V}{nF} i_0 f_c t \tag{2.134}$$

or

$$r_N \approx \frac{V}{nF} i_0 f_c t \tag{2.135}$$

because r_0 is extremely low.

Obviously, Eqs. (2.130), (2.131), (2.134), and (2.135) are only the approximation on growth times, because the effect of surface energy has not been taken into consideration. At larger deposition times, they are valid, because the surface energy term at higher value can be neglected [5].

An increase in r_N leads to a decrease of $i_{L,N}$, and at sufficiently large r_N deposition comes under mixed activation–diffusion control. It can be assumed that this happens at

$$i_N > v\, i_{L,N} \tag{2.136}$$

where $0 < v < 1$. By combining Eqs. (2.127), (2.130), and (2.136) one obtain:

$$r_{mix} \approx \frac{i_L v \delta}{i_0 f_c (1 - v)} \tag{2.137}$$

where r_{mix} is the radius of the growing nucleus when the process comes under mixed or spherical diffusion control. According to Barton and Bockris [5], the diffusion layer around such grain forms very fast. The further combination of Eqs. (2.135) and (2.137) gives the corresponding induction time, t_i, given by:

$$t_i = \frac{i_L}{i_0^2} \frac{v n F \delta}{V f_c^2 (1 - v)} \tag{2.138}$$

For $v = 0.2$, Eqs. (2.137) and (2.138) can be rewritten in the forms [118]

$$r_{mix} \approx \frac{i_L}{i_0} \frac{\delta}{4 f_c} \tag{2.139}$$

and

$$t_i = \frac{i_L}{i_0^2} \frac{n F \delta}{4 V f_c^2} \tag{2.140}$$

At $r_N < r_{mix}$ and $t < t_i$ the deposition on the growing grain is under activation control.

Hence, if $r_N > r_{mix}$, the spherical diffusion layer around microelectrode can be formed. This is the condition for deposition in spherical diffusion control.

The nucleus of spongy deposit, *i.e.,* hedgehog-like particle, appears when amplification of surface coarseness on the nucleus in spherical diffusion control growing starts. It was shown earlier [118] that this amplification is very fast so the induction time when growing nucleus enters mixed control can be taken also as induction time of spongy formation. It follows from Eqs. (2.139) and (2.140) that r_{mix} and t_i decrease with increasing overpotential.

On the other hand, it was also shown [54] that spongy deposit can be formed only if around each grain with radius r_{mix}, growing under spherical diffusion control, a diffusion layer of the same thickness is formed, as illustrated earlier (Eq. (2.129)).

Hence, deposition in spherical diffusion control on the growing grain is possible if both Eqs. (2.139) and (2.129) are satisfied in the same time. The nucleation law is already given by Eqs. (2.87) and (2.88).

Then, spongy deposits formation is possible if

$$N_0[1 - \exp(-At_i)] \leq \frac{1}{(4r_{mix})^2} \tag{2.141}$$

and $At_i \approx 0$ which happens at sufficiently high overpotentials where $K_2/\eta^2 \to 0$, $A \to K_1 i_0$ and $t_i \to 0$. Hence, the spongy deposit formation at high overpotentials starts at very low deposition times, when the spherical diffusion layer formed around grains does not overlap. The critical overpotential of spongy formation can be obtained by substitution of r_{mix} from Eq. (2.139) and t_i from Eq. (2.140) in Eq. (2.141) and further calculation if this overpotential is larger than critical one for instantaneous dendritic growth the dendrite spongy nuclei can be formed over inert substrate.

Real Systems

The experimental verification of the above discussion is given by the consideration of the morphology of electrodeposited silver from 0.50 M $AgNO_3$ in 0.20 M HNO_3 on the graphite electrode at different overpotentials of deposition and with different deposition times [116]. In Fig. 2.43a, the deposit obtained at an overpotential of 100 mV during 180 s is shown.

As expected, the large irregular grains are obtained. In Fig. 2.43b, c, the deposits obtained at 200 mV during 1 and 10 s are presented. At 1 s, the grains are formed, but at 10 s the needle-like deposit is obtained. This means that the spherical diffusion layer around the growing grains is not formed before the formation of the diffusion layer of the macroelectrode. The electrodeposition inside the diffusion layer of the macroelectrode is confirmed by the growth of needles toward the bulk of solution.
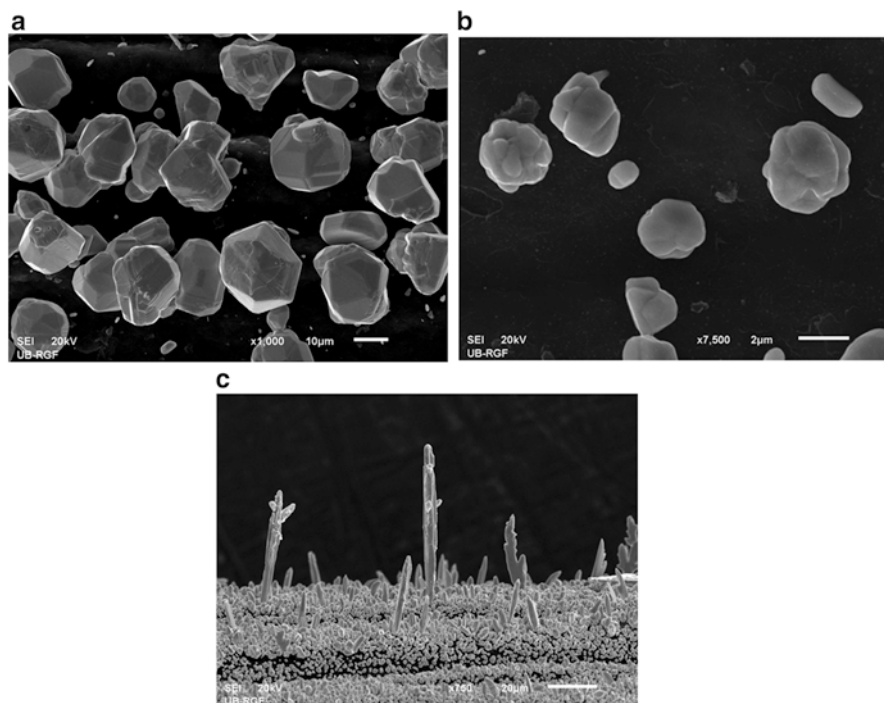
Fig. 2.43 Silver deposit obtained from 0.50 M $AgNO_3$ in 0.20 M HNO_3 at overpotentials of (**a**) 100 mV; time: 180 s, (**b**) 200 mV; time: 1 s, and (**c**) 200 mV; time: 10 s (Reprinted from Ref. [116] with permission from ESG)

At an overpotential of 300 mV, the conditions of the spherical diffusion control around the growing grains are fulfilled and dendritic-spongy deposit is formed, as can be seen from Fig. 2.44.

The growth of dendrites in all directions means that there is a spherical control to the growing grains in the initial stage of the electrodeposition.

Finally, the fact that r_{mix} and t_i (Eqs. (2.139) and (2.140)) decrease with the increasing overpotential can be verified by Figs. 2.44 and 2.45.

2.2.6   Whisker Deposits

This form of crystal growth differs from that of dendrites in that (a) it tends to have a still larger ratio between the longitudinal and the lateral dimensions with an almost perfect preservation of the latter during growth, and (b) it exhibits no tendency to side branching. Impurities or additives in the electrolyte seem to be a prerequisite for its appearance [11, 119].

Gorbunova et al. [120, 121] grew silver whiskers from fairly concentrated silver nitrate solutions (>0.30 M) containing oleic acid, gelatin, albumin, heptyl, octyl, and nonyl alcohols.
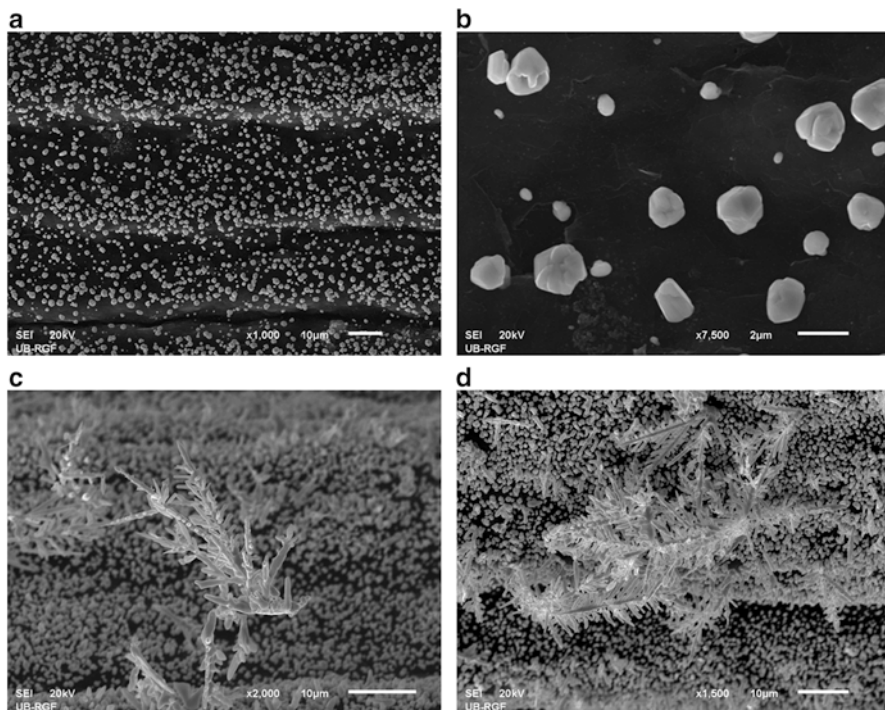
Fig. 2.44 Silver deposits obtained at an overpotential of 300 mV with a time of (**a**) 1 s, (**b**) 1 s, (**c**) 3 s, and (**d**) 5 s (Reprinted from Ref. [116] with permission from ESG)

A few more phenomena should be noted: (a) while growing exclusively in one direction only, whiskers dissolve anodically at a practically uniform rate from all sides [119] and at an overpotential much smaller than that needed for growth; (b) a higher overpotential is needed temporarily for the initiation of growth (or continuation after interruption) than for growth at a steady rate; (c) if the growth is interrupted for a longer period of time, then it may continue at the tip, but usually assuming a new direction, or else it may be completely prevented and a new whisker started elsewhere. The minimum time required for complete cessation of further growth was found to depend on the concentration of the additive; (d) if a constant rate of growth is maintained, by a constant current flow through the cell to the individual whisker tip, fluctuations of overpotential are observed.

Finally, it should be noted that whiskers differ from other crystals of the same metal in two respects at least: they have an increased electrical resistivity (two to three times that of crystals deposited in the absence of additives) and an increased tensile strength compared to large, pure silver single crystals [11].

A model of the growth mechanism was developed by Price et al. [119] which gives a good account of most of the phenomena observed. The basic assumption of the model is that molecules of impurities or additives are strongly adsorbed at all but one crystal plane and at such a concentration as to completely block the
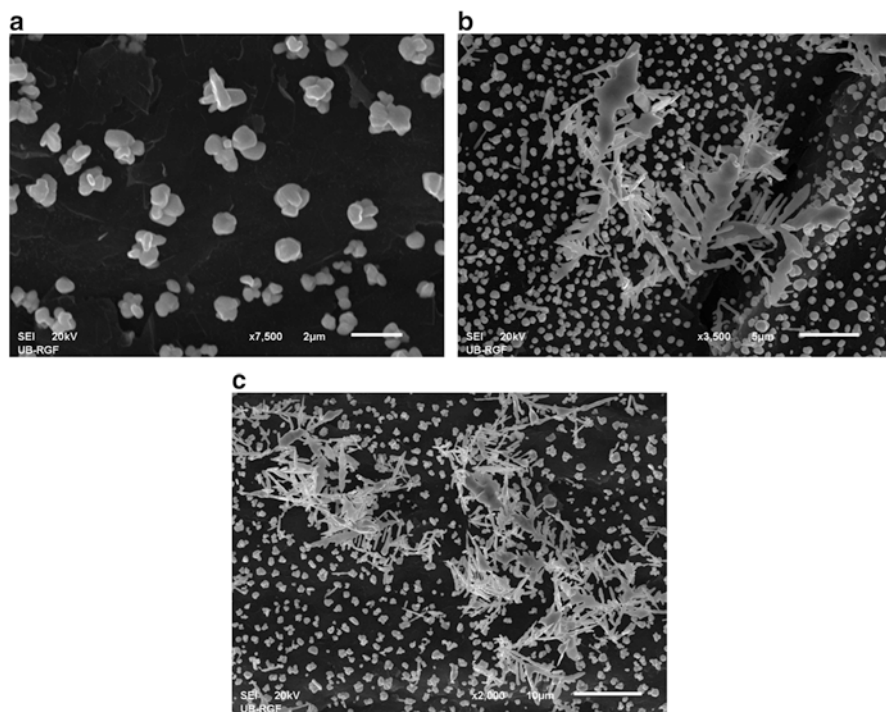
Fig. 2.45 Silver deposits obtained at an overpotential of 700 mV with a time of (**a**) 0.15 s, (**b**) 0.30 s, and (**c**) 0.50 s (Reprinted from Ref. [116] with permission from ESG)

deposition and extension of the lattice. On the one plane, however, the process of adsorption is competitive with that of metal deposition whereby the adsorbed molecules are buried, and, at a steady state, a sufficiently low surface coverage of foreign molecules is maintained for growth to be possible. The latter is assumed to occur by continuous nucleation and movement of steps over the close-packed surface. Indeed, the appearance of some whiskers suggests repeated one-dimensional nucleation of the type shown in Fig. 2.8a and the extension of the step in two directions to the edge of the crystal.

References

1. Popov KI, Živković PM, Nikolić ND (2010) The effect of morphology of activated electrodes on their electrochemical activity. In: Djokić SS (ed) Electrodeposition: theory and practice, vol 48, Series: modern aspects of electrochemistry. Springer, New York, pp 163–213
2. Bockris JO'M, Reddy AKN, Gamboa–Aldeco M (2000) Modern electrochemistry 2A, fundamentals of electrodics, 2nd edn. Kluwer Academic/Plenum Publishers, New York, p 1248

3. Diggle JW, Despić AR, Bockris JO'M (1969) The mechanism of the dendritic electrocrystallization of zinc. J Electrochem Soc 116:1503–1514
4. Živković PM, Grgur BN, Popov KI (2008) The validity of the general polarization curve equation approximation for the metal deposition process. J Serb Chem Soc 73:227–231
5. Barton JL, Bockris JO'M (1962) The electrolytic growth of dendrites from ionic solutions. Proc Roy Soc A268:485–505
6. Popov KI, Živković PM, Grgur BN (2007) Physical and mathematical models of an inert macroelectrode modified with active hemispherical microelectrodes. Electrochim Acta 52:4696–4707
7. Popov KI, Krstajić NV, Čekerevac MI (1996) The mechanism of formation of coarse and disperse electrodeposits. In: White RE, Conway BE, Bockris JO'M (eds) Modern aspects of electrochemistry, vol 30. Plenum Press, New York, pp 261–311
8. Popov KI, Nikolić ND (2012) General Theory of Disperse Metal Electrodeposits Formation. In: Djokić SS (ed) Electrochemical Production of Metal Powders. Series: Modern Aspects of Electrochemistry, vol 54. Springer, New York, pp 1–62
9. Despić AR, Diggle JW, Bockris JO'M (1968) Mechanism of formation of zinc dendrites. J Electrochem Soc 115:507–508
10. Gilleadi E (1993) Electrode kinetics. VCH Publishers Inc, New York, p 443
11. Despić AR, Popov KI (1972) Transport controlled deposition and dissolution of metals. In: Conway BE, Bockris JO'M (eds) Modern aspects of electrochemistry, vol 7. Plenum Press, New York, pp 199–313
12. Popov KI, Grgur BN, Pavlović MG, Radmilović V (1993) The morphology of copper electrodeposits: I. The mechanism of copper cauliflower-like electrodeposit formation. J Serb Chem Soc 58:1055–1062
13. Popov KI, Djokić SS, Grgur BN (2002) Fundamental aspects of electrometallurgy. Kluwer Academic/Plenum Publishers, New York
14. Popov KI (1971) Deposition and dissolution of metals in diffusion control conditions. University of Belgrade, Dissertation (in Serbian)
15. Popov KI, Pavlović LjJ, Pavlović MG, Čekerevac MI (1988) Electrode surface coarsening in potentiostatic copper electrodeposition. Surf Coat Technol 35:39–45
16. Popov KI, Pavlović MG, Pavlović LjJ, Čekerevac MI, Remović GŽ (1988) Electrode surface coarsening in pulsating overpotential copper electrodeposition. Surf Coat Technol 34:355–363
17. Popov KI, Maksimović MD, Pavlović MG, Lukić DT (1980) The mechanism of copper powder formation in potentiostatic deposition. J Appl Electrochem 10:299–308
18. Damjanović A (1965) On the mechanism of metal electrocrystallization. Plating 52:1017–1026
19. Popov KI, Radmilović V, Grgur BN, Pavlović MG (1994) The morphology of copper electrodeposits. III. The disperse deposits formation. J Serb Chem Soc 59:119–125
20. Popov KI, Radmilović V, Grgur BN, Pavlović MG (1994) The morphology of copper electrodeposits. II. The mechanism of carrot-like electrodeposit formations. J Serb Chem Soc 59:47–52
21. Pangarov NA (1964) On the crystal orientation of electrodeposited metals. Electrochim Acta 9:721–726
22. Pangarov NA, Vitkova SD (1966) Preferred orientation of electrodeposited cobalt crystallites. Electrochim Acta 11:1733–1745
23. Maksimović MD, Popov KI, Jović LjJ, Pavlović MG (1979) Mechanism of electrode surface roughening in galvanostatic metal deposition at natural convection. Bull Soc Chim 44:547–554
24. Maksimović MD, Popov KI, Pavlović MG (1979) Roughening in galvanostatic metal deposition on a rotating disc electrode. Bull Soc Chim 44:687–693

25. Popov KI, Maksimović MD (1989) Theory of the effect of electrodeposition at a periodically changing rate on the morphology of metal deposits. In: Conway BE, Bockris JO'M, White RE (eds) Modern aspects of electrochemistry, vol 19. Plenum Press, New York, pp 193–250

26. Wranglen G (1960) Dendrites and growth layers in the electrocrystallization of metals. Electrochim Acta 2:130–146

27. Bechtoldt CJ, Ogburn F, Smith J (1968) Structure and morphology of electrodeposited molybdenum dendrites. J Electrochem Soc 115:813–816

28. Faust JW, John HF (1963) Growth twins in F.C.C metals. J Electrochem Soc 110:463–464

29. Faust JW, John HF (1961) Germanium dendritic studies. I. Studies of thin structures and the seeding mechanism. J Electrochem Soc 108:855–860

30. Smith J, Ogburn F, Bechtoldt CJ (1968) Multiple twin structures in electrodeposited silver dendrites. J Electrochem Soc 115:371–374

31. Justinijanović IN, Despić AR (1973) Some observation on the properties of zinc electrodeposited from alkaline zincate solutions. Electrochim Acta 18:709–712

32. Bockris JO'M, Razumney GA (1967) Fundamental aspects of electrocrystallization. Plenum Press, New York

33. Popov KI, Čekerevac MI (1989) Dendritic electrocrystallization of cadmium from acid sulphate solution II: the effect of the geometry of dendrite precursors on the shape of dendrites. Surf Coat Technol 37:435–440

34. Nikolić ND, Popov KI, Ivanović ER, Branković G, Stevanović SI, Živković PM (2015) The potentiostatic current transients and the role of local diffusion fields in formation of the 2D lead dendrites from the concentrated electrolyte. J Electroanal Chem 739:137–148

35. Nikolić ND, Popov KI (2014) A new approach to the understanding of the mechanism of lead electrodeposition. In: Djokić SS (ed) Electrodeposition and surface finishing, vol 57, Series: modern aspects of electrochemistry. Springer, New York, pp 85–132

36. Nikolić ND, Popov KI, Ivanović ER, Branković G (2014) Effect of orientation of initially formed grains on the final morphology of electrodeposited lead. J Serb Chem Soc 79:993–1005

37. Newman JS (1973) Electrochemical systems. Prentice-Hall Inc, Engelwood Cliffs, p 177

38. Popov KI, Maksimović MD, Trnjavčev JD, Pavlović MG (1981) Dendritic electrocrystallization and the mechanism of powder formation in the potentiostatic electrodeposition of metals. J Appl Electrochem 11:239–246

39. Popov KI, Krstajić NV, Pantelić RM, Popov SR (1985) Dendritic electrocrystallisation of lead from lead nitrate solution. Surf Technol 26:177–183

40. Popov KI, Pavlović MG, Jovićević JN (1989) Morphology of tin powder particles obtained in electrodeposition on copper cathode by constant and square – wave pulsating overpotential from Sn(II) alkaline solution. Hydrometallurgy 23:127–137

41. Epstein IM (1966) Priblizhennaya formula polubeskonechnoi cilindricheskoi diffuzii. Elektrokhimiya 2:734–736 (in Russian)

42. Scharifker B, Hills G (1983) Theoretical and experimental studies of multiple nucleation. Electrochim Acta 28:879–889

43. Popov KI, Pavlović MG (1993) Electrodeposition of metal powders with controlled grain size and morphology. In: White RE, Bockris JO'M, Conway BE (eds) Modern aspects of electrochemistry, vol 24. Plenum Press, New York, pp 299–391

44. Calusaru A (1979) Electrodeposition of metal powders. Material science monography, vol 3. Elsevier, Amsterdam

45. Ibl N (1962) The formation of powdered metal deposits. In: Delahay P, Tobias CW (eds) Advances in electrochemistry and electrochemical engineering, vol 2. Intersience, New York

46. Pangarov NA (1967) Twining processes in the electrocrystallization of face-centred cubic metals. Phys Stat Sol 20:371–377

47. Gutzov I (1964) Kinetics of electrolytic phase-formation under galvanostatic conditions. Izv Inst Fiz Chim Bulgar Acad Nauk 4:69–88 (in Bulgarian)

48. Klapka V (1970) To the problem of crystallization overvoltage during electrocrystallization of metals. Coll Czechoslov Chem Comun 35:899–906
49. Pangarov NA, Velinov V (1966) The orientation of silver nuclei on a platinum substrate. Electrochim Acta 11:1753–1758
50. Pangarov NA, Vitkova SD, Uzunova I (1966) Electronographic investigation of the degree of preferred orientation of nickel electrodeposits. Electrochim Acta 11:1747–1751
51. Markov I, Boynov A, Toshev S (1973) Screening action and growth kinetics of electrodeposited mercury droplets. Electrochim Acta 18:377–384
52. Štrbac S, Rakočević Z, Popov KI, Pavlović MG, Petrović R (1999) The role of surface defects in HOPG on the electrochemical and physical deposition of Ag. J Serb Chem Soc 64:483–493
53. Milchev A, Kruijt WS, Sluyters-Rehbach M, Sluyters JH (1993) Distribution of the nucleation rate in the vicinity of a groving spherical cluster. Part 1. Theory and simulation results. J Electroanal Chem 362:21–31; Kruijt WS, Sluyters-Rehbach M, Sluyters JH, Milchev A (1994) Distribution of the nucleation rate in the vicinity of a growing spherical cluster. Part 2. Theory of some special cases and experimaental results. J Electroanal Chem 371:13–26
54. Popov KI, Krstajić NV (1983) The mechanism of spongy electrodeposits formation on inert substrate at low overpotentials. J Appl Electrochem 13:775–782
55. Markov I (1976) Saturation nucleus density in the electrodeposition of metal onto inert electrodes. I. Theory. Thin Solid Films 35:11–20; Markov I, Stoycheva E (1976) Saturation nucleus density in the electrodeposition of metal onto inert electrodes. II. Experimental. Thin Solid Films 35:21–35
56. Kaishew R, Mutafctschiew B (1965) Electrolytic nucleation of mercury. Electrochim Acta 10:643–650 (in German)
57. Erdey-Grúz T, Volmer Z (1931) Overvoltage of metals. Z Phys Chem 157A:165–181 (in German)
58. Fetter K (1967) Electrochemical kinetics. Khimiya, Moscow (in Russian)
59. Fleischmann M, Thirsk HR (1959) The potentiostatic study of the growth of deposits on electrodes. Electrochim Acta 1:146–160
60. Kovarskii NY, Lisov AV (1984) Periodicities in the surface structure of polycrystalline electrolytic deposits. Elektrokhimiya 20:221–225 (in Russian)
61. Kovarskii NY, Lisov AV (1984) The reasons for the structure periodicity in the surfaces of electrolyte copper deposits. Elektrokhimiya 20:833–837 (in Russian)
62. Kovarskii NY, Arzhanova TA (1986) On the nature of the "no nucleation" zones in the electrocrystallization process. Elektrokhimiya 20:452–458 (in Russian)
63. Popov KI, Grgur BN, Stojilković ER, Pavlović MG, Nikolić ND (1997) The effect of deposition process exchange current density on the thin metal films formation on inert substrate. J Serb Chem Soc 62:433–442
64. Popov KI, Krstajić NV, Popov SR (1983) Fundamental aspects of plating technology. II: morphological aspects of metal electrodeposition from complex salt solutions. Surf Technol 20:203–208
65. Dimitrov AT, Hadži-Jordanov S, Popov KI, Pavlović MG, Radmilović V (1998) Electrodeposition of silver from nitrate solutions: part I. Effect of phosphate ions on morphology. J Appl Electrochem 28:791–796
66. Popov KI, Pavlović MG, Grgur BN, Dimitrov AT, Hadži-Jordanov S (1998) Electrodeposition of silver from nitrate solutions: part II. Mechanism of the effect of phospate ions. J Appl Electrochem 28:797–801
67. Radmilović V, Popov KI, Pavlović MG, Dimitrov AT, Hadži-Jordanov S (1998) The mechanism of silver granular electrodeposits formation. J Solid State Electrochem 2:162–169
68. Popov KI, Rodaljević ZP, Krstajić NV, Novaković SD (1985) Fundamental aspects of plating technology V: the effect of strongly adsorbed species on the morphology of metal deposit. Surf Technol 25:217–222

69. Meibuhr S, Yeger E, Kozawa A, Hovorka F (1963) The electrochemistry of tin I. Effect of nonionic addition agents on electrodeposition from stannous sulfate solutions. J Electrochem Soc 110:190–202

70. Kabanov BN (1966) Electrochemistry of metal and adsorption. Nauka, Moscow (in Russian)

71. Lorenz W (1954) Oscillographic overvoltage measurements. Z Electrochem 58:912–918 (in German)

72. Despić AR (1983) Deposition and dissolution of metals and alloys. In: Bockris JO'M, Conway BE, Yeger E, White RE (eds) Comprehensive treatise of electrochemistry, 2nd edn. Plenum Press, New York

73. Oniciu L, Muresan LM (1991) Some fundamental aspects of levelling and brightening in metal electrodeposition. J Appl Electrochem 21:565–574

74. Muresan LM, Varvara SC (2005) Levelling and brightening mechanisms in metal electrode-position. In: Nunez M (ed) Metal electrodeposition. Nova Science Publishers Inc, ew York, pp 1–45

75. Kardos O, Foulke G (1962) Applications of mass transfer theory. In: Delahay P, Tobias CW (eds) Electrodeposition on small-scale profiles. Advances in electrochemistry and electro-chemical engineering, 2nd edn. Interscience, New York

76. Ibl N (1983) Current distribution. In: Yeger E, Bockris JO'M, Conway BE, Sarangapani S (eds) Comprehensive treatise of electrochemistry, 6th edn. Plenum Press, New York

77. Kruglikov SS, Kudriavtsev NT, Vorobiova GF, Antonov AY (1965) On the mechanism of levelling by addition agents in electrodeposition of metals. Electrochim Acta 10:253–262

78. Dukovic JO, Tobias CW (1990) Simulation of levelling in electrodeposition. J Electrochem Soc 137:3748–3755

79. Đorđević S, Maksimović MD, Pavlović MG, Popov KI (1997) Electroplating. Tehnička knjiga, Beograd (in Serbian)

80. Krichmar SI (1965) On the theory of the levelling action in the electrochemical behaviour of metals. Elektrokhimiya 1:858–861 (in Russian); Krichmar SI (1965) Levelling mechanism in the cathodic deposition of nickel. Zh Fiz Khim 39:602–603 (in Russian)

81. Krichmar SI, Pronskaya AY (1965) Experimental investigation of the levelling effect in the cathodic deposition of nickel from coumarine containing electrolytes. Zh Fiz Khim 39:741–744 (in Russian)

82. Jordan KG, Tobias CW (1991) The effect of inhibitor transport on levelling in electrodepo-sition. J Electrochem Soc 138:1251–1259

83. Dukovic JO (1993) Feature-scale simulation of resist-pattered electrodposition. IBM J Res Develop 37:125–141

84. Andricacos PC, Uzoh C, Dukovic JO, Horkans J, Deligianni H (1998) Damascene copper electroplating for chip interconnection. IBM J Res Develop 42:567–574

85. Schlesinger M, Paunovic M (eds) (2000) Modern electroplating. Wiley-interscience publi-cation, New York

86. Weil R, Paquin R (1960) The relationship between brightness and structure in electroplated nickel. J Elec-trochem Soc 107:87–91

87. Nikolić ND, Rakočević Z, Popov KI (2005) Nanostructural analysis of bright metal surfaces in relation to their reflectivities. In: Conway BE, Vayenas CG, White RE, Gamboa-Adelco M (eds) Modern aspects of electrochemistry, vol 38. Kluwer Academic/Plenum Publishers, New York, pp 425–474

88. Dennis JK, Such TE (1993) Nickel and chromium plating. Wood head publ. ltd, Cambridge

89. Nichols RJ, Bach CE, Meyer H (1993) The effect of three organic additives on the structure and growth of electrodeposited copper: an in-sity scaning probe microscopy study. Ber Bunsenges Phys Chem 97:1012–1020

90. Czerwinski F, Kondo K, Szpunar JA (1997) Atomic force microscopy study of surface morphology of zinc-iron electrodeposits. J Electrochem Soc 144:481–484

91. Nikolić ND, Rakočević Z, Popov KI (2001) Structural characteristics of bright copper surfaces. J Electroanal Chem 514:56–66

92. Nikolić ND, Rakočević Z, Popov KI (2001) The STM analysis of a silver mirror surface. J Serb Chem Soc 66:723–727
93. Edwards J (1953) The mechanism of electropolishing of copper in phosphoric acid solutions. I. Processes preceding the establishment of polishing conditions. J Electrochem Soc 100:189c–194c
94. Wagner C (1954) Contribution to the theory of electropolishing. J Electrochem Soc 101:225–228
95. Krichmar SI, Pronskaya AY (1966) Study of the levelling effect in electrochemical polishing of metals. Elektrokhimiya 2:69–73 (in Russian)
96. Popov KI, Pavlović MG, Rakočević Z, Škorić DM (1995) The structure of bright copper surfaces. J Serb Chem Soc 60:873–878
97. Nikolić ND, Rakočević Z, Popov KI (2004) Reflection and structural analyses of mirror bright metal coatings. J Solid State Electrochem 8:526–531
98. Nikolić ND, Popov KI, Rakočević Z, Đurović DR, Pavlović MG, Stojanović M (2000) The structure of bright zinc coatings. J Serb Chem Soc 65:819–827
99. Nikolić ND, Rakočević Z, Đurović DR, Popov KI (2006) Nanostructural analysis of mirror – bright zinc coatings. Russ J Electrochem 42:1121–1126
100. Nikolić ND, Novaković G, Rakočević Z, Đurović DR, Popov KI (2002) Comparative reflection and structural analyses of copper and zinc coatings electrodeposited from acid sulfate solutions without and with additives. Surf Coat Technol 161:188–194
101. Bockris JO'M, Nagy Z, Dražić DM (1973) On the morphology of zinc electrodeposited from alkaline solutions. J Electrochem Soc 120:30–41
102. Jovićević JN, Despić AR, Dražić DM (1977) Studies of the deposition of cadmium on foreign substrates. Electrochim Acta 22:577–587
103. Despić AR, Dražić MD, Mirjanić MD (1978) Granular growth of electrochemically deposited metals. Faraday Discuss Chem Soc 12:126–135
104. Popov KI, Čekerevac MI, Nikolić LjN (1988) The dendritic electrocrystallization of cadmium from acid sulphate solutions I: Granular cadmium substrate. Surf Coat Technol 34:219–229
105. Popov KI, Krstajić NV, Jerotijević ZD, Marinković SR (1985) Electrocrystallization of silver from silver nitrate solutions at low overpotentials. Surf Technol 26:185–188
106. Jović VD, Nikolić ND, Lačnjevac UČ, Jović BM, Popov KI (2012) Morphology of different electrodeposited pure metal powders. In: Djokić SS (ed) Electrochemical production of metal powders, vol 54, Series: modern aspects of electrochemistry. Springer, New York, pp 63–123
107. Price PB, Vermilyea DA (1958) Kinetics of electrodeposition of silver. J Chem Phys 28:720–721
108. Popov KI, Živković PM, Krstić SB, Nikolić ND (2009) Polarization curves in the Ohmic controlled electrodeposition of metals. Electrochim Acta 54:2924–2931
109. Meibhur S, Yeager E, Kozawa A, Hovorka F (1963) The electrochemistry of tin: I. Effects of nonionic addition agents on electrodeposition from stannous sulfate solutions. J Electrochem Soc 110:190–202
110. Popov KI, Pavlović MG, Stojilković ER, Stevanović ZŽ (1997) The current density distribution on stationary wire electrodes during copper and lead electro-deposition. Hydrometallurgy 46:321–336
111. Nikolić ND, Popov KI, Živković PM, Branković G (2013) A new insight into the mechanism of lead electrodeposition: Ohmic–diffusion control of the electrodeposition process. J Electroanal Chem 691:66–76
112. Popov KI, Krstajić NV, Popov SR, Čekerevac MI (1986) Spongy electrodeposit formation. J Appl Electrochem 16:771–774
113. Popov KI, Krstajić NV, Simičić MV, Bibić NM (1992) The initial stage of spongy electrodeposit formation on inert substrate. J Serb Chem Soc 57:927–933
114. Jakšić MM (1985) Impurity effects on the macromorphology of electrodeposited zinc I: theoretical consideration and a review of existing knowledge. Surf Technol 24:193–217

115. Murashova I, Pomosov B (1989) Electrodeposition of metals in dendritic shapes. In: Polukarov YM (ed) In Itogi nauki i tehniki, Seria Elektrokhimiya, vol 30. Acad Sci, Moscow (in Russian)
116. Popov KI, Živković PM, Nikolić ND (2012) Formation of disperse silver deposits by the electrodeposition processes at high overpotentials. Int J Electrochem Sci 7:686–696
117. Toshev S, Markov I (1967) Electrolytic nucleation of cadmium. Electrochim Acta 12:281–286
118. Popov KI, Krstajić NV, Popov SR (1985) The morphology of cadmium deposits obtained on foreign substrates at high overpotentials. J Appl Electrochem 15:151–154
119. Price PB, Vermilyea DA, Webb MB (1958) The growth and properties of electrolytic whiskers. Acta Mat 6:524–531
120. Gorbunova KM, Zhukova AJ (1949) Crystallochemical and diffusion mechanism of electrocrystallization. Zh Fiz Khim 23:605–615 (in Russian)
121. Gorbunova KM, Pankov PD (1949) Regularities in the crystallization of thin silver filaments. Zh Fiz Khim 23:616–624 (in Russian)